Author:
Green, Kirk

Title:
Bifurcation analysis of a semiconductor laser subject to phase conjugate feedback

Bifurcation analysis of a semiconductor laser subject to phase-conjugate feedback

Kirk Green

Department of Engineering Mathematics
University of Bristol

A dissertation submitted to the University of Bristol
in accordance with the requirements of the degree of
Doctor of Philosophy in the Faculty of Engineering

September 2002

Abstract

In this thesis we present a detailed bifurcation analysis of a semiconductor laser subject to phase-conjugate feedback (PCF). Mathematically, lasers with feedback are modelled by delay differential equations (DDEs) with an infinite-dimensional phase space. This is why, in the past, systems described by DDEs were only studied by numerical simulation. We employ new numerical bifurcation tools for DDEs that go much beyond mere simulation. More precisely, we continue steady states and periodic orbits, irrespective of their stability with the package DDE-BIFTOOL, and present here the first algorithm for computing unstable manifolds of saddle-periodic orbits with one unstable Floquet multiplier in systems of DDEs. Together, these tools make it possible, for the first time, to numerically study global bifurcations in DDEs.

Specifically, we first show how periodic solutions of the PCF laser are all connected to one another via a locked steady state solution. A one-parameter study of these steady states reveals heteroclinic bifurcations, which turn out to be responsible for bistability and excitability at the locking boundaries. We then perform a full two-parameter investigation of the locking range, where we continue bifurcations of steady states and heteroclinic bifurcations. This leads to the identification of a number of codimension-two bifurcation points. Here, we also make a first attempt at providing a two-parameter study of bifurcations of periodic orbits in a system of DDEs. Finally, our new method for the computation of unstable manifolds of saddle periodic orbits is used to show how a torus breaks up with a sudden transition to chaos in a crisis bifurcation.

In more general terms, we believe that the results presented in this thesis showcase the usefulness of continuation and manifold computations and will contribute to the theory of global bifurcations in DDEs.

Acknowledgements

Firstly, many thanks to my supervisor Bernd Krauskopf for his continued support and enthusiasm throughout this project. Without Bernd's commitment and attention to detail this work would not have been possible.

Thankyou to all my colleagues in the Engineering Mathematics department. In particular, those I started my studies with: Gareth, Ines and Piotr; Bart for his excellent knowledge of Linux; Rob the ploymaster; and everyone else for making the past three years a thoroughly enjoyable experience.

In the laser and nonlinear dynamics communities, I would like to thank Ingo Fischer, Tilmann Heil, Sebastian Wieczorek, Raj Roy, Thomas Erneux, Koen Engelborghs, Giovanni Samaey and everyone I have met at conferences around the world.

Finally, I would like to thank my friends and family, with special thanks to Clare for her support during my studies.

Author's declaration

I declare that the work in this dissertation was carried out in accordance with the Regulations of the University of Bristol. The work is original except where indicated by special reference in the text and no part of the dissertation has been submitted for any other degree.

Any views expressed in the dissertation are those of the author and in no way represent those of the University of Bristol.

The dissertation has not been presented to any other University for examination either in the United Kingdom or overseas.

Signed:.....

Date:....16/12/02

Contents

List of Figures

Chapter 1

Summary and overview

Recently there has been much interest in the nonlinear dynamics of semiconductor lasers; see, for example, the recent overviews Refs. [37, 59, 60] and further references therein. Due to the material properties of semiconductor lasers, external influences can alter the stability and dynamics of the laser dramatically. Knowledge of this effect is therefore essential for physical applications. Of particular interest are lasers subject to optical feedback, such as lasers with conventional optical feedback (COF) from an external mirror [17, 44, 46, 49], lasers with opto-electronic feedback [67], mutually coupled lasers with delay [33] and lasers with phase conjugate feedback (PCF) [1, 6, 19, 22, 23, 35, 61], the case considered here. In all these cases the relevant and generally well-established models are delay differential equations (DDEs) [7, 9, 31]. Delay generally arises by optical reflection on an external reflector such as a CD or an optical fibre, so that the laser 'sees' its past output after a fixed time delay. Feedback can easily destabilise the laser and lead to regimes of chaotic output. In many applications this is unwanted, and expensive optical isolators need to be used. However, recently there has been considerable interest in the controlled production of chaotic optical output for use in chaotic communication schemes [16, 66]. In general, an understanding of the dynamics of a semiconductor laser with feedback can lead to new uses and better control of lasers. Considering the vast amount of lasers used in applications, this is of a considerable economic interest.

On the mathematical side, there has been a lot of interest recently in delay differential equations, at least partly motivated by the many applications including biology [50], chemistry [15], neural networks [47] and control theory [21]. It is quite a challenge to understand the dynamics and bifurcations of a DDE. Already in the case of one fixed delay τ (like in a laser with feedback), the phase space of the DDE is the infinite-

dimensional space of continuous functions on the delay interval $[-\tau.0]$; see Ref. [62] and Chapter 3. Tackling delay equations arising in applications is analytically very hard, and for a long time the only numerical tool was simulation by direct integration of the DDE.

The good news is that this is now changing dramatically with the arrival of continuation software, notably the package DDE-BIFTOOL [12, 13, 14], which allows the user to find and follow equilibria and periodic orbits irrespective of their stability. Changes of the stability (local codimension-one bifurcations) can be detected and also followed as parameters are varied. DDE-BIFTOOL essentially implements the local bifurcation theory of DDEs [7]. (This has roughly the same functionality that the local bifurcation theory part of the well-known continuation package AUTO [8] has for ordinary differential equations (ODEs).) DDE-BIFTOOL is still under development with new capabilities being added; one is the continuation of homoclinic and heteroclinic orbits to equilibria; see Ref. [55] and Chapter 8.

There are already some examples of the usefulness of these new techniques. In the series of papers [30, 52, 53] connecting bridges of periodic solutions were studied between steady states in the COF laser using DDE-BIFTOOL. Similar work on the rate equations describing a vertical-cavity surface-emitting laser (VCSEL) can be found in [56]. Continuation studies of the PCF laser can be found in [26, 27, 28].

As is known from the respective theory for ODEs, the next step is to understand the global dynamics of a DDE. To this end one needs to find not only saddle points and saddle periodic orbits, but also their global stable and unstable manifolds. Except in the case of a one-dimensional unstable manifold of an equilibrium [27] (see Section 3.1), they cannot be found by mere simulation, but require more sophisticated methods. We have made a step in this direction by providing the first algorithm for computing global unstable manifolds of saddle periodic orbits with one unstable Floquet multiplier in systems of DDEs. This allows us, for the first time in DDEs, to compute certain invariant objects, for example, an underlying torus on which a locked solution lies. Furthermore, we can detect certain global bifurcations, an example is the crisis bifurcation discussed in Chapter 9; see also [28].

This thesis is an in-depth study of complicated dynamics and routes to chaos in a PCF laser using the new tools of continuation and manifold computations. The numerical bifurcation analysis presented in this thesis is one of the first examples of its kind for DDEs.

We began our study by analysing the effect a variation of the feedback strength has

on the dynamics of the PCF laser. Mathematically, this requires a one-parameter study of the governing rate equations. Previous studies by direct integration of the DDE modelling the PCF laser found that as the feedback strength was increased the overall picture was that of regions of periodic output interspersed with 'bubbles' of more complicated dynamics, which for the most part were chaotic [35]. Our first step is to analyse the periodic solutions found between these chaotic regions using the recently developed continuation package DDE-BIFTOOL; see Section 3.4.2. This reveals that a number of them end in Hopf bifurcations associated with the same unstable steady state, therefore, a connection between the periodic solutions of the PCF laser is found. This part of our study also leads to the discovery of homoclinic orbits associated with the periodic solutions.

Our next step is to study in detail the steady state solution to which the periodic solutions are connected. This steady state is shown to be stable for low feedback strengths. By using continuation techniques alongside the computation of unstable manifolds of equilibria we reveal global bifurcations and bistability at both boundaries of this region of stability. These global bifurcations are a saddle-focus heteroclinic bifurcation, where we computed the associated heteroclinic orbit using a new functionality of DDE-BIFTOOL [55], and a heteroclinic bifurcation between a saddle steady state and a saddle periodic orbit, which we identified by computing unstable manifolds of saddle equilibria.

The next logical step in the analysis of the PCF laser is to construct a full two-dimensional bifurcation diagram. While two-parameter continuation of bifurcations of periodic orbits in DDEs is currently unavailable, we perform a full two-parameter study of the bifurcations of the steady state and a two-parameter continuation of the saddle-focus heteroclinic orbit. This revealed a key organising centre for the dynamics of the PCF laser, namely, a codimension-two bifurcation of the heteroclinic orbit, which is identified as a T-point bifurcation.

We then study a transition from one of the periodic solutions to the 'second bubble' of chaos in the PCF laser. By using a new tool we developed for the computation of unstable manifolds of saddle-periodic orbits in systems of DDEs, we are able to show that a crisis bifurcation is responsible for this sudden transition to chaos. This part of our study also leads to the discovery of regions of bistability associated with this transition.

Outline of the thesis

In Chapter 2 we introduce the general theory of semiconductor lasers and optical feedback.

Chapter 3 provides a detailed introduction into the general theory and computational methods for DDEs. We first explain equilibria, periodic solutions, the Poincaré map and unstable manifolds in terms of the structure of a DDE. Secondly, we explain numerical integration of a DDE and then new tools, namely, numerical continuation using DDE-BIFTOOL and computing unstable manifolds of saddle periodic solutions.

A semiconductor laser subject to phase-conjugate feedback (PCF) is introduced in Chapter 4. The PCF laser, a technologically relevant example of a DDE, will be the object of study throughout the rest of this thesis.

In Chapter 5 we present an algorithm for computing unstable manifolds of saddle-type periodic orbits with one unstable Floquet multiplier in systems of DDEs.

Chapter 6 provides a detailed bifurcation analysis of the frequency locked, external-cavity modes (ECMs) of the PCF laser. We continue steady states and periodic orbits irrespective of their stability. In this way, we show that the periodic orbits corresponding to the ECMs are connected to the steady state solution of the PCF laser. We also identify symmetric and non-symmetric homoclinic orbits and hysteresis in the system.

In Chapter 7 we investigate, in detail, the steady state solution, which we refer to as the locking range of the PCF laser. Again, we find and follow steady states regardless of their stability and compute unstable manifolds of saddle equilibria. Furthermore, we identify heteroclinic bifurcations, which turn out to be responsible for bistability and excitability at the locking boundaries.

The locked, steady state solution of the PCF laser is investigated in further detail in Chapter 8. We perform a two-parameter bifurcation analysis and show how codimension-two bifurcations globally organise the dynamics of the PCF laser near the locking range.

In Chapter 9 we use the new method of computing unstable manifolds of saddle periodic orbits in DDEs (introduced in Chapter 5) to investigate a transition to chaos in the PCF laser. We show how a torus breaks up with a final sudden onset of chaos in a crisis bifurcation. We also identify regions of bistability between periodic solutions and other attractors in the system.

Finally, in Chapter 10 we draw conclusions and discuss future work.

Chapter 2

Semiconductor lasers

The majority of lasers in application today are semiconductor lasers. They can be found, for example, in CD-players, laser printers and in optical communications networks. Semiconductor lasers are so-called Class B lasers, in which the polarization of the electric field can be adiabatically eliminated. As a consequence, they can be described well by three-dimensional rate equations, one for the complex electric field $E(t)$ and one for the population inversion $N(t)$ (the number of excited states that can produce a single photon). It turns out that the phase $\phi(t)$ of the electric field follows the two equations for the optical intensity $P(t)$ and the inversion $N(t)$. Therefore, a solitary semiconductor laser is essentially a two-dimensional dynamical system that cannot exhibit chaotic dynamics. The only observable dynamical behavior is a damped periodic exchange between the electric field and the inversion. These oscillations are referred to as *relaxation oscillations* in the laser literature (not to be confused with relaxation oscillations in slow-fast systems); see, for example, [37, 59] as an entry point to the theory of semiconductor lasers.

To obtain chaotic dynamics requires the addition of one or more degrees of freedom to the system describing a semiconductor laser. The good news, from a dynamical systems point of view, is that this is easily achievable with the addition of some form of external forcing. This forcing may be due to noise, optical injection from another laser, or delayed optical feedback; see Section 2.2.

2.1 Semiconductor laser rate equations

The standard rate equations for a single-mode semiconductor laser are given by

$$\frac{dE}{dt} = \frac{1}{2}(1-i\alpha)G_N(N(t)-N_{\text{th}})E(t) \tag{2.1}$$

$$\frac{dN}{dt} = \frac{J}{qd} - \frac{N(t)}{T_1} - \left[T_{\text{ph}}^{-1} + G_N(N(t)-N_{\text{th}})\right]P(t), \tag{2.2}$$

for the evolution of the slowly varying complex electric field $E(t)$ and the population inversion $N(t)$ [59]. In equations (2.1) and (2.2), $P(t)$ denotes the photon density within the laser cavity which is directly proportional to the optical intensity $|E(t)|^2$. Other parameters include the differential-gain G_N, and the threshold carrier density N_{th}. The pumping terms in equation (2.2) involve the current density J which is injected into an active layer of depth d, and the magnitude of the electron charge q. The carrier lifetime T_1 is typically $\sim$ 1 ns and the photon lifetime $T_{\text{ph}} \sim$ 1 ps.

The linewidth enhancement factor α is an important material property of a semiconductor laser. It governs a strong nonlinear coupling between the amplitude of the light and phase variations of the light inside the laser cavity. It is defined as a ratio between the imaginary and real parts of the differential gain coefficients, Ω_N and G_N, respectively,

$$\alpha = 2\frac{\partial\Omega/\partial N}{\partial G/\partial N}. \tag{2.3}$$

Any change in the optical gain G results in a change in the optical frequency Ω. For semiconductor lasers, α typically take values between 2 and 6; we note that for gas or solid-state lasers, α is approximately zero. Physically, α enhances the line-width of the laser by a factor of $1+\alpha^2$, which is a strong effect in semiconductor lasers.

2.2 Optical feedback

Optical feedback results when part of the solitary laser's output intensity is fed back into the laser after a time τ. This feedback can be unwanted, for example, reflections from a CD or optical fibre. However, controllable feedback can be obtained by adding an external mirror to the laser set-up; see already Fig. 4.1.

This addition of a conventional optical reflector to the laser set-up results in conven-

tional optical feedback (COF) [17, 49]. Mathematically, this feedback is described by adding a delay term to equation (2.1) [44], resulting in the following delay differential equation (DDE) for the evolution of the electric field,

$$\dot{E}(t) = \left.\frac{dE}{dt}\right|_{\text{Solitary Laser}} + \kappa E(t-\tau)\exp[-i\omega_0\tau]. \tag{2.4}$$

In equation (2.4), the relevant feedback parameters are the feedback strength κ, the round-trip time in the external cavity τ, and the feedback phase $e^{-i\omega_0\tau}$; where ω_0 is the optical frequency of the solitary laser.

Equation (2.4) assumes weak feedback so that multiple round-trips in the external-cavity can be neglected. It also assumes no significant change in the electric field during one internal round-trip so that complex modal dynamics can be neglected, in other words, the laser is single-mode. Even with these simplifications, the theoretical results obtained using equations (2.2) and (2.4) have been shown to compare very well with experimental results.

Mathematically, the delay implies that the phase space of the system is now infinite-dimensional; see Chapter 3. The dynamics of the laser are no longer restricted to relaxation oscillations, for example, the dynamics of the laser with feedback can undergo period-doubling, and exhibit quasiperiodic motion and chaos.

A local stability analysis of equations (2.2) and (2.4) reveals that the number of solutions increases as the feedback strength is increased [62]. These are running phase solutions, or external-cavity modes (ECMs) or continuous wave (CW) states of the COF laser, and are of the form $(R_s e^{i\omega_s t}, N_s)$ where R_s, ω_s and N_s are constant and can be determined from equations (2.2) and (2.4). They are created in pairs in saddle-node bifurcations, each pair consists of a mode and an antimode. All antimodes are always saddle points and the majority of modes are quickly destabilised in Hopf bifurcations as the feedback strength κ or the feedback phase $e^{-i\omega_0\tau}$ is varied. Note here that equations (2.2) and (2.4) have S^1-symmetry. When this symmetry is taken into account an ECM can be reduced to a fixed point by using a rotating frame of reference.

With such a large number of saddle points in the system, the COF laser can produce a wealth of dynamical behaviour. The most studied dynamics in the COF laser are known as low frequency fluctuations (LFF) and recently the related regular pulse packages (RPPs). Regular pulse packages occur in the short cavity regime, where the number of modes is not too large [32]. They are characterised by a regular quasiperiodic global orbit in phase space. As the feedback strength and, hence, the number of modes

increases the dynamical regime changes to that of LFF. These are characterised by an irregular global orbit in phase space, with large power drop-outs. For higher pump-currents the LFF regime becomes more chaotic, this is known as Coherence Collapse [45].

In Chapter 4 we introduce the semiconductor laser with phase-conjugate feedback (PCF). We will see that the equations describing the PCF laser have $\mathbb{Z}_2$-symmetry. Due to this discrete symmetry the PCF laser does not exhibit the same dynamical behaviour as the COF laser. As we shall see, the discrete symmetry of the PCF laser means that there may be symmetry-breaking bifurcations, which play a crucial role in the dynamical behaviour of the PCF laser.

As we have seen, delay differential equations (DDEs) are vital in modelling lasers with feedback. Before we investigate the dynamics and bifurcations of the PCF laser, we first provide a brief introduction into the theory of DDEs and computational methods used in investigating them.

Chapter 3

General theory of DDEs

We now recall some basic facts on DDEs; see Refs. [7, 31, 62] as general references to the theory. Readers may find it useful to look ahead to the concrete example of a laser with phase-conjugate feedback, system (4.1) in Chapter 4, which is used for the illustration throughout. We consider the simplest case, namely an autonomous DDE with a single fixed delay. It has the general form

$$\frac{dx(t)}{dt} = F(x(t), x(t-\tau), \lambda), \tag{3.1}$$

where

$$F : \mathbb{R}^n \times \mathbb{R}^n \times \mathbb{R}^p \to \mathbb{R}^n$$

is differentiable and where $\tau \in \mathbb{R}$ is a fixed delay, while $\lambda \in \mathbb{R}^p$ represents a number of physical parameters. Considering a single fixed delay is less of a restriction than it seems: for example, all of the laser systems mentioned in Chapters 1 and 2 are in this class. Furthermore, the algorithm described in Chapter 5 also works for delay equations with a finite number of fixed delays, by way of working with the largest such delay. Other types of delay, such as state dependent delays, are beyond the scope of this thesis.

As it is the case for finite-dimensional vector fields, the function F assigns at a given moment t in time a vector, but this vector now not only depends on the state $x(t)$ but also on $x(t-\tau)$ at time τ earlier. The solution of (3.1) is a function

$$x : [-\tau, \infty) \to \mathbb{R}^n, \tag{3.2}$$

which is a one-parameter family of vectors $x(t)$ defined only for all positive values of

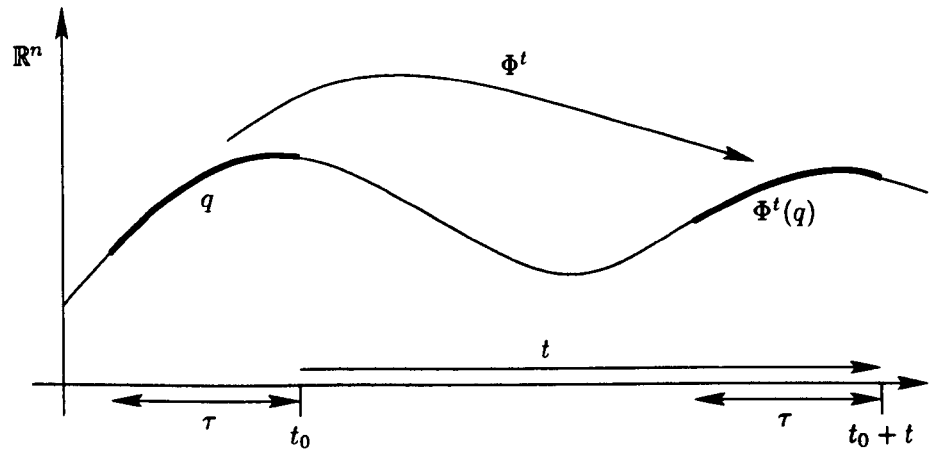

Figure 3.1: The evolution operator Φ^t of a DDE takes a point q to $\Phi^t(q)$ for any positive $t > 0$. In projection onto the physical space $\mathbb{R}^n$, the point q is a finite piece of curve that is transported under Φ^t much like a train moving over a roller coaster track.

time t. We call $\mathbb{R}^n$ the physical space of the system, but the crucial thing is that $\mathbb{R}^n$ is *not* the phase space of (3.1). Indeed, one needs to know the entire *history* of $x(0)$, that is, a continuous function on the interval $[-\tau, 0]$ for (3.1) to have a unique solution. In other words, the phase space of (3.1) is the infinite-dimensional space of continuous functions with values in the physical space $\mathbb{R}^n$, denoted by $\mathscr{C}$. When we speak of a *point*, say $q \in \mathscr{C}$, in what follows we mean a point in this infinite-dimensional phase space, that is, q is a continuous function

$$q : [-\tau, 0] \to \mathbb{R}^n .$$

Further, we call $q(0)$ the head of q and $\{q(t) \mid t \in [-\tau, 0)\}$ its history.

The *evolution operator*

$$\Phi^t : \mathscr{C} \to \mathscr{C} \tag{3.3}$$

describes how an initial condition $q \in \mathscr{C}$ evolves after time t. It is formally given by an abstract differential equation on the infinite-dimensional phase space [11]. More geometrically, one can picture Φ^t as illustrated in Fig. 3.1. The point q is mapped under Φ^t to a new point $\Phi^t(q)$. If one imagines letting time t run then $\Phi^t(q)$ moves over the solution x of (3.1) like a train over a roller coaster track.

In general, the flow is not defined for negative time. However, for special solutions,

such as periodic orbits and their stable and unstable manifolds, the flow can be defined also for negative time; see e.g. Ref. [31].

3.1 Equilibria

The simplest invariant object of (3.1) is an equilibrium point $x(t) = x_0$ for all $t \in [0,\infty]$ and fixed $x_0 \in \mathbb{R}^n$, which satisfies $F(x_0,x_0,\lambda^*) = 0$ (where the parameter is now fixed to λ^*). Its stability is determined by the eigenvalues of the linearisation $DF(x_0,x_0,\lambda^*) = Ax(t) + Bx(t-\tau)$ around x_0, where $A = D_1F(x_0,x_0,\lambda^*)$ and $B = D_2F(x_0,x_0,\lambda^*)$ are the derivatives of F in (3.1) with respect to the first and second variable. The spectrum of the operator DF consists only of eigenvalues and is given by the roots of the characteristic function $\chi(\lambda) = \det(\lambda I - A - Be^{-\lambda\tau})$.

It is an important property of DDEs with fixed delays that the eigenvalues are discrete and that there are at most finitely many eigenvalues with real part larger than γ, for any fixed $\gamma \in \mathbb{R}$ [7, Theorem 4.4 (i)]. In particular, there are only finitely many unstable eigendirections (associated with eigenvalues with real part greater than zero). Furthermore, $\chi(\lambda)$ has at most finitely many roots in a given vertical strip, that is, the eigenvalues are isolated and cannot have a finite accumulation point [7, Theorem 4.4 (ii)]; for eigenvalues in the left half-plane, the following holds $|Im(\lambda)| \leq Ce^{-\tau Re(\lambda)}$, where C is a constant [7, Theorem 4.4 (iii)]; and if there are no eigenvalues in the right half-plane $\{\lambda \mid Re(\lambda) \geq 0\}$, all solutions of (3.1) converge to zero exponentially as time t tends to infinity [7, Corollary 5.5].

One says that an equilibrium x_0 is hyperbolic, if $DF(x_0,x_0,\lambda^*)$ has no eigenvalues with zero real part. A hyperbolic equilibrium x_0 is either stable, namely if all of these eigenvalues have real part less than zero, or a saddle otherwise. In the latter case one can consider its *local unstable manifold* $W^u_{loc}(x_0)$, which is the set of points q that can be integrated backwards, never leave a small neighbourhood V of x_0 under Φ^t for $t < 0$ and are such that $\Phi^t(q) \to x_0$ as $t \to -\infty$. The local unstable manifold $W^u_{loc}(x_0)$ is finite-dimensional and tangent to the linear eigenspace $E^u(x_0)$ spanned by the unstable eigenfunctions. The (global) unstable manifold $W^u(x_0)$ is defined as $W^u(x_0) = \{\Phi^t(p) \mid p \in W^u_{loc}(x_0) \text{ and } t > 0\}$. The stable manifold $W^s(x_0)$ is defined similarly as the set of points that converge to x_0 under Φ^t in positive time. Note that $W^s(x_0)$ is always infinite-dimensional [7, Chapter VIII].

When there is one unstable eigenvalue then the unstable manifold $W^u(x_0)$ is a smooth 1D curve in projection onto the physical space $\mathbb{R}^n$. Both of its branches can be found

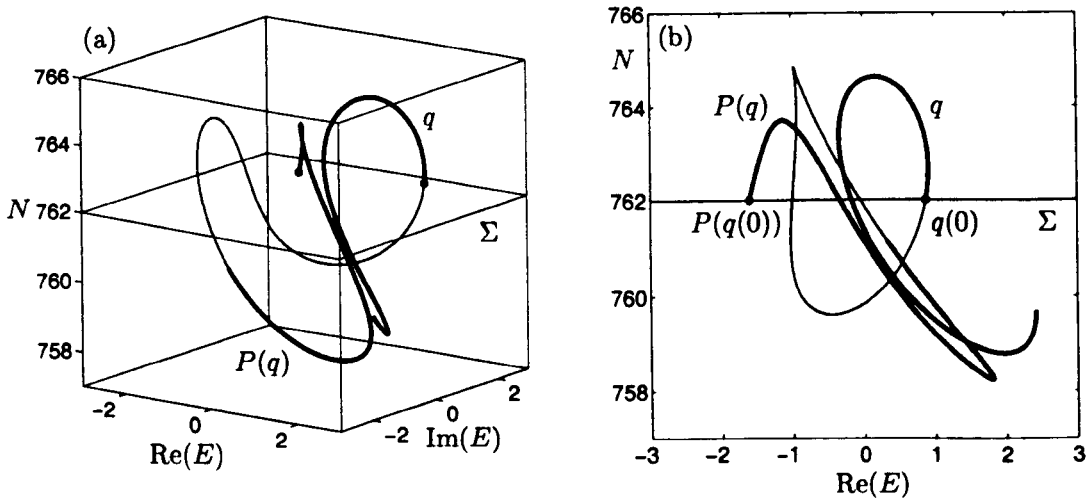

Figure 3.2: The Poincaré map P takes a point q with $q(0) \in \Sigma$ to the point $P(q)$ with $P(q(0)) \in \Sigma$, which is shown in (E,N)-space (a) and in the $(\mathrm{Re}(E),N)$-plane (b) for the PCF laser (4.1).

by integrating two initial conditions near x_0 along the linear eigenspace $E^u(x_0)$. Approximations to both x_0 and $E^u(x_0)$ can be found with the continuation software DDE-BIFTOOL; see Section 3.4.2. Examples of 1D unstable manifolds of equilibria can be found in Chapter 7.

It is much harder to compute higher-dimensional unstable manifolds of equilibria. It appears to be possible that methods from ODEs [40] can be generalised to the DDE case, but this is work for the future. The main interest here is in computing 1D unstable manifolds of a saddle point of the Poincaré map associated with a given periodic orbit.

3.2 Periodic orbits and the Poincaré map of a DDE

A *periodic point* of (3.1) is a solution $q \in \mathscr{C}$ such that $\Phi^{\mathsf{T}}(q) = q$ for some (smallest) period $\mathsf{T} > 0$. The associated solution $\Gamma(t)$ starting from q is a *periodic orbit*. In other words, a periodic orbit is a solution along which any segment of length τ repeats after time T. The periodic orbit Γ traces out a closed curve in projection onto the physical space $\mathbb{R}^n$.

A very useful concept is that of the Poincaré map P defined by the return to a suitable section transverse to the flow of (3.1). For a prescribed section $\Sigma \subset \mathbb{R}^n$ we denote by $\mathscr{C}_\Sigma$

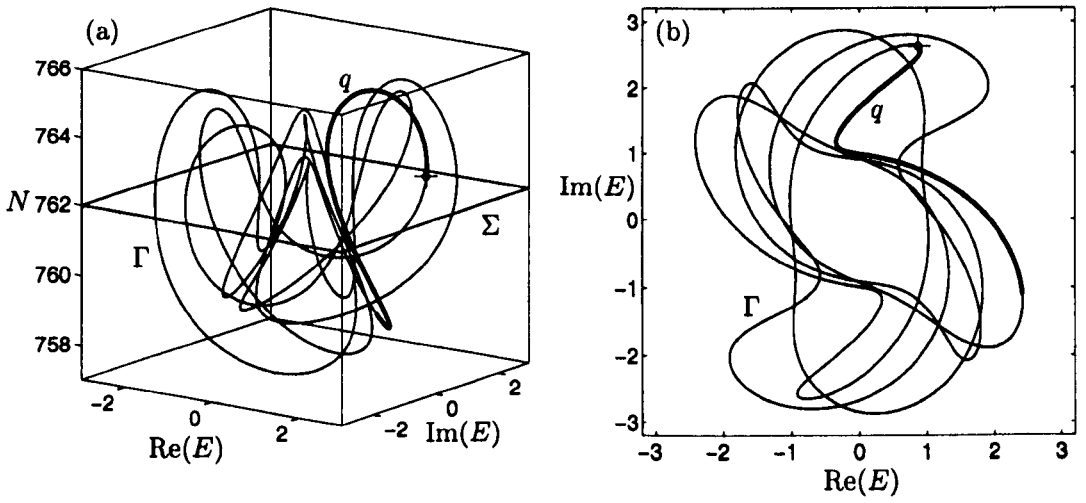

Figure 3.3: A periodic orbit Γ of the DDE and a periodic point q of the Poincaré map P (boldface), shown in (E,N)-space (a) and in the E-plane (b) for the PCF laser (4.1).

the space of points in $\mathscr{C}$ with headpoints in Σ. Then the Poincaré map P is defined as

$$P\colon \mathscr{C}_\Sigma \to \mathscr{C}_\Sigma, \quad q \mapsto \Phi^{t_q}(q), \tag{3.4}$$

where $t_q > 0$ is the return time to Σ. In other words, the headpoint of $P(q)$ again lies in the section Σ, as is illustrated in Fig. 3.2.

One can always find a section Σ (locally) transverse to a periodic orbit Γ, so that the Poincaré map is well-defined at least locally near the intersection point with Σ, which is a fixed point $q \in \mathscr{C}_\Sigma$ under P (and a periodic point of (3.1) as defined above); see Fig. 3.3.

The stability of a periodic orbit Γ is given by its Floquet multipliers, which are the eigenvalues of the linearisation $DP(q)$ of the Poincaré map P at the associated fixed point $q \in \mathscr{C}_\Sigma$. The linearisation $DP(q)$ is a compact operator, which implies that its spectrum consists of countably many eigenvalues (the Floquet multipliers) with the origin of the complex plane as their only possible accumulation point; see e.g. Refs. [31, 62] for more details. It follows that for any fixed $r > 0$ there are only a finite number of Floquet multipliers outside a circle of radius r. In particular, there are always only a finite number of unstable Floquet multipliers, that is Floquet multipliers outside the unit circle. A periodic orbit is called hyperbolic if there are no Floquet multipliers on the unit circle. A hyperbolic periodic orbit is either stable if all the Floquet multipliers are inside the unit circle or of saddle type with finitely many unstable Floquet multipliers.

If there are other Floquet multipliers on the unit circle then the system is undergo-

ing a bifurcation. In this study we will encounter saddle-node, symmetry-breaking and torus (or Neimark-Sacker) bifurcations, which are all associated with Floquet multipliers crossing the unit circle.

We now briefly discuss how one can compute the Poincaré map P in practice. Near q the map P can be defined as the kth return to the section Σ for some fixed k, where k counts all intersections of the periodic orbit with Σ (of which $k-1$ are outside a small neighbourhood of q). It is generally not possible to define P *globally* as the kth return map to Σ for a fixed k. Indeed there typically are curves in Σ along which the flow fails to be transverse and this changes the number of returns to Σ. (This is in contrast to periodically forced systems, which do have a globally defined Poincaré map in the form of the stroboscopic map of the forcing frequency.) Such a tangency can occur at the begin point, an interior point or the end point of the orbit of the flow. In our computations we deal with the case that a tangency occurs at an interior point: we detect it and change the definition of P from being the kth to the $(k+2)$th (or the $(k-2)$th) return to Σ. This is done by monitoring the return time to Σ, which is a continuous function across such a tangency. Indeed discontinuities of the kth return map are encountered when computing a global object such as an unstable manifold, and dealing with them as just explained allows us to compute longer pieces of manifolds; see Section 5.1.5 for an example.

3.3 Unstable manifold of a fixed point

Suppose that a periodic orbit has Floquet multipliers outside the unit circle. For a suitable section Σ transverse to the periodic orbit we consider the fixed point $q \in \mathscr{C}_\Sigma$ (with headpoint in Σ) of the associated Poincaré map P. The *local unstable manifold* $W^u_{\mathrm{loc}}(q)$ of q is the set of all points $p \in \mathscr{C}_\Sigma$ that can be iterated backwards under P, never leave a small neighbourhood V of q and are such that $P^l(p) \to q$ as $l \to -\infty$. The local unstable manifold $W^u_{\mathrm{loc}}(q)$ is finite-dimensional and tangent to the linear eigenspace $E^u(q)$ spanned by the unstable eigenfunction. In the case that there is a single Floquet multiplier outside the unit circle then, in projection onto the physical space $\mathbb{R}^n$, the 1D linear eigenspace $E^u(q)$ forms a one-parameter family of directions along (the history of) q, as is illustrated in Fig. 3.4. The (global) unstable manifold $W^u(q)$ can be defined as $\{P^l(p) \mid p \in W^u_{\mathrm{loc}}(q) \text{ and } l > 0\}$.

The stable manifold $W^s(q)$ is defined similarly as the set of points that converge to q under P in positive time. Again, $W^s(q)$ is always infinite-dimensional.

In projection onto the physical space $\mathbb{R}^n$ a 1D unstable manifold $W^u(q)$ forms a

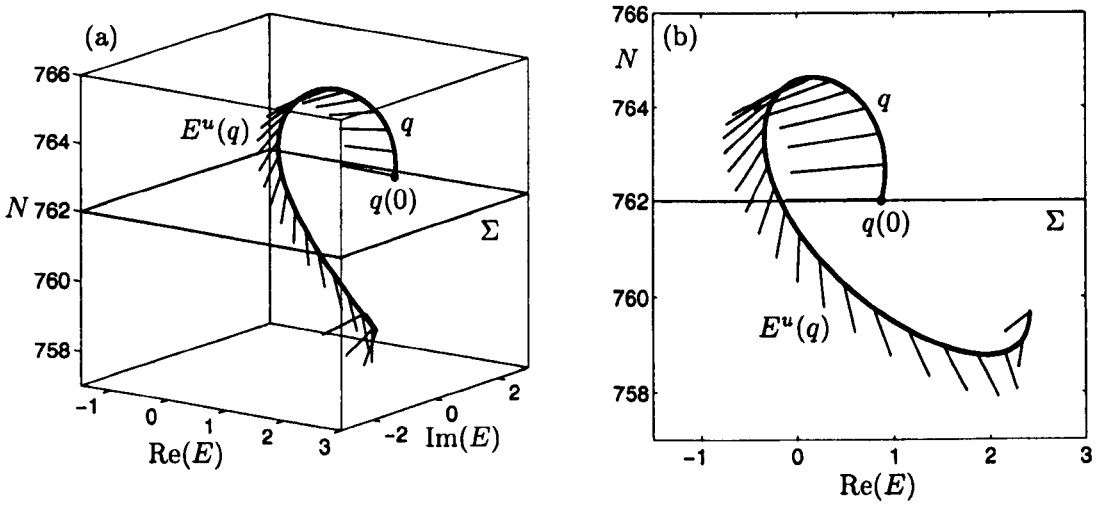

Figure 3.4: A periodic point of saddle-type q together with the linear line field approximating the unstable linear eigenspace $E^u(q)$ (only every 100th line of the discrete representation is shown), shown in (E,N)-space (a) and in the $(\mathrm{Re}(E),N)$-plane (b) for the PCF laser (4.1).

complicated object; see already Fig. 5.5 below. However, its *trace* $W^u(q) \cap \Sigma$ is a 1D curve that is smooth (except possibly at isolated points due to the projection). The trace of the 1D unstable manifold $W^u(q)$ reveals about as much as a 1D unstable manifold of a diffeomorphism in $\mathbb{R}^2$; see Section 5.1.5. We remark that the trace may have self-intersections. This is an artifact of the projection and reminds one of the fact that $W^u(q)$ lives in an infinite-dimensional phase space.

3.4 Computational methods for DDEs

3.4.1 Numerical integration

A DDE of the form (3.1) with a fixed delay can easily be integrated numerically with a fixed time-step method, where the time step is such that it fits an integer number of times into the delay time τ. To this end, one discretises the history of every point, that is, the interval $[-\tau,0]$, into M subintervals. Here the integer M is chosen such that the integration step τ/M is sufficiently small. This induces a discretisation of time t into steps of τ/M, yielding a numerical approximation of the evolution operator $\Phi^{\tau/M}$ as the basic integration step.

It is particularly useful to represent a point q by a circular list as is shown in Fig. 3.5 (a), where **root** points to the headpoint $q(0)$ of q. In the simplest case of an Euler

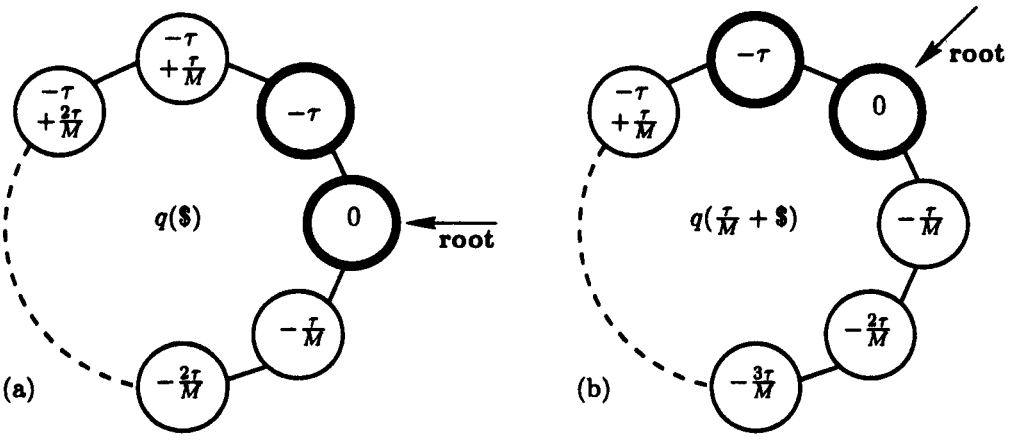

Figure 3.5: One Euler integration step applied to the circular list representing a point of a DDE. The delay interval is discretised into $M+1$ elements, with \$ standing for the labels of the list elements. Before the integration step **root** points to $q(0)$ (a), and after the integration step **root** points to $q(\frac{\tau}{M})$, which can be achieved by simply overwriting $q(-\tau)$ and moving **root** (b). Only the two boldfaced list elements close to **root** are needed for one Euler step.

integration step, the point $q(-\tau)$ is simply overwritten by the new headpoint $q(\tau/M)$ of $\Phi^{\tau/M}(q)$ and **root** moves one node along the circular list. In our simulations we use an Adams-Bashforth fourth-order multistep method, which requires storing a list up to and including the vector $q(-\tau-3\frac{\tau}{M})$.

3.4.2 Numerical continuation

The recently developed continuation package DDE-BIFTOOL [12, 13, 14] goes far beyond simulation. DDE-BIFTOOL consists of Matlab routines for the continuation and bifurcation analysis of steady states and periodic solutions. Roughly speaking it has the same functionality for DDEs as (the local bifurcation part of) the well-known package AUTO [8] does for ODEs. It not only allows one to find and follow stable solutions (those also found by simulation), but unstable ones as well. Furthermore, DDE-BIFTOOL detects local bifurcations. For equilibria, these bifurcations are: a saddle-node bifurcation when a real eigenvalue changes sign, and a Hopf bifurcation when a complex pair of eigenvalues cross the imaginary axis. For periodic solutions, these bifurcations are: a saddle-node bifurcation of limit cycles when a real Floquet multiplier crosses the unit circle at $+1$, a period-doubling bifurcation when a real Floquet multiplier crosses the unit circle at -1 and a torus (Neimark-Sacker) bifurcation when a pair

of complex Floquet multipliers cross the unit circle. It is possible to compute bifurcating branches of periodic orbits from detected bifurcation points.

Because of the $\mathbb{Z}_2$-symmetry of the PCF laser, see already Chapter 4, it is possible that a Floquet multiplier crossing $+1$ corresponds to a symmetry-breaking bifurcation. In order to deal with symmetry-breaking bifurcations, DDE-BIFTOOL was extended to allow branch switching at symmetry-breaking bifurcations as well [28]. There is now a routine to compute the linearised direction corresponding to this multiplier. Specifically, it is found by computing the eigenvalues of the discretised monodromy operator. The eigenfunction which is thus found is defined on the delay interval $[-\tau, 0]$ and is further integrated under the linearised equations to obtain a profile on the complete period interval $[0, T]$. The eigenfunction can then be used as a perturbation in the direction of the emanating branch to provide a guess of an initial solution on the branch. It is also used in a special steplength condition to prevent convergence of the computation back to the original branch. During these computations, the continuation parameter is also corrected. As such, the branch switching automatically detects the direction of the emanating branch (to higher or lower values of the continuation parameter). After a first point is found, the branch can then be continued further.

Specifically, DDE-BIFTOOL solves a large system that is obtained by discretising the delay interval $[-\tau, 0]$ as described in Section 3.4.1. It uses arclength continuation to follow equilibria and periodic orbits as a parameter is varied. Periodic orbits are represented by a suitable boundary value problem, which is solved using Gauss collocation. By also solving for the eigenvalues, the above local bifurcations, for equilibria, are detected and can then be followed in two parameters; for further details see Refs. [12, 13, 14].

The usefulness of DDE-BIFTOOL can hardly be exaggerated. It enables continuation studies of local bifurcations in DDEs in much the same way as one is used to perform for ODEs. DDE-BIFTOOL has not been used that widely yet, but there are already some examples of its use in applications, for example, the study of a laser with COF in Refs. [4, 30, 52, 53] and our own work on the PCF laser in Refs. [26, 27, 28].

In the context of computing 1D unstable manifolds of periodic orbits, DDE-BIFTOOL is crucial for finding periodic orbits with one unstable Floquet multiplier as starting data.

3.4.3 1D unstable manifolds

Our second main tool is a new technique for computing 1D unstable manifolds of saddle periodic orbits. Specifically we compute the 1D unstable manifold $W^u(q)$ of an associated fixed point q of a suitable Poincaré map defined on a fixed section Σ. This allows us, for the first time in DDEs, to compute certain invariant objects, for example, an underlying torus on which the dynamics is attracted to a stable periodic orbit. Unstable manifolds are of great importance in understanding the global dynamics of a system. However, they cannot be found analytically and therefore, need to be computed by numerical methods. Our method generalises a well established algorithm for computing 1D unstable manifolds in ODEs [39]. It grows the unstable manifold such that the headpoints in Σ are a distance Δ_k apart. The distance Δ_k is constantly adapted according to the curvature of $W^u(q) \cap \Sigma$, thus providing a best possible numerical approximation given prespecified accuracy parameters. Since each intersection point of the unstable manifold in Σ has an associated history of length τ, the projection of the unstable manifold into the physical (E,N)-space forms a very complicated object. However, the trace $(W^u(q) \cap \Sigma)$ of the 1D unstable manifold in Σ is a smooth 1D curve (with the exception of some points, where smoothness may be lost due to the projection).

This method is explained in detail in Chapter 5. First, we introduce the central DDE in this thesis, describing a PCF laser.

Chapter 4

Phase-conjugate feedback

Our object of study is a semiconductor laser with phase-conjugate feedback (PCF), schematically shown in Fig. 4.1. This form of feedback is interesting as it produces a reflected wave that is wave-front inverted, with the angle of incidence of the wave being equal to the angle of reflection. Furthermore, any distortions in the external cavity are undone over a round-trip, thus the amplified beam is less spread and the energy more focused than with conventional optical feedback (COF) [19]. Also, compared to COF, where there is extreme sensitivity to the positioning of the mirror, PCF lasers are 'self-aligning'; this is an advantage when stable output is desired. Physical applications of PCF include mode locking [22] and phase locking, where PCF has been shown to reduce the laser noise considerably [1, 23, 61]. Experimental attempts at realising PCF include the studies of Refs. [5, 18, 58], where PCF was used to obtain frequency control, optical noise reduction and mode switching, respectively.

The PCF laser is a technologically relevant example of a DDE. Its physical space is three-dimensional, that is, $n = 3$ in (3.1), and this has the advantage of allowing for good illustrating figures in $\mathbb{R}^3$. Apart from its stable periodic operation, the PCF laser was shown to exhibit complicated nonlinear dynamics, including quasiperiodic motion and chaos. This was found in detailed simulations of bifurcation diagrams, phase plots and optical spectra [23, 35]. As the feedback strength is increased, the overall picture is that of regions of periodic output that are interspersed with 'bubbles' of chaos; see already Fig. 4.2.

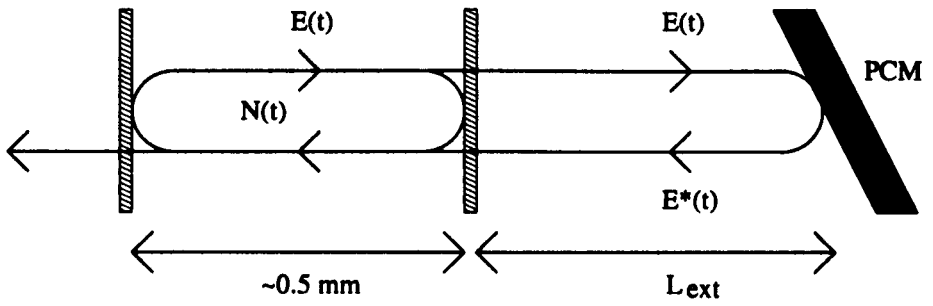

Figure 4.1: Sketch of a semiconductor laser with phase-conjugate feedback.

4.1 Rate equations

A single-mode semiconductor laser subject to weak (instantaneous) PCF can be described by the three-dimensional delay differential system

$$\begin{aligned}\frac{dE}{dt} &= \frac{1}{2}\left[-i\alpha G_N(N(t)-N_{\text{sol}})+\left(G(t)-\frac{1}{\tau_p}\right)\right]E(t)\\ &\qquad +\kappa E^*(t-\tau)\exp[2i\delta(t-\tau/2)+i\phi_{\text{PCM}}]\\ \frac{dN}{dt} &= \frac{I}{q}-\frac{N(t)}{\tau_e}-G(t)\,|E(t)|^2\end{aligned} \tag{4.1}$$

for the evolution of the slowly varying complex electric field $E(t) = E_x(t) + iE_y(t) \in \mathbb{C}$ and the population inversion $N(t) \in \mathbb{R}$ [23, 35]. In system (4.1), nonlinear gain is included as $G(t) = G_N(N(t) - N_0)(1 - \varepsilon P(t))$, where $\varepsilon = 3.57 \times 10^{-8}$ is the nonlinear gain coefficient and $P(t) = |E(t)|^2$ is the intensity. This produces an effective detuning of 166 MHz. Parameter values are set to realistic values corresponding to a Ga-Al-As semiconductor laser [23, 35], namely, the line-width enhancement factor $\alpha = 3$, the optical gain $G_N = 1190\,\text{s}^{-1}$, the photon lifetime $\tau_p = 1.4\,\text{ps}$, the pump current $I = 65.1\,\text{mA}$, the magnitude of the electron charge $q = 1.6 \times 10^{-19}\,\text{C}$, the electron lifetime $\tau_e = 2\,\text{ns}$, and the transparency electron number $N_0 = 1.64 \times 10^8$. Further, $N_{\text{sol}} = N_0 + 1/(G_N\tau_p)$. The constant phase shift ϕ_{PCM} at the PCM and the detuning parameter δ were both set to zero, as is common in the field [23, 35]. Therefore, the feedback term in system (4.1) reduces to $\kappa E^*(t-\tau)$ and involves the complex conjugated electric field E^*, the feedback

rate κ and the external cavity round-trip time τ. They are given by

$$\kappa = \frac{(1-R_m)}{\tau_L}\left[\frac{R_{\text{ext}}}{R_m}\right]^{1/2} \quad \text{and} \quad \tau = \frac{2L_{\text{ext}}}{c},$$

where $R_m = 0.12$ is the laser front-facet reflectivity, $\tau_L = 9.3\,\text{ps}$ is the round-trip time in the solitary laser cavity, R_{ext} is the power reflectivity of the PCM, and L_{ext} is the length of the external-cavity. For one-parameter studies of (4.1), we fix τ at the realistic value $\tau = 2/3\,\text{ns}$, corresponding to $L_{\text{ext}} \approx 10\,\text{cm}$, and consider the dimensionless bifurcation parameter $\kappa\tau$; for the two-parameter study in Chapter 8 we also free the parameter I.

System (4.1) has $\mathbb{Z}_2$-symmetry under the transformation $(E,N) \to (-E,N)$, where the symmetry group is $\mathbb{Z}_2 = \{1,-1\}$. This corresponds to a rotation over π of the complex E-plane, so that any attractor (or other invariant set) is either symmetric, or has a symmetric counterpart. This symmetry allows the possibility of symmetry-breaking and symmetry-restoring bifurcations [35, 42], and also implies restrictions on the types of bifurcations of periodic orbits. For example, when a Floquet multiplier of a symmetric orbit goes through $+1$ then this may indicate a symmetry-breaking bifurcation other than a saddle-node bifurcation of limit cycles. Also, symmetric orbits cannot undergo period-doubling bifurcations [43]. The numerical consequences of this symmetry were described in Section 3.4.2. Note that the PCF laser considered here is different from the COF laser in terms of the underlying symmetry of the governing equations [42]. The COF laser is symmetric under any rotation of the electric field E and does not feature symmetry-breaking bifurcations.

Figure 4.2 shows a bifurcation diagram obtained by simulation. It gives a first impression of the dynamics and bifurcations of the PCF laser as the feedback parameter $\kappa\tau$ is increased. For each value of $\kappa\tau$ we numerically integrated system (4.1), using an initial condition from the attractor corresponding to the previous value of $\kappa\tau$ (thus, for non-symmetric solutions assuring that we did not switch between symmetric counterparts). We then plotted the normalised value of the inversion $\hat{N} = (N/N_{\text{sol}} - 1) \times 10^3$ whenever the intensity P crossed its average value in the increasing direction [28, 35]. The region with no points corresponds to a steady state. A small number of points correspond to a periodic orbit. While a large number of points correspond to quasiperiodic or chaotic dynamics.

In Fig. 4.2 stable periodic orbits can clearly be seen interspersed with the bubbles of chaotic dynamics. These stable periodic orbits are external-cavity modes (ECMs) of

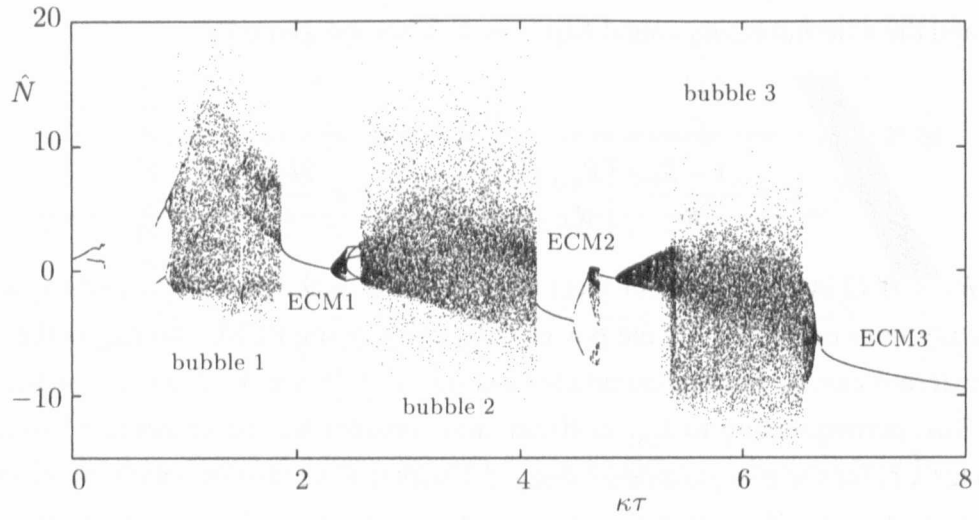

Figure 4.2: Bifurcation diagram obtained by simulation showing normalised inversion $\hat{N}$ versus the feedback strength $\kappa\tau$. The stable periodic orbits corresponding to ECM1, ECM2 and ECM3 are interspersed with three bubbles of chaotic dynamics.

the PCF laser; which we detail in Chapter 6. Within these bubbles of chaos the laser is between ECMs. The complex dynamics can be thought of as the result of a competition between ECMs. It was shown in Ref. [6] that as L_{ext} (and with it τ) is increased, the widths of the chaotic regions increase. (There, the authors also considered a finite-interaction-depth PCM leading to a model featuring a distributed delay which is beyond the scope of this study.)

We observe an absence of points for $\kappa\tau \in [0.2794, 0.7487]$ corresponding to an attracting steady state. Physically, this corresponds to a frequency match between the PCM pump laser and the solitary laser. Here, both the laser frequency and phase are locked. The laser phase no longer undergoes diffusion and, subsequently, the line-width of the laser is extremely narrow [1, 61]. This narrow line-width was shown to remain stable even with the addition of noise from spontaneous emission [23]. This is why the PCF laser is interesting for applications requiring narrow laser line-width, such as, spectroscopy. We will see in Chapter 6 that this locked state provides a connection between the ECMs.

As is traditional in the field, when studying the PCF laser we will work with the physical rate equations of system (4.1). In the future, this will allow for direct comparison to experimental results which presently are unavailable for the PCF laser. In order to understand in more detail the nature of different transitions to chaos in the PCF laser we

will use new numerical techniques, namely the combination of DDE-BIFTOOL with the manifold computations introduced in this thesis. For completeness, we present a brief analysis of the stability of the steady states of the PCF laser in the next section, where in order to make the algebra more simple we write system (4.1) in a dimensionless form.

4.2 Local stability analysis of the PCF laser

Here we perform a local stability analysis of system (4.1). To compute steady states and the characteristic function around a steady state, see Section 3.1, we first write system (4.1) in a dimensionless form.

4.2.1 Dimensionless PCF rate equations

In full, system (4.1) can be written as

$$\begin{aligned} \frac{dE}{dt'} &= \frac{1}{2}\begin{bmatrix} (G_N(N(t')-N_0)-\tau_p^{-1})(1-i\alpha) \\ -\varepsilon|E(t')|^2 G_N(N(t')-N_0) \end{bmatrix} E(t') + \kappa E^*(t'-\tau), \\ \frac{dN}{dt'} &= \frac{I}{q} - \frac{N(t')}{\tau_e} - G_N(N(t')-N_0)(1-\varepsilon|E(t')|^2)|E(t')|^2 \end{aligned} \tag{4.2}$$

Next, we introduce the dimensionless variables t, $Y(t)$ and $Z(t)$ defined by

$$t \equiv t'/\tau_p, Y(t) \equiv \sqrt{\frac{\tau_e G_N}{2}} E(t') \text{ and } \mathrm{Z(t)} \equiv \frac{\mathrm{G_N}\tau_\mathrm{p}}{2}(\mathrm{N(t')} - \mathrm{N_{sol}}).$$

By substitution into Eqs. (4.2), we find the dimensionless equations

$$\begin{aligned} \frac{dY}{dt} &= \left[Z(t)(1-i\alpha) - \frac{\varepsilon'}{2}|Y(t)|^2(1+2Z(t))\right]Y(t), \\ &\quad +\gamma Y^*(t-\theta), \\ T\frac{dZ}{dt} &= P - Z(t) - (1+2Z(t))(1-\varepsilon'|Y(t)|^2)|Y(t)|^2. \end{aligned} \tag{4.3}$$

where

$$\begin{aligned} \varepsilon' &= \frac{2\varepsilon}{\tau_e G_N}, \gamma = \kappa\tau_\mathrm{p}, \theta = \tau/\tau_\mathrm{p}, \mathrm{T} = \tau_\mathrm{e}\tau_\mathrm{p}^{-1} \\ I_{th} &= \frac{N_{sol} q}{\tau_e}, \mathrm{P} = \frac{\mathrm{G_N}\tau_\mathrm{p}\tau_\mathrm{e}}{2}\left(\frac{\mathrm{I}-\mathrm{I_{th}}}{\mathrm{q}}\right). \end{aligned}$$

Using the values of the parameters given in Section 4.1, we find

$$I_{th} = 61.1\,\text{mA},\ \varepsilon' = 0.03,\ \theta = 476,\ \alpha = 3,\ T = 1428.57\,\text{s}.$$

4.2.2 Steady states and their stability

In this section, we discuss steady states of the dimensionless system (4.3). For simplicity, we consider the case of no nonlinear gain, in other words, $\varepsilon' = 0$. The laser equations are given by

$$\begin{aligned} \frac{dY}{dt} &= Z(1-i\alpha)Y + \gamma Y^*(t-\theta), \\ T\frac{dZ}{dt} &= P - Z - (1+2Z)\,|Y|^2, \end{aligned} \tag{4.4}$$

It is immediately obvious that system (4.4) has an steady state at $(Y,Z) = (0,P)$. This solution, which we refer to as the *trivial steady state*, corresponds to the off-state of the PCF laser. System (4.4) has two additional steady state solutions, which due to the $\mathbb{Z}_2$-symmetry of the PCF laser are symmetric counterparts of one another over a rotation of π of the E-plane. We refer to these solutions as the *non-symmetric steady states*.

4.2.3 Non-symmetric steady states

To compute the non-symmetric steady state solutions, we write system (4.4) in polar form by introducing

$$Y(t) = R(t)\exp(i\phi(t)). \tag{4.5}$$

Then system (4.4) becomes

$$\begin{aligned} \frac{dR}{dt}(t) &= Z(t)R(t) + \gamma R(t-\theta)\cos[\phi(t)+\phi(t-\theta)], \\ \frac{d\phi}{dt}(t) &= -\alpha Z(t) - \gamma\frac{R(t-\theta)}{R(t)}\sin[\phi(t)+\phi(t-\theta)], \\ T\frac{dZ}{dt}(t) &= P - Z(t) - (1+2Z(t))R(t)^2. \end{aligned} \tag{4.6}$$

A steady state solution, is a solution of the form

$$R(t) \equiv R_s,\ \phi(t) \equiv \phi_s,\ Z(t) \equiv Z_s, R(t-\theta) \equiv R_s,\ \phi(t-\theta) \equiv \phi_s.$$

Substituting this in (4.6) yields

$$\begin{aligned} 0 &= R_s Z_s + \gamma R_s \cos(2\phi_s), \\ 0 &= -\alpha Z_s - \gamma \sin(2\phi_s), \\ R_s^2 &= \frac{P - Z_s}{1 + 2Z_s}. \end{aligned} \tag{4.7}$$

Here we already see the double-angle $2\phi_s$ which is a consequence of the $\mathbb{Z}_2$-symmetry of the PCF laser and leads to the two non-symmetric steady state solutions for $\phi \in [0, 2\pi]$.

Since $R_s \neq 0$, (4.7) can be simplified to

$$\begin{aligned} Z_s &= -\gamma \cos(2\phi_s), \\ Z_s &= -\frac{\gamma}{\alpha} \sin(2\phi_s), \\ R_s^2 &= \frac{P - Z_s}{1 + 2Z_s}, \\ \text{or } 0 &= \alpha \cos(2\phi_s) - \sin(2\phi_s). \end{aligned} \tag{4.8}$$

This leads to the expression

$$\phi_s = \frac{\arctan \alpha}{2}. \tag{4.9}$$

We can see here that a variation of α does not create or destroy the solutions and, therefore, conclude for non-zero feedback ($\gamma > 0$) and without nonlinear gain ($\varepsilon = 0$) we do not find the saddle-node bifurcation leading to the creation of the two non-symmetric steady states. This is confirmed below by a linear stability analysis around the steady states.

4.2.4 Characteristic function

We now compute the characteristic function around a steady state. System (4.4) in polar form is given by

$$\frac{d}{dt} \begin{pmatrix} R(t) \\ \phi(t) \\ Z(t) \end{pmatrix} = F(R(t), \phi(t), Z(t), R(t-\theta), \phi(t-\theta)); \tag{4.10}$$

compare with (3.1).

In the notation used in Section 3.1, a steady state of the form (4.7) satisfies $F(R_s, \phi_s, Z_s, R_s, \phi_s) = 0$. Its stability is determined by the eigenvalues of the linearisation DF around the steady state, in other words,

$$\frac{d}{dt}\begin{pmatrix} R(t) \\ \phi(t) \\ Z(t) \end{pmatrix} = DF(R_s, \phi_s, Z_s, R_s, \phi_s)\begin{pmatrix} R(t) \\ \phi(t) \\ Z(t) \\ R(t-\theta) \\ \phi(t-\theta) \end{pmatrix} \tag{4.11}$$

where DF denotes the Jacobian of F with respect to all variables and is given by

$$DF(R_s, \phi_s, Z_s, R_s, \phi_s) = A\begin{pmatrix} R(t) \\ \phi(t) \\ Z(t) \end{pmatrix} + B\begin{pmatrix} R(t-\theta) \\ \phi(t-\theta) \\ Z(t-\theta) \end{pmatrix}, \tag{4.12}$$

where $A = D_1F(R_s, \phi_s, Z_s, R_s, \phi_s)$ and $B = D_2F(R_s, \phi_s, Z_s, R_s, \phi_s)$ are the derivatives of F in (4.10) with respect to the first and second variable. These are given by

$$A = \begin{bmatrix} Z_s & -\gamma R_s S_2 & R_s \\ \frac{\gamma S_2}{R_s} & -\gamma C_2 & -\alpha \\ -\frac{2R_s(1+2Z_s)}{T} & 0 & -\frac{(1+2R_s^2)}{T} \end{bmatrix}, \tag{4.13}$$

and

$$B = \begin{bmatrix} \gamma C_2 & -\gamma R_s S_2 & 0 \\ -\frac{\gamma S_2}{R_s} & -\gamma C_2 & 0 \\ 0 & 0 & 0 \end{bmatrix}, \tag{4.14}$$

where $C_2 = \cos(2\phi_s)$ and $S_2 = \sin(2\phi_s)$. The spectrum of the operator DF consists of discrete eigenvalues and is given by the roots λ of the characteristic function $\chi(\lambda) = \det(\lambda I - A - Be^{-\lambda\theta})$.

Using the facts, from (4.8), that

$$\begin{aligned} Z_s &= -\gamma C_2 = -\frac{\gamma}{\alpha}S_2 \\ S_2 &= \alpha C_2 \\ R_s^2(1+2Z_s) &= P - Z_s \end{aligned}$$

we find the simplified expression

$$\begin{aligned}\chi(\lambda) = \lambda^3 &+ \lambda^2\left[2\gamma C_2 + \frac{(1+2P)}{T(1-2\gamma C_2)}\right] \\ &+ \lambda\left[\frac{2}{T}\left(\frac{2\gamma C_2(1-\gamma C_2)+P}{1-2\gamma C_2}\right) + \gamma^2(1-e^{-2\lambda\theta})\right] \\ &+ \frac{1}{T}\left[\gamma^2(1-e^{-2\lambda\theta})\left(\frac{1+2P}{1-2\gamma C_2}\right)\right] \\ &+ \frac{1}{T}\left[2\gamma C_2(1+e^{-2\lambda\theta})(P+\gamma C_2)(1+\alpha^2)\right].\end{aligned} \tag{4.15}$$

Since ϕ_s depends only upon α, by fixing the values of α and P we can show how the stability of the steady states change as the feedback rate γ is varied. However, this is difficult as, due to the presence of the exponential $e^{-2\lambda\theta}$, the characteristic function $\chi(\lambda)$ has infinitely many roots which cannot be found analytically. In practice, the roots of equation (4.15) need to be found numerically, for example, by Newton's method.

There is one simple case: if $\chi(0) = 0$ there is a change in stability. This occurs for

$$P + \gamma\cos\left(2\arctan\left(\frac{\alpha}{2}\right)\right) = 0. \tag{4.16}$$

From equation (4.8), we find that (4.16) means that $R_s \equiv 0$. In other words, this case of $\lambda = 0$ gives us the first change in stability of the trivial steady state $(Y,Z) = (0,P)$ of the PCF laser.

To perform a full stability analysis of the PCF laser one needs to include nonlinear gain $\varepsilon \neq 0$ in equation (4.4). As mentioned above, also the characteristic function including nonlinear gain would have to be solved numerically. This is essentially the same as using DDE-BIFTOOL, which solves for equilibrium and its eigenvalues simultaneously, following solution branches with a predictor and Newton correction step. Indeed, in what follows we will compute solutions and stability of the PCF laser, with nonlinear gain, using DDE-BIFTOOL.

Chapter 5

Computing unstable manifolds in DDEs

This chapter is based on the paper [B. Krauskopf and K. Green, "Computing unstable manifolds of periodic orbits in delay differential equations", *J. Comp. Phys.*, to appear].

We present the first method to compute global unstable manifolds of saddle periodic orbits with one unstable Floquet multiplier in autonomous DDEs with one fixed delay. Specifically, we compute the 1D unstable manifold of a saddle fixed point in a suitable Poincaré map, which corresponds to a saddle periodic orbit of the DDE; see Section 3.2 for details. We remark that we speak of a 1D unstable manifold to stress that there is only one unstable eigenfunction. The unstable manifold of a periodic orbit of a DDE is a two-dimensional object in an infinite-dimensional space, but one whose intersection with the Poincaré plane is a one-dimensional curve.

The basic idea is to generalise the method for finite-dimensional maps in [39] (now implemented in the DSTOOL environment [2]) to the setting of DDEs. We use DDE-BIFTOOL to obtain the starting data required by our method. At present, the implementation is stand-alone, but it is envisaged that it will be integrated with DDE-BIFTOOL. Our method computes a piece of the unstable manifold of a set arclength, represented by a minimum number of points while satisfying pre-specified accuracy parameters. While the unstable manifold is a complicated object, its intersection with the Poincaré section, which we call the trace, is a one-dimensional curve. Despite effects of projection from an infinite-dimensional space, this curve conveys basically the same information as a one-dimensional unstable manifold of a fixed point of a planar map. This allows one to identify and study, for the first time, global bifurcations in DDEs. As an example, we show in Chapter 9 the break-up of a torus in the PCF laser and its subsequent transition to chaos in a crisis bifurcation.

5.1 Computing 1D unstable manifolds

Let $q \in \mathscr{C}_\Sigma$ be a saddle fixed point of a Poincaré map P defined by a section Σ transverse to the periodic orbit of the DDE that corresponds to q. We further assume that the periodic orbit has exactly one unstable Floquet multiplier, so that the linearisation $DP(q)$ of P has one unstable eigenvalue (which lies outside the unit circle). The goal is to compute the 1D unstable manifold $W^u(q)$.

The basic idea is to realize that practically any of the known algorithms for computing 1D unstable manifolds of saddle points of finite-dimensional maps can be generalised to the setting of DDEs by working on points in $\mathscr{C}_\Sigma$, instead of on points in a finite-dimensional space. While this sounds simple, all relevant operations, such as the iteration of the Poincaré map and interpolation, need to be interpreted and implemented as operations on points in $\mathscr{C}_\Sigma$, or rather on their discretisations as circular lists. This can be done by applying all respective operations *pointwise* to the elements of the respective circular lists; see Fig. 3.5.

We chose to implement the generalisation of the growth method in [39], because it computes the minimum number of points necessary to achieve an accurate representation of $W^u(q)$ (according to pre-specified accuracy parameters) by taking account of the curvature along the manifold. Using as few points as possible while maintaining a prescribed quality of the computation is particularly important in the setting of DDEs because every point in $\mathscr{C}$ is discretised and represented by a circular list of $(M+4) \times n$ real numbers; see Section 3.4.1. We remark that we do not adapt the integration step size during a computation, but use a fixed time step $\frac{\tau}{M}$ throughout.

5.1.1 Starting data

The starting data for a computation of an unstable manifold is the saddle periodic point q together with the knowledge of the linear eigenfunction $E^u(q)$, which we represent by a (generalised) vector $v = \{v(t) \mid t \in [-\tau, 0]\}$ whose elements are unit vectors. Both of these objects are represented as circular lists of length $M+4$, because of the integration method we use; see Section 3.4.1.

The saddle periodic point q can be found as follows. With the help of DDE-BIFTOOL, one continues periodic orbits of the DDE until a suitable saddle periodic orbit with one unstable eigenvalue is found. From this orbit one extracts the saddle periodic point q by choosing a point $q(0)$ in the prescribed section Σ together with its history. Because the required headpoint $q(0)$ will generally not be part of the mesh used

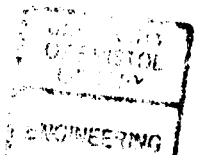

by DDE-BIFTOOL to represent the saddle periodic orbit, this step requires interpolation. Figure 3.3 shows a periodic orbit Γ of saddle-type computed by continuation with DDE-BIFTOOL, on which a periodic point $q \in \mathscr{C}_\Sigma$ has been selected. Notice that Γ intersects the chosen section Σ twenty times, so that P can be defined locally near q as the 20th return to Σ.

The next step is to find the vector v, which is a circular list defining a direction at every discretisation point of the delay interval. As finding v is not yet implemented in DDE-BIFTOOL, we use the following method. Choose a starting point close to q along some chosen direction v_0 and perform a small number m of iterations under the Poincaré map P, yielding $\tilde{v}_1 = P^m(q+\eta v_0) - q$. Normalising $\tilde{v}_1$ such that each element of the circular list is a unit vector gives a first approximation v_1 of v. This process can be repeated, yielding the approximation $v_2 = (P^l(q+\eta v_1) - q)/|P^l(q+\eta v_1) - q|$, and so on until one is satisfied with the accuracy. In Fig. 3.4 we illustrated v by plotting its every 100th element.

We finally remark that the above procedure finds the unstable eigenfunction v of the *strongest* unstable eigenvalue when there are other unstable eigenvalues. In this case, the algorithm described below computes the strong unstable manifold, which is tangent to this vector v.

5.1.2 Growing the manifold

With the knowledge of (approximations to) q and v one can implement one's favourite method for computing the associated 1D unstable manifold $W^u(q)$; for example those in [34, 39, 41, 51, 68].

The easiest method is *fundamental domain iteration*. Take a fixed number of points on the segment $[(q+\delta v), P(q+\delta v)]$ and iterate them under the Poincaré map P. Because of its invariance, all iterates will lie on $W^u(q)$ in good approximation. However, the distribution of points along $W^u(q)$ is generally poor. Nevertheless, the computational error of these points is determined only by the initial distance δ along v and the accuracy of the integration. There are several methods to ensure a suitable distribution of computed points along $W^u(q)$ [34, 51, 68]; see also the discussion in [39].

The method we decided to generalise to the setting of DDEs is that in [39], which entirely steps away from the idea of using a fundamental domain. The manifold $W^u(q)$ is represented by a list of points in $\mathscr{C}_\Sigma$ with the understanding that linear interpolation is used between consecutive points of this list. The idea is to find the next point p_{k+1} along

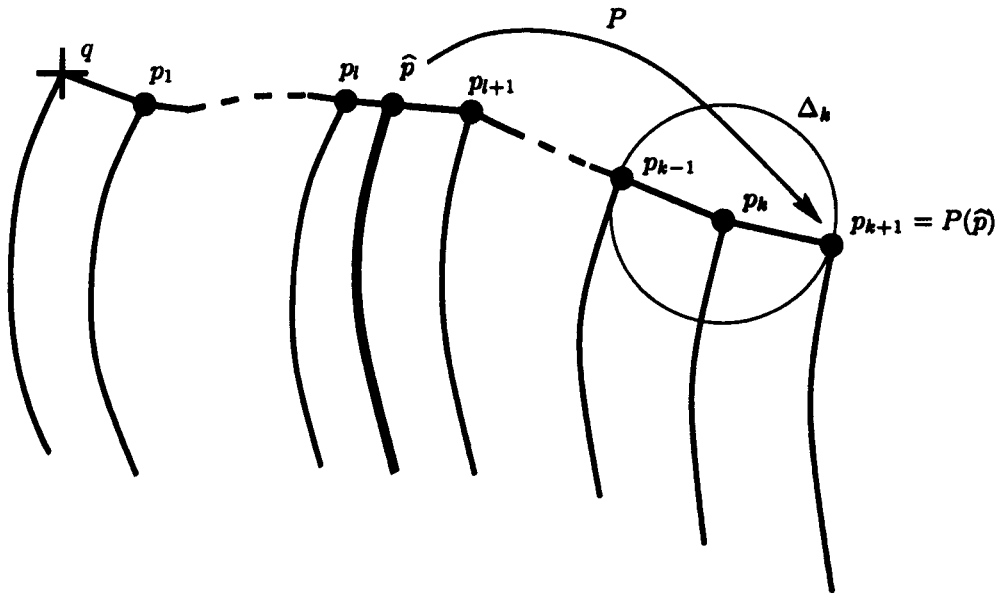

Figure 5.1: Sketch of the algorithm. The new point p_{k+1} lies at distance Δ_k from p_k, and it is found as the image of an interpolated point $\hat{p}$ on the part of $W^u(q)$ that was already computed. To indicate that we are dealing with a DDE we sketch this situation in projection onto X: the headpoint of each point lies in the section Σ.

$W^u(q)$ at some distance Δ_k from the last point p_k. This is done by finding a pre-image $\hat{p}$ of p_{k+1} in the part of $W^u(q)$ that was already computed. This idea is sketched in Fig. 5.1. The algorithm first finds the two points p_l and p_{l+1} between which $\hat{p}$ must lie and then determines $\hat{p}$ by bisection along the linear interpolation between p_l and p_{l+1}, such that the respective headpoints satisfy

$$(1-\varepsilon)\Delta_k < |P(\hat{p}(0)) - p_k(0)| < (1+\varepsilon)\Delta_k, \tag{5.1}$$

where ε is a pre-specified tolerance. In fact, one can take ε relatively large without loss of accuracy, which makes the method more efficient by reducing the number of bisection steps dramatically [39]. The linear interpolation between p_l and p_{l+1} is defined pointwise for all $t \in [-\tau, 0]$.

The distance Δ_k is adapted during the computation depending on the curvature of the trace of the manifold $W^u(q) \cap \Sigma$ in the section Σ. This is done because we want to represent the trace faithfully with as few points as possible; see Section 5.1.3 for a discussion of what this means in terms of the accuracy of our method. We use a criterion

used in [39] to accept the new point; for details see also [34]. The quantity

$$\alpha_k = \frac{|\bar{p}(0) - p_{k-1}(0)|}{|p_k(0) - p_{k-1}(0)|}, \tag{5.2}$$

is an approximation of the angle α between the line segments from $p_{k-1}(0)$ to $p_k(0)$ and from $p_k(0)$ to $p_{k+1}(0)$, where

$$\bar{p}(0) = p_k(0) + |p_k(0) - p_{k-1}(0)| \frac{(p_k(0) - p_{k+1}(0))}{|p_k(0) - p_{k+1}(0)|}. \tag{5.3}$$

Note that the angle is only computed in the section Σ.

The key is to check the conditions

$$\alpha_{\min} < \alpha_k < \alpha_{\max} \tag{5.4}$$

$$(\Delta\alpha)_{\min} < \Delta_k \alpha_k < (\Delta\alpha)_{\max}, \tag{5.5}$$

where the bounds are four pre-specified accuracy parameters. Condition (5.4) states that α_k should be small, while condition (5.5) controls the local interpolation error.

If both $\alpha_k < \alpha_{\max}$ and $\Delta_k \alpha_k < (\Delta\alpha)_{\max}$ then Δ_k is acceptable and the point $P(\hat{p})$ is accepted as the new point p_{k+1}. We keep the estimate for Δ_k unchanged, that is, $\Delta_{k+1} = \Delta_k$, except if both $\alpha_k < \alpha_{\min}$ and $\Delta_k \alpha_k < (\Delta\alpha)_{\min}$. Then we set $\Delta_{k+1} = 2\Delta_k$. If $\alpha_k \geq \alpha_{\max}$ or $\Delta_k \alpha_k \geq (\Delta\alpha)_{\max}$ then Δ_k is too large and p_{k+1} is not accepted. We set $\Delta_k = \frac{1}{2}\Delta_k$ and find a new candidate. At sharp bends of the manifold it may not be possible to ensure that $\alpha_k \geq \alpha_{\max}$ without making Δ_k impractically small. In this case, we accept the candidate p_{k+1} after all if $\Delta_k < \Delta_{\min}$ for a pre-specified number $\Delta_{\min}$. By choosing these accuracy parameters suitably, one can ensure that bends do not get cut off; see the discussion in [39].

The computation stops after a prescribed arclength distance of the trace $W^u(q) \cap \Sigma$ has been reached. However, it may be that $W^u(q) \cap \Sigma$ does not have such a large arclength, which occurs typically when the manifold ends up at an attracting fixed point. In which case, convergence of new points on the manifold is detected when Δ_k dips under a pre-specified value and the computation also stops.

5.1.3 On the accuracy

By a computation we mean the computation of a piece of one branch of $W^u(q)$ up to some prescribed arclength. When computing a global invariant manifold it is generally impossible to derive *a priori* bounds on the accuracy parameter one needs to choose in order to achieve a given accuracy. Furthermore, the accuracy of a calculation generally becomes worse as longer pieces of $W^u(q)$ are computed; compare [38, 39, 41]. Therefore, the only practical way of checking the accuracy of a computation in practice is to repeat it with increased accuracy and to compare the results. If the difference between the two approximations of $W^u(q)$ is smaller than some user-defined bound, then the computation can be accepted as accurate enough. This is certainly the strategy a user should adopt when using the algorithm presented here.

In the examples below we used a different method to illustrate the accuracy of our computations, namely to overlay points obtained by fundamental domain iteration, also starting from $q \pm \delta v$. While these overlaid points are not well distributed along $W^u(q)$, their computation does involve only integration, and not interpolation. It is therefore a good test to check that these points all lie on the approximation of $W^u(q)$ computed with our method; see already Section 5.1.5.

We now discuss briefly what contributes to the error of a computation, where we follow [39]. The first contribution to the overall error depends on the initial distance δ along $E^u(q)$ and on the distribution of mesh points along $W^u(q)$. As is the case for the algorithm for finite-dimensional maps, the initial error between $q \pm \delta v$ and $W^u_{\mathrm{loc}}(q)$ goes to zero with δ. Note that v is only known approximately, but the difference between v and $E^u(q)$ can be made arbitrarily small. Further, $W^u(q)$ is a collection of P-images of $W^u_{\mathrm{loc}}(q)$ and, due to the hyperbolicity of q, $W^u(q)$ is attracting in some neighbourhood U of q, so that the initial error will be damped in this neighbourhood. However, outside U the initial error grows with the number of iterates that are needed to cover the computed part of $W^u(q)$.

Outside U the total integration time is bounded from above implicitly by the maximal integration time used to compute (the finitely many iterations of) the Poincaré map. Therefore, the numerical integration is supposed to be accurate enough so that the integration error makes a negligible contribution to the overall error of the computation.

Because the manifold is grown by taking images of interpolated points, the interpolation error ε_l between the mesh points is important. The key thing is to keep the distance between two consecutive mesh points p_l and p_{l+1} small, depending on the curvature of

$W^u(q)$. It would be possible to check the curvature pointwise between three consecutive points for all points along the history, that is, for all $t \in [-\tau, 0]$. However, this would be computationally very expensive. Therefore, we chose to let Δ_k, the distance to the next point, depend only on the curvature of the trace $W^u(q) \cap \Sigma$. As in the finite-dimensional case, the distance, and hence the local interpolation error, between the *head points* $p_l(0)$ and $p_{l+1}(0)$ is controlled by keeping the product $\Delta_k \alpha_k$ small; see [34, 39].

The main reason for considering only the curvature of the trace is the following. It is ultimately the trace that we want to work with in applications, so that it makes sense to represent it well with as few points as possible. But further, this strategy also ensures that the local interpolation error between a pair of points p_l and p_{l+1} is bounded not just for $t = 0$ but for all $t \in [-\tau, 0]$, because the error $|p_{l+1}(t) - p_l(t)|$ depends continuously in t on $|p_{l+1}(0) - p_l(0)|$. Clearly, the error $|p_{l+1}(t) - p_l(t)|$ can be very large, but it does go to zero with $|p_{l+1}(0) - p_l(0)|$. Therefore, over a finite computation, the overall interpolation error is bounded.

We found that our strategy works well for the examples we considered: indeed the distance between p_l and p_{l+1} is nicely bounded for all l and $t \in [-\tau, 0]$, as can be seen in Fig. 5.5 below. We repeat that it is impossible to find *a priori* error bounds for this error, so that a computation should not be trusted blindly. Instead, as mentioned above, one should check the accuracy by increasing the accuracy bounds.

5.1.4 The bifurcation diagram

To illustrate our method we focus on a region where we find locking on a torus in the PCF laser (4.1) for $\kappa\tau \in [2.3, 2.6]$. This occurs at the beginning of the second 'bubble' of complicated dynamics; see Fig. 4.2. More details on the dynamics associated with the bifurcations of this torus can be found in Chapter 9.

The bifurcation diagram in Fig. 5.2 (a) was obtained by simulation: as in Section 4.1, for a new value of $\kappa\tau$ we integrated (4.1) starting from an attractor of the previous $\kappa\tau$, let transients die away, and then plotted $\hat{N} = (N/N_{sol} - 1) \times 10^3$ whenever the intensity $P(t) = |E(t)|^2$ crossed its average value in the positive direction [35]. Figure 5.2 (a) tells one what happens to the (main) attractor. It seems that a periodic orbit becomes unstable when a torus is born, the dynamics on this torus appears to be quasiperiodic at first, but then locks to a periodic orbit as five distinct branches appear. This new periodic orbit seems to undergo a torus bifurcation of its own. The new torus then suddenly disappears and a region of chaos is entered. We remark that there is no hysteresis when changing

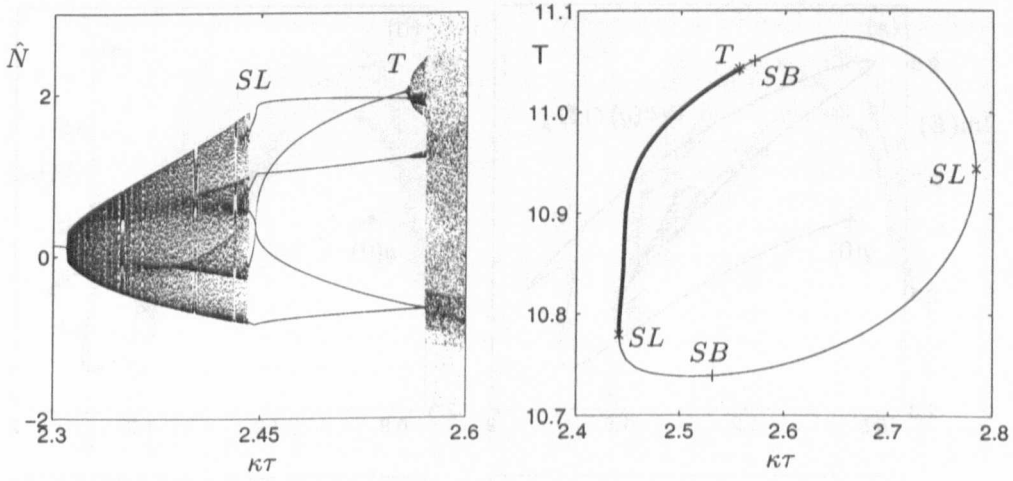

Figure 5.2: The bifurcation diagram for $\kappa\tau \in [2.3, 2.6]$ found by simulation (a), and the continuation with DDE-BIFTOOL of periodic orbits for $\kappa\tau \in [2.4, 2.8]$ (b). This should be compared to the more detailed Fig. 9.1.

the direction of the sweep in $\kappa\tau$.

As a first step to understand what is going on we started a DDE-BIFTOOL computation from the stable locked periodic orbit for $\kappa\tau = 2.445$ that we found by numerical integration. The result is shown in Fig. 5.2 (b), where the period of the respective periodic orbit is plotted against $\kappa\tau$. At $\kappa\tau \approx 2.441$ a stable and a saddle periodic orbit are born on the torus in a saddle-node bifurcation of limit cycles, which corresponds to the beginning of locked dynamics. The stable periodic orbit disappears in a torus bifurcation T that is detected at $\kappa\tau \approx 2.556$. The bifurcating torus is stable and it is like a hose winding around the original torus; see Chapter 9 for more details. Both the stable and the saddle periodic orbits undergo symmetry breaking bifurcations at the points denoted *SB*. They are in fact connected by a branch of non-symmetric periodic orbits; see Chapter 9 for details. On the lower branch between the points *SL* and *SB* the unstable periodic orbit has exactly one unstable Floquet multiplier.

5.1.5 1D unstable manifolds

Our method is implemented in C++ and its performance is demonstrated with the 1D unstable manifolds of periodic points associated with the periodic orbit in Fig. 3.3 of the PCF laser (4.1) for $\kappa\tau = 2.500$.

The periodic point q in Figs. 3.2 and 3.3 has the one-dimensional unstable linear

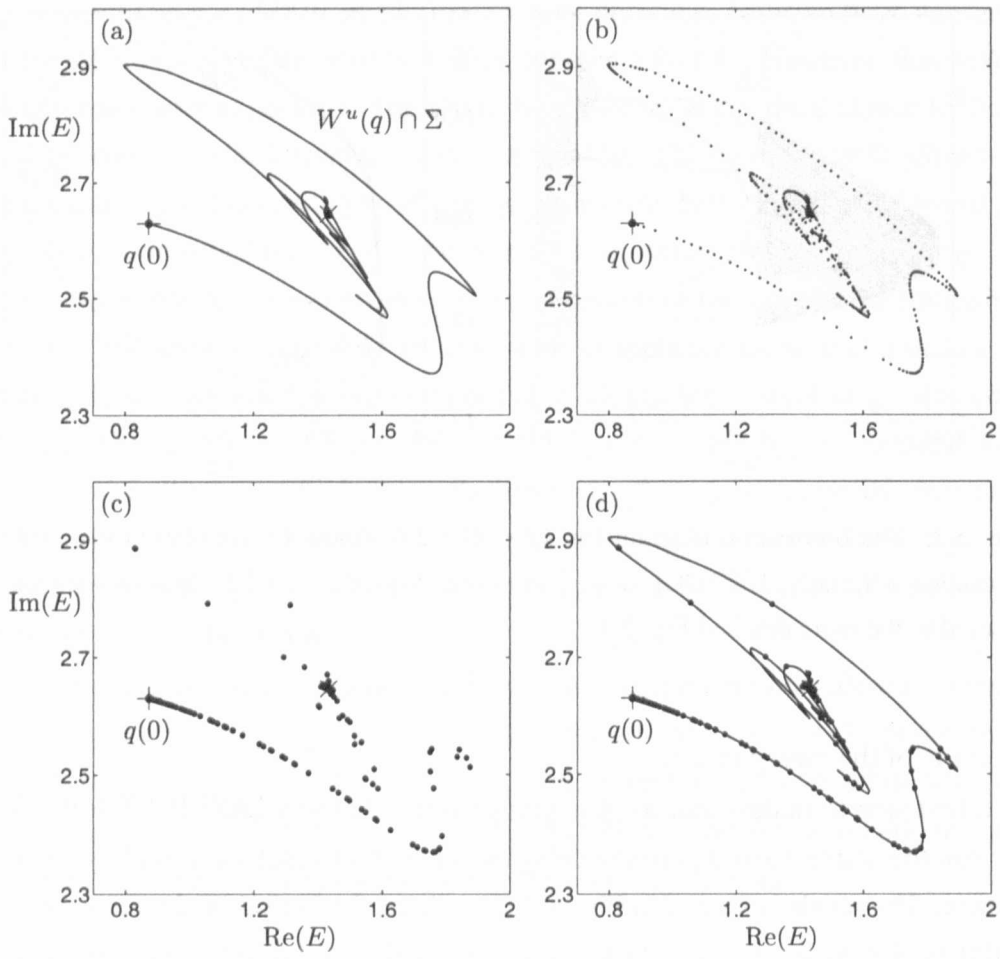

Figure 5.3: The trace of one branch of the unstable manifold of the saddle-point (+), which spirals into an attractor (×). Shown is the branch computed by our algorithm (a), the distribution of points along this branch (b), and the branch computed by 'naive' fundamental domain iteration (c). Part (d) shows that all points of (c) lie exactly on the computed branch from (a). This branch is for $\kappa\tau = 2.500$ and it is one of the branches in Fig. 5.4.

eigenspace $E^u(q)$ shown in Fig. 3.4. It was computed as described in Section 5.1.1 and stored in the normalised vector v. The approximation of $W^u(q)$ was started at a distance $\delta = 1.0 \times 10^{-4}$, while the accuracy parameters (detailed in Section 5.1.3) were $\alpha_{\min} = 0.2$, $\alpha_{\max} = 0.3$, $(\Delta\alpha)_{\min} = 1.0 \times 10^{-3}$, $(\Delta\alpha)_{\max} = 1.0 \times 10^{-4}$, $\Delta_{\min} = 1.0 \times 10^{-2}$ and $\varepsilon = 0.2$. Convergence of the manifold to a stable periodic orbit was detected when Δ_k fell below 5.0×10^{-4}.

Figure 5.3 (a) shows the trace in the section Σ defined by $N = 762.0$. Note that in this chapter, we rescaled $E(t)$ by a factor $1.0 \times 10^{-}2$ and $N(t)$ by a factor $1.0 \times$

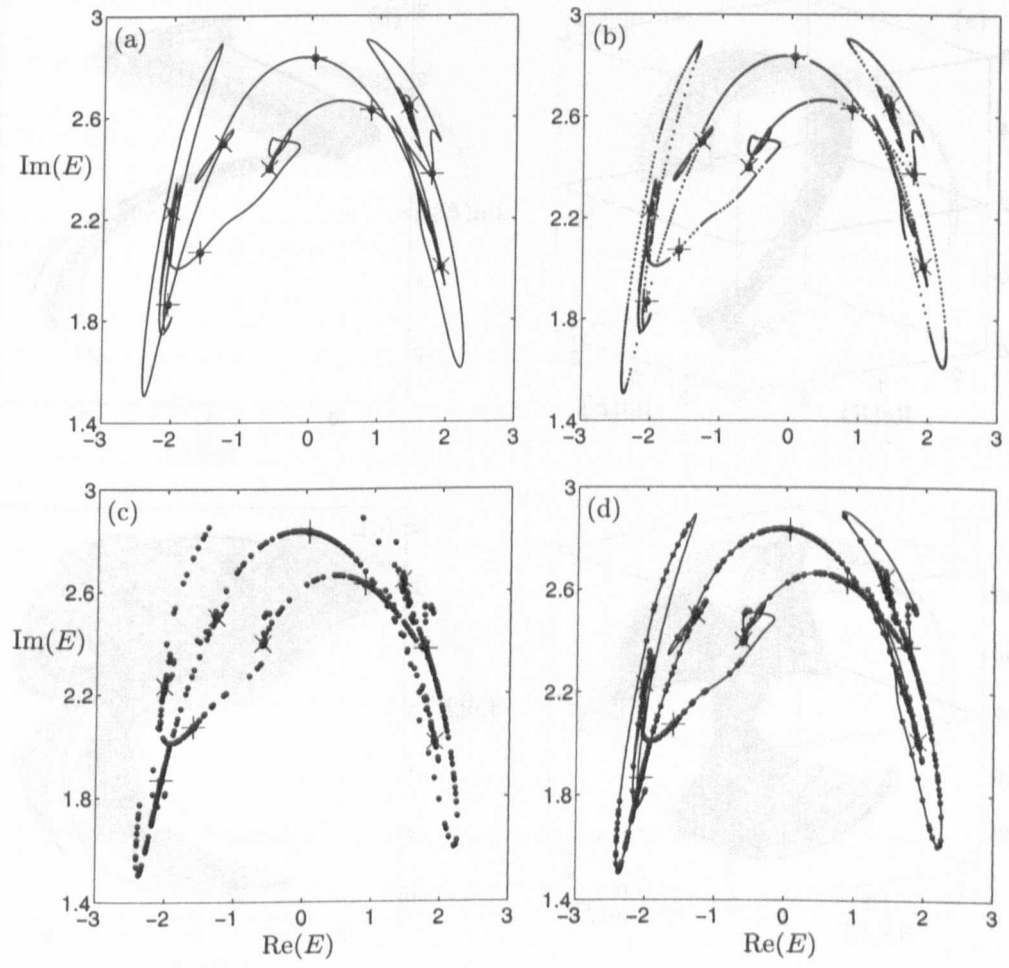

Figure 5.4: The traces of all branches in Σ emanating from both sides of the five saddle-points (+) converging to five attractors ($\times$) for $\kappa\tau = 2.500$. Panels (a)-(d) illustrate the performance of our algorithm as in Fig. 5.3.

10^-6; this does not change any of the dynamics. The points that were computed are shown in Fig. 5.3 (b), illustrating the distribution of points along $W^u(q) \cap \Sigma$ according to its curvature. Figure 5.3 (c) shows points obtained by iterating 100 initial points in a fundamental domain. While their distribution is such that one does not obtain a good image of the manifold, they lie on the trace of the true manifold to within the accuracy of integration. Indeed, an overlay of panels (a) and (c) in Fig. 5.3 (d) demonstrates the accuracy of the computed trace; the distance of the iterated points to the computed branch is less than 1.5×10^3. Note that the trace has self-intersections and sharp bends, which are both due to the projection, and eventually spirals into an attracting periodic point.

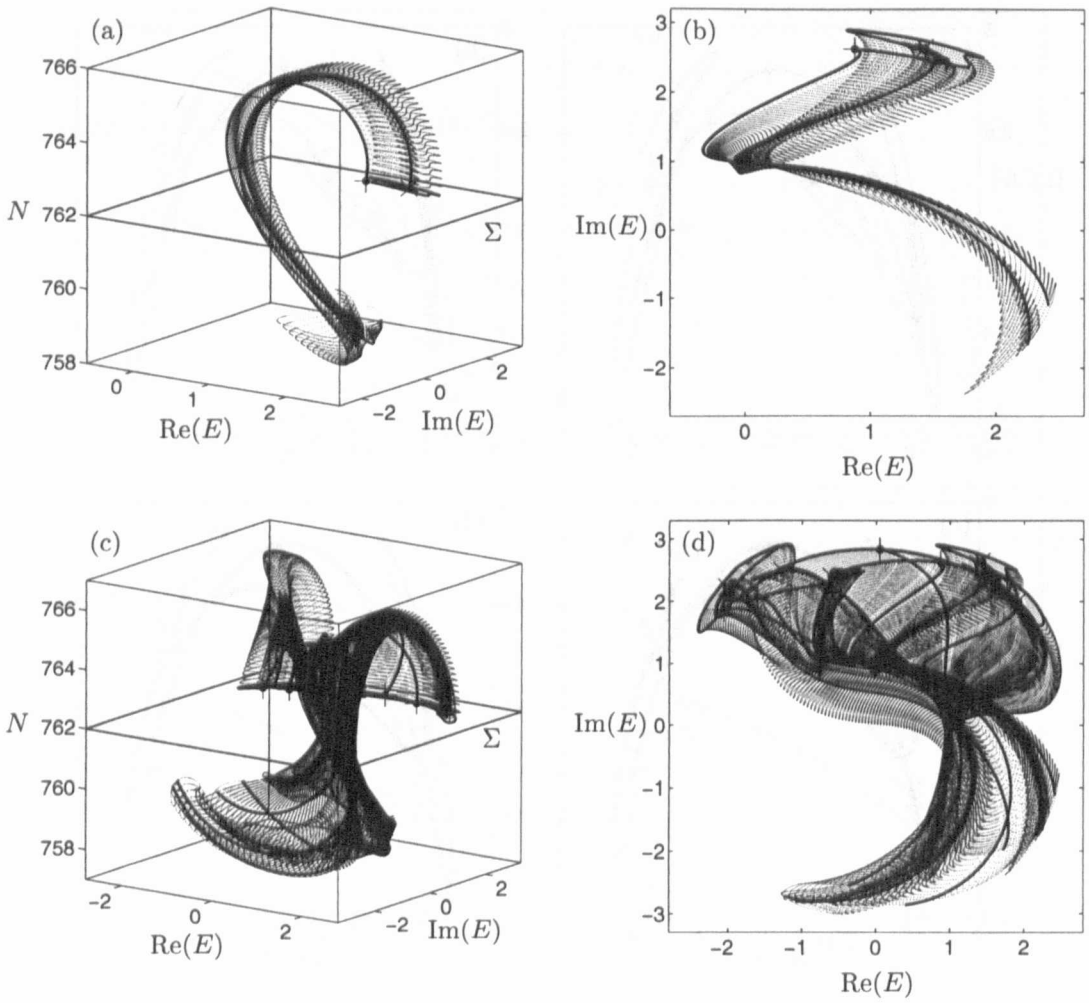

Figure 5.5: One branch of the unstable manifold (shown in Fig. 5.3 in the section Σ) in (E,N)-space (a) and in the E-plane (b), and all branches emanating from both sides of the five saddle-points (shown in Fig. 5.4 in the section Σ) in (E,N)-space (c) and in the E-plane (d).

Figure 5.4 (a) shows the overall picture with all branches of all five periodic points corresponding to the periodic orbit, rendered from the computed points in Fig. 5.4 (b). Points obtained by fundamental domain iteration in Fig. 5.4 (c) again lie on the computed 1D trace, as is illustrated in Fig. 5.4 (d). The five saddle points are mapped to each other by the 4th return to Σ. The unstable manifolds converge to five attracting equilibria, which correspond to the five branches in Fig. 5.2.

Finally, we show in Fig. 5.5 the manifolds corresponding to the traces in Figs. 5.3 and 5.4 in projection onto (E,N)-space (left column) and onto the E-plane (right col-

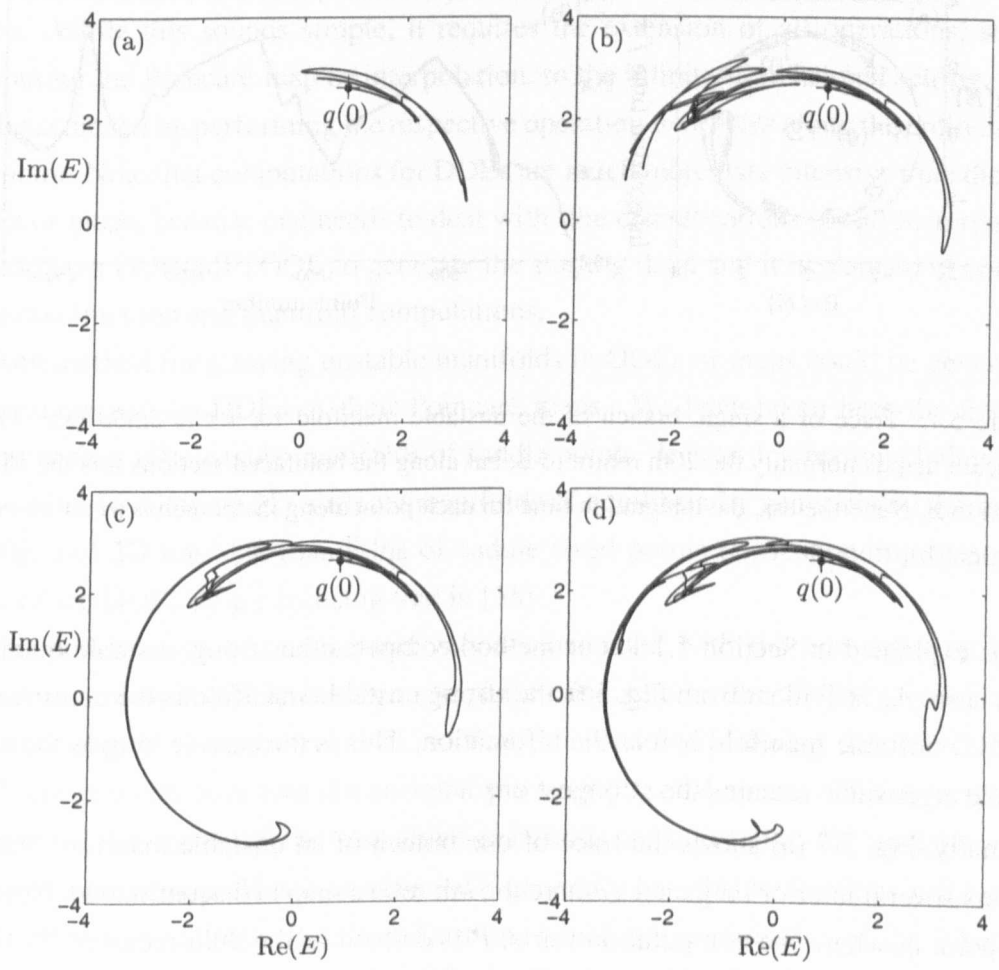

Figure 5.6: Trace of one branch of the unstable manifold of the saddle point q for $\kappa\tau = 2.5197$ (a), $\kappa\tau = 2.5271$ (b), $\kappa\tau = 2.5310$ (c), and the trace of the strong unstable manifold for $\kappa\tau = 2.5348$ (d).

umn). This reveals their intricate structure and highlights their high-dimensional nature. One can imagine the 1D trace in Σ as a 'curtain rail' along which the 'curtain' $W^u(q)$, made up of the headpoints in Figs. 5.3 (b) and 5.4 (b) together with their histories, is drawn during the growth process. This is shown in an animation accompanying this thesis, which can be accessed at `http://www.enm.bris.ac.uk/anm/preprints/2002r01.html`.

Figure 5.6 shows the development of a single branch of the unstable manifold of a fixed point when $\kappa\tau$ is changed through the symmetry-breaking bifurcation *SB* on the lower branch in Fig. 5.2. Figure 5.6 (d) corresponds to a situation where there are two unstable eigenvalues, the one that is involved in the symmetry-breaking being very small.

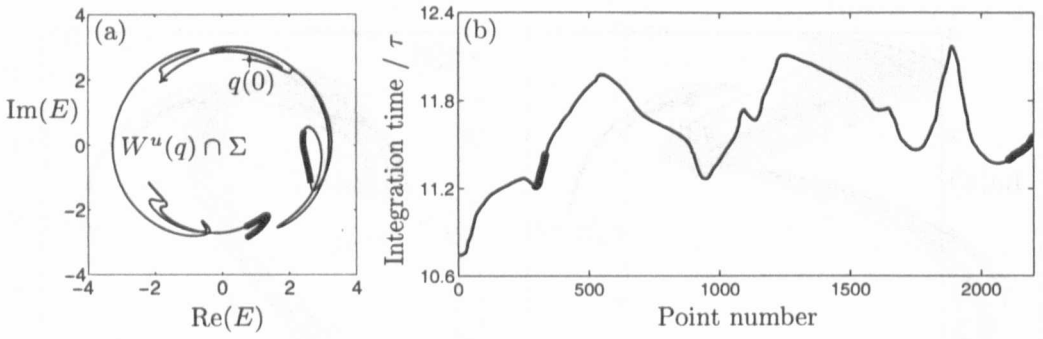

Figure 5.7: Trace of a single branch of the unstable manifold for $\kappa\tau = 2.550$ (a). The Poincaré map is normally the 20th return to Σ, but along the boldfaced sections it is the 18th return to Σ. Nevertheless, the integration time for each point along the branch is a continuous function (b).

As was explained in Section 5.1.1, our method computes the strong unstable manifold in this case. As is evident from Fig. 5.6, the strong unstable manifold is the continuation of the 1D unstable manifold before the bifurcation. This is the case as long as the same unstable eigenvalue remains the strongest one.

Finally, Fig. 5.7 (a) shows the trace of one branch of an unstable manifold that encounters several interior tangencies where the kth return map is discontinuous. Near the fixed point q, where the computation starts, P is defined as the 20th return to Σ. However, the boldfaced part of the trace corresponds to points where P is defined as the 18th return to Σ. In Fig. 5.7(b) we plotted the integration time for each computed point, and this clearly shows that, although the number of returns to Σ varies along the branch, the integration time is a continuous function. In other words, we are indeed following the right branch of P. As mentioned in Section 3.2, this technique of adapting the number of returns to the section during a computation allows one to compute longer pieces of $W^u(q)$.

5.2 Conclusions

We presented an algorithm for computing 1D unstable manifolds of saddle fixed points of a Poincaré map of a DDE, which generalises the method for finite-dimensional maps in [39] to Poincaré maps of DDEs. Behind this is the idea to work with points in the infinite-dimensional phase space of the DDE just like with points in a finite-dimensional

space. While this sounds simple, it requires the extension of all operations, such as computing the Poincaré map or interpolation, to the infinite-dimensional setting, which can be achieved by performing the respective operation *pointwise* along the entire history of a point. Note that computations for DDEs are much more data intensive than those for ODEs or maps, because one needs to deal with (the discretisations of) all histories. Our method uses DDE-BIFTOOL to generate the starting data, and it is planned to combine these continuation and manifold computations.

Any method for growing unstable manifolds in ODEs or maps could be generalised in the same way to DDEs or their Poincaré maps. We have taken here the first step by computing 1D unstable manifolds of saddle points. It is an interesting challenge for future work to compute 2D unstable manifolds of equilibria by generalising the method in [40], and 2D unstable manifolds of saddle fixed points (corresponding to periodic orbits of the DDE) by generalising that in [38].

The performance of our method was demonstrated with the rate equation model (4.1) of a semiconductor laser subject to phase-conjugate feedback. The physical space of this system is three-dimensional, so that the condition defining the Poincaré section Σ corresponds to a two-dimensional plane in physical space. This is very helpful because the traces of the respective manifolds look just like 1D unstable manifolds of a planar map. However, there will generally be self-intersections and isolated points of non-smoothness due to projection, which are a reminder of the inherently infinite-dimensional nature of the problem. While it is useful to work with a three-dimensional projection, we remark that it is not necessary that the *physical space* is three-dimensional. Alternatively, one can consider any three-dimensional space onto which one projects the infinite-dimensional phase space of the DDE, so that Σ again defines a two-dimensional subspace in this space.

Combined with the continuation of saddle periodic orbits, the computation of 1D manifolds presented here allows one to study *global bifurcations* in DDEs for the first time in much the same spirit as one does in ODEs. We demonstrate these methods in Chapter 9 with the example of the break-up of a torus and a subsequent crisis bifurcation to chaos.

Chapter 6

Bifurcation analysis of frequency locking

This chapter is based on the paper [K. Green and B. Krauskopf, "Bifurcation analysis of frequency locking in a semiconductor laser with phase-conjugate feedback", *Int. J. Bif. Chaos*, to appear].

We now perform a detailed bifurcation analysis of periodic orbits found in the PCF laser. In a bifurcation diagram obtained by simulation one finds stable periodic orbits interspersed with bubbles of more complicated dynamics, which for the most part are chaotic; again see Fig. 4.2. Between these bubbles the PCF laser is frequency locked, with its intensity oscillating close to some integer multiple of the fundamental external-cavity frequency [35]. One therefore refers to these stable periodic orbits as external-cavity modes (ECMs) of the PCF laser [26]. We remark that one also finds external-cavity modes in the COF laser, in which they are also referred to as continuous wave (CW) states. In the COF laser, a CW-state is a periodic solution with constant intensity and inversion, and a linearly evolving phase, of which solutions can be found analytically [59, 62]. We remark that this nature of the CW-states is a consequence of the S^1-symmetry of the COF laser. (Mathematically, the CW-states of the COF laser are group orbits of a steady state under the S^1-symmetry [42].) In contrast, the ECMs of the PCF laser are genuine periodic orbits with a periodically evolving intensity and inversion, and therefore cannot be found analytically. Hence the need to employ advanced numerical tools to investigate them.

Our main tool is DDE-BIFTOOL, which we use to continue the branches of symmetric periodic orbits on which each ECM lies. By detecting symmetry-breaking bifurcations along these symmetric branches we can switch to and continue branches of

non-symmetric periodic orbits. In fact, DDE-BIFTOOL was extended to allow branch switching at symmetry-breaking bifurcations to allow investigation of the PCF laser [28]. Continuation of these non-symmetric branches shows that a number of them end in Hopf bifurcations. Therefore, an immediate question is, are all ECMs of the PCF laser connected to one another via a non-symmetric steady state?

We answer this question to the positive, by giving a complete view of the ECMs and their bifurcating branches and show how they are connected. This includes identifying symmetric and non-symmetric branches, and all local bifurcations along those branches. We also identify homoclinic bifurcations of symmetric and non-symmetric periodic solutions, extra regions of stability and a bistability which leads to a hysteresis loop.

6.1 Continuation of the steady state

Figure 6.1 (a) shows continuation of the non-symmetric steady state, where we started from the stable (locked) state in Fig. 4.2. When the steady state is stable it is denoted by a thick curve and by a thin curve otherwise. The steady state is created at $\kappa\tau \approx 0.2794$ in a saddle-node bifurcation. It is destabilised in a sub-critical Hopf bifurcation H_1 at $\kappa\tau \approx 0.7487$. We also identify further Hopf bifurcations H_2 to H_6 when the steady state is already unstable, which we refer to later in Section 6.2. For a detailed discussion of this steady state we refer to Chapter 7. Here, we concentrate on the branches and bifurcations of periodic orbits associated with the ECMs.

6.2 Continuation of ECMs

Figures 6.1 (b) and 6.2 were obtained by continuation with DDE-BIFTOOL of the periodic orbits associated with each ECM. They show branches of periodic orbits, denoted by thick curves when stable, and by thin curves otherwise. In order to directly compare a periodic solution with a steady state in Fig. 6.1 (b) we plot a normalised amplitude $|\max(Re(E)) - \min(Re(E))|$ against $\kappa\tau$. This plot may appear complicated, but continuation of bifurcating (non-symmetric) branches clearly show that a number of them end in Hopf bifurcations, identified by a normalised amplitude of zero. Indeed, they end at the Hopf bifurcation points $H_{1,2,3,6}$ already indicated in Fig. 6.1 (a). This provides a connection between the different ECMs. The different branches corresponding to each ECM are further distinguished by the frequency ranges, as is highlighted in Fig. 6.2,

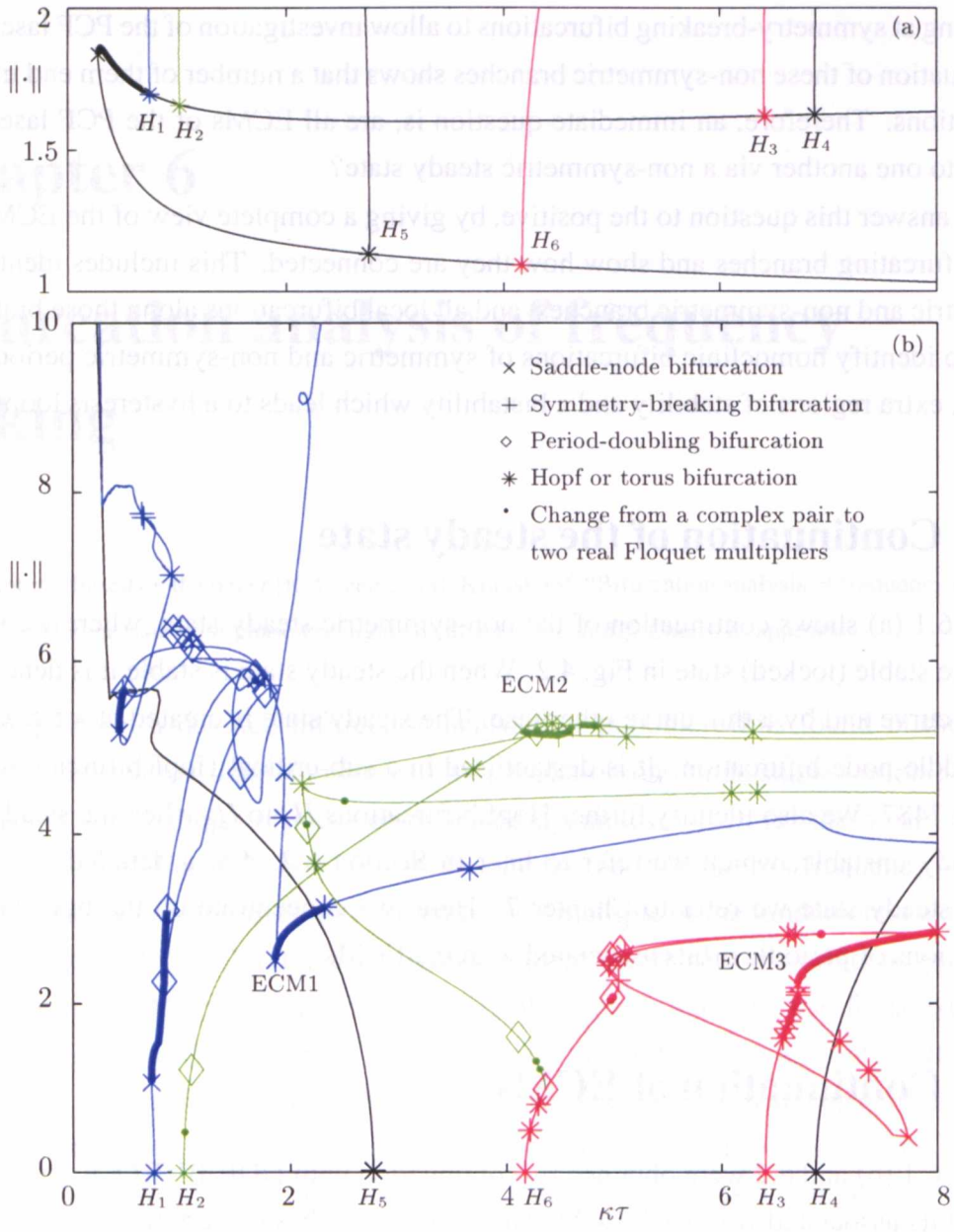

Figure 6.1: Bifurcation diagrams computed with DDE-BIFTOOL showing a normalised amplitude $\|\cdot\|$ versus $\kappa\tau$ for the steady states (a) and for all branches emanating from the external-cavity modes (b).

where they are plotted as a function of their period T. In both figures, all branches associated with the first, second and third external-cavity modes (ECM1–ECM3) are blue, green and red, respectively. The interval of $\kappa\tau \in [0,8]$ was chosen to contain the first three ECMs.

The main branches, on which the ECMs lie are of symmetric periodic orbits and, therefore, since symmetric periodic orbits cannot undergo period-doubling bifurcations [43, 57], all branches of periodic orbits which bifurcate from this main symmetric branch are non-symmetric. Another consequence of the $\mathbb{Z}_2$-symmetry is that for a symmetric periodic orbit the intensity is periodic with period T/2, while the period of the corresponding periodic orbit is T [42]. With this in mind, we see that ECM1 has a period ranging from 2.13τs to 2.47τs; ECM2 from 1.12τs to 1.19τs; and ECM3 from 0.71τs to 0.74τs, corresponding to frequency ranges of 1.21 GHz to 1.40 GHz; 2.51 GHz to 2.67 GHz; and 4.03 GHz to 4.20 GHz, respectively. This agrees well with the frequencies of 1.5 GHz, 3.0 GHz and 4.5 GHz mentioned in [35].

We computed the branches of periodic orbits which end at the Hopf points $H_{1,2,3,6}$ by starting from an ECM and continuing branches of periodic orbits. The two branches of periodic orbits emanating from H_4 and H_5 in Fig. 6.1 (a) are not directly related to the ECMs we considered and were computed from the periodic orbits created at the Hopf points. The branch emanating from H_5 leads to a branch of unstable periodic orbits which ends in a homoclinic bifurcation; see Section 6.4. We note that this branch is not connected to any of the symmetric branches on which the ECMs lie. The branch emanating from H_4 is connected to the symmetric branch on which the fourth ECM lies, which is beyond the scope of this study.

Notice that when plotted as a function of the period T, as in Fig. 6.2, the symmetric branches (on which the ECMs lie) have a similar shape. In each case, a lower part of the curve contains the ECM (thick curve) and is destabilised when decreasing $\kappa\tau$, in a saddle-node bifurcation of limit cycles; see also Section 6.3.

Figure 6.1 (b) clearly shows that bifurcating branches emanating from the main branches on which the ECMs lie end in Hopf bifurcations associated with the same non-symmetric steady state; identified in Figs. 4.2 and 6.1 (a). In order to provide a complete picture of these connections, these bifurcation diagrams should be looked at together with the phase portraits along them, shown in Figs. 6.3, 6.4 and 6.5, which we now discuss in some detail.

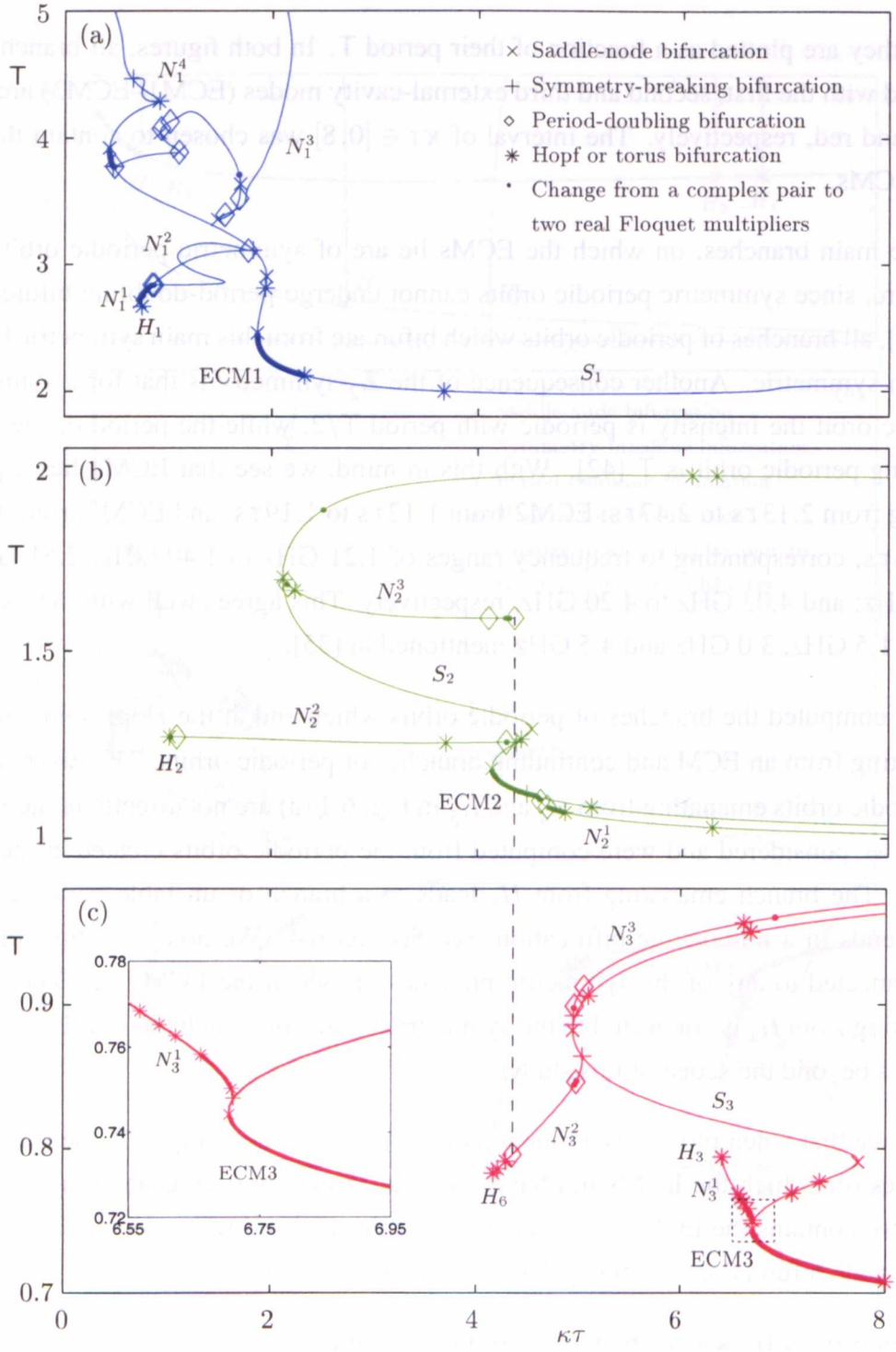

Figure 6.2: Bifurcation diagrams as in Fig. 6.1 (b), but plotted as period T versus $\kappa\tau$.

6.3 Bifurcations along branches

Figure 6.3 shows periodic orbits along the blue branch associated with ECM1. Along the symmetric branch S_1 (see panels (a1) to (a8)) the unstable periodic orbit, shown in panel (a1), is stabilised in a torus bifurcation at $\kappa\tau \approx 2.307$ as $\kappa\tau$ is decreased. The ensuing stable periodic orbit (see panel (a2)) is ECM1. It is destabilised in a saddle-node bifurcation of limit cycles at $\kappa\tau \approx 1.860$, where, as Fig. 4.2 shows, the attracting solution becomes chaotic. Continuing S_1 further, one sees the branch pass through a number of bifurcations before a symmetry-breaking bifurcation at $\kappa\tau \approx 0.471$ again stabilises the branch. The ensuing stable periodic orbit, shown in panel (a4), is not seen by simulation in Fig. 4.2 as it is connected to the main attractor of the system by branches of unstable solutions. A saddle-node bifurcation of limit cycles destabilises this periodic orbit at $\kappa\tau \approx 0.430$. Its period then starts to grow rapidly, and the periodic orbit spirals around the origin of the E-plane, this is shown in panels (a5) to (a7). This is evidence that the periodic orbit is approaching a homoclinic bifurcation. We detail this in Section 6.4.

Figures 6.3 (b1)–(b4) and (c1)–(c4) show non-symmetric periodic orbits along branches N_1^1 and N_1^2, respectively. Along N_1^1, we see a clear change in symmetry as the branch extends from the symmetry-breaking bifurcation point on S_1 at $\kappa\tau \approx 1.822$. Initially the periodic orbit, shown in panel (b1), is almost symmetric but quickly loses symmetry, before shrinking about the non-symmetric steady state (see panel (b4)) associated with the Hopf bifurcation H_1. This change in symmetry can also be seen along the period-two branch N_1^2, which bifurcates from N_1^1 at $\kappa\tau \approx 0.843$ (marking the start of the period doubling cascade shown in Fig. 4.2 and shown later in Fig. 7.1 (a)) and rejoins N_1^1 close to the symmetric branch S_1 at $\kappa\tau \approx 1.770$. The period-two orbits in panels (c1) to (c4) should be directly compared to the period-one orbits in panels (b1) to (b3).

The phase portraits along the non-symmetric branch N_1^3 are given in Fig. 6.3 (d1) to (d8). The branch N_1^3 bifurcates from S_1 at the symmetry-breaking bifurcation at $\kappa\tau \approx 0.471$. Again, the initial stable periodic orbit, shown in panel (d1), is almost symmetric. It should be compared with the symmetric periodic orbit in panel (a4). However, stability is quickly lost in a period-doubling bifurcation. The ensuing unstable periodic orbits in panels (d2) to (d8) quickly lose symmetry. They increasingly look like 'one half' of the symmetric periodic orbits of panels (a5) to (a8). As one moves along N_1^3, one 'arm' of the periodic orbit retracts about the origin of the E-plane. However, an image of the larger arm along with its symmetric counterpart is directly comparable with the symmetric orbits along S_1. Finally, as with S_1 (see panel (a8)), N_1^3 ends in a homoclinic bifurcation.

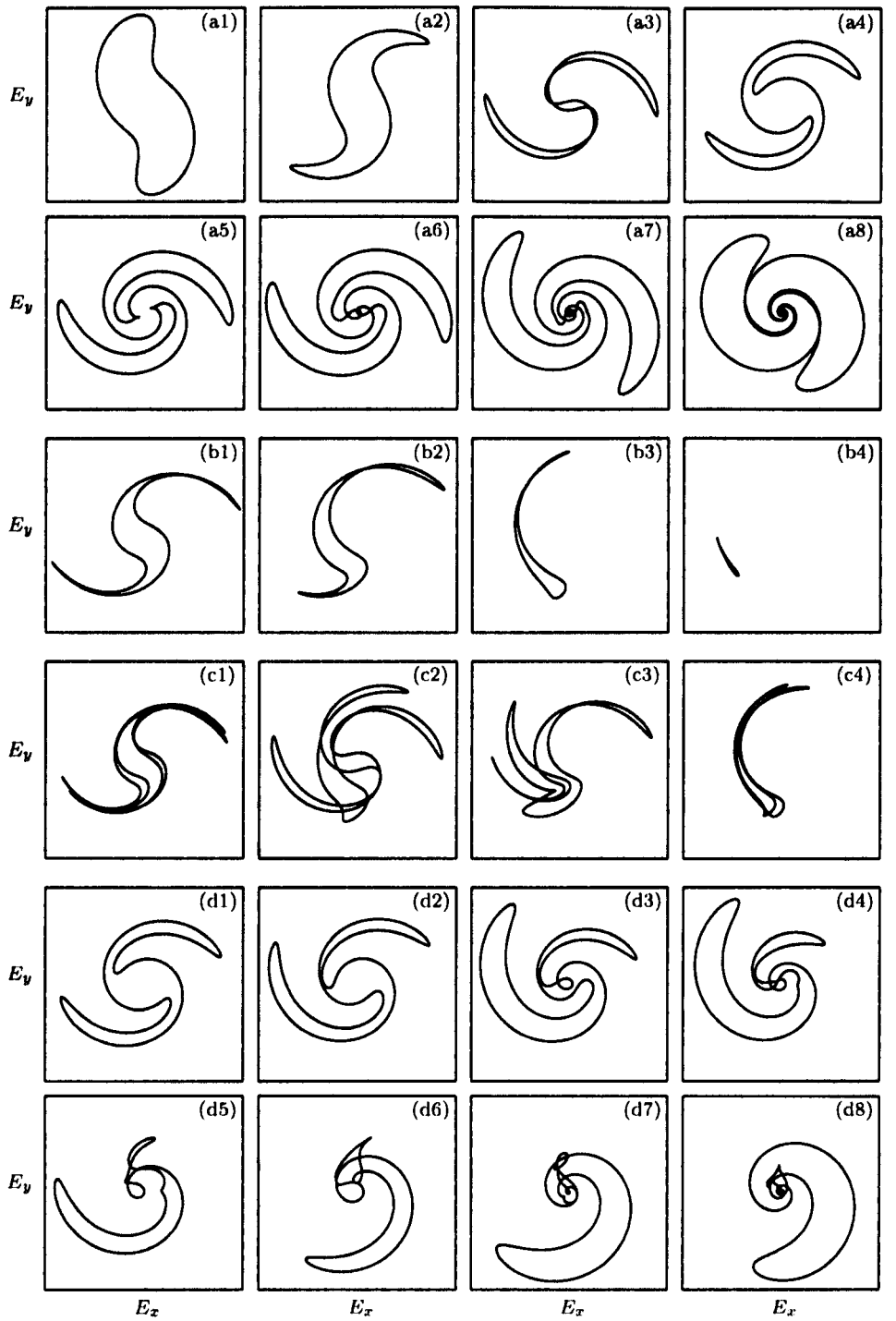

Figure 6.3: Phase portraits along the branches S_1 (a1)-(a8), N_1^1 (b1)-(b4), N_1^2 (c1)-(c4) and N_1^3 (d1)-(d8); shown in projection onto the E-plane. From (a1) to (a8) $\kappa\tau$ takes the values 2.0617, 1.9366, 1.1850, 0.4410, 0.9155, 0.7898, 0.4905 and 0.0973; from (b1) to (b4) $\kappa\tau$ takes the values 1.7929, 1.2871, 0.7964 and 0.7379; from (c1) to (c4) $\kappa\tau$ takes the values 1.7507, 1.1496, 1.3869 and 0.8458; and from (d1) to (d8) $\kappa\tau$ takes the values 0.4763, 0.7226, 0.9286, 1.3411, 1.6819, 1.5093, 2.1572 and 2.2414.

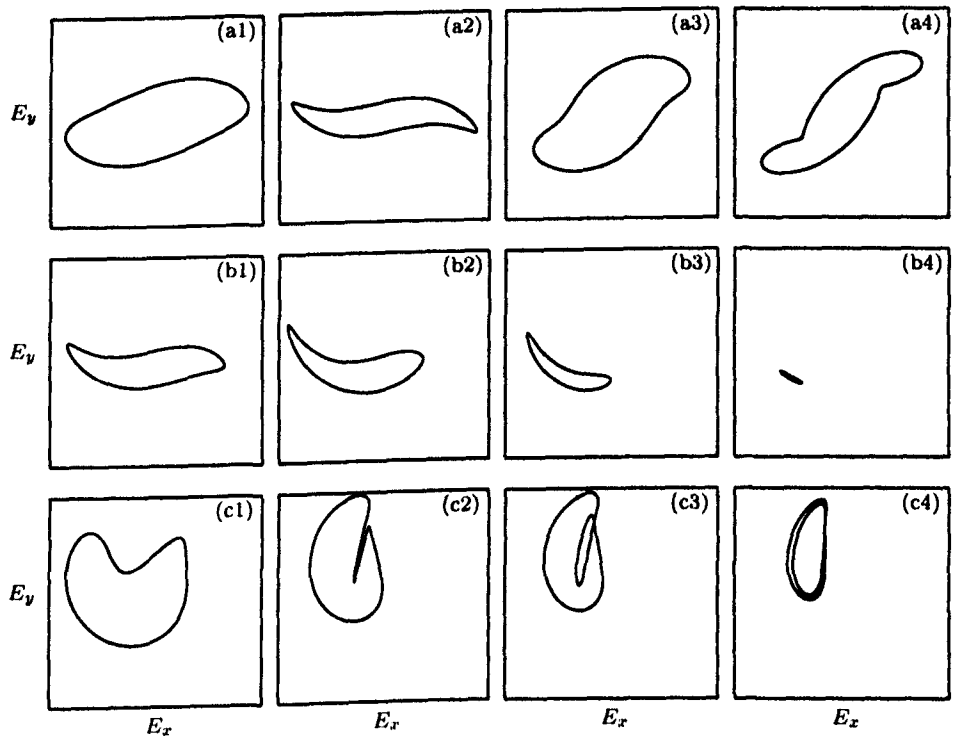

Figure 6.4: Phase portraits along the branches S_2 (a1)-(a4), N_2^2 (b1)-(b4) and N_2^3 (c1)-(c4); shown in projection onto the E-plane. From (a1) to (a4) $\kappa\tau$ takes the values 4.3221, 4.4738, 2.3500 and 6.6011; from (b1) to (b4) $\kappa\tau$ takes the values 4.2600, 3.3589, 1.5593 and 1.0411; and from (c1) to (c4) $\kappa\tau$ takes the values 2.3097, 3.6737, 4.0689 and 4.3529.

An example of this non-symmetric homoclinic orbit, which we investigate in detail in Section 6.4, is shown in panel (d8).

Periodic orbits associated with ECM2 and ECM3 are shown in Figs. 6.4 and 6.5. The symmetric periodic orbits along S_2 and S_3 are shown in Figs. 6.4 (a1)–(a4) and 6.5 (a1)–(a4), respectively. In both cases, no qualitative change in the shape of the orbits is observed. Figures 6.4 (b1)–(b4), 6.5 (b1)–(b4) and 6.5 (c1)–(c4) show how bifurcating non-symmetric branches N_2^2, N_3^1 and N_3^2 end at the Hopf bifurcations H_2, H_3 and H_6. As in the case of branch N_1^1, in all cases, the periodic orbit is seen to lose symmetry as one moves from the bifurcation point, before shrinking about the non-symmetric steady state associated with the respective Hopf bifurcation.

Apart from the Hopf bifurcations associated with ECM2 and ECM3 we find other bifurcation scenarios. The dashed line in Figs. 6.2 (b) and (c) represents a period-doubling bifurcation connecting the branches N_2^3 and N_3^2, and therefore, forms another connection between ECM2 and ECM3. Figure 6.4 (c1)–(c4) shows the development of the periodic

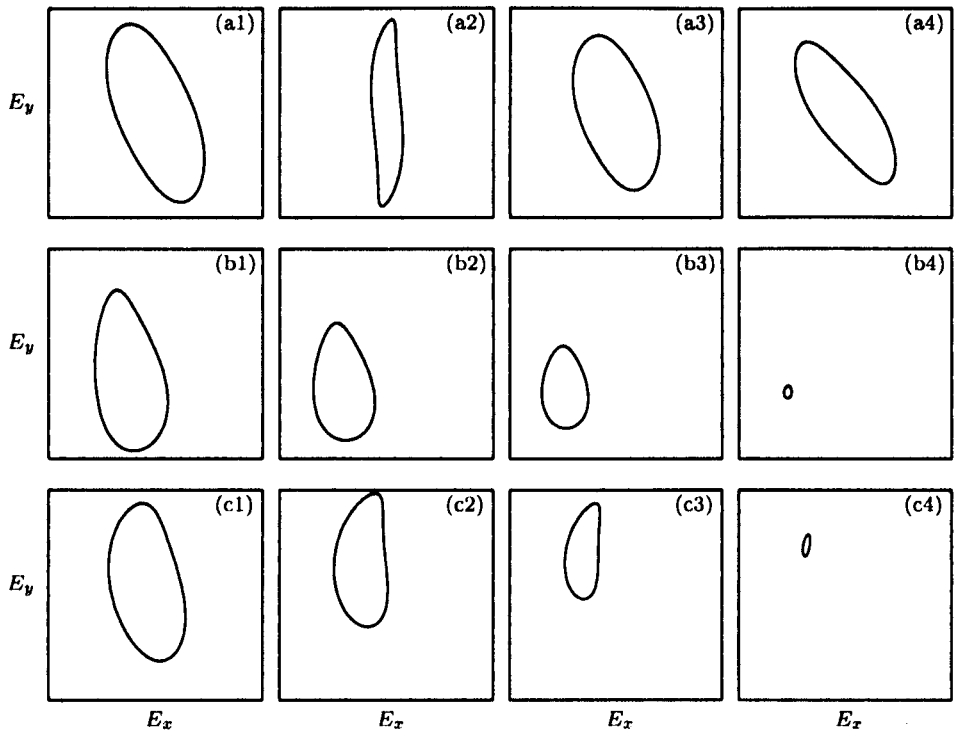

Figure 6.5: Phase portraits along the branches S_3 (a1)-(a4), N_3^1 (b1)-(b4) and N_3^2 (c1)-(c4); shown in projection onto the E-plane. From (a1) to (a4) $\kappa\tau$ takes the values 7.5033, 7.5696, 4.9669 and 7.3940; from (b1) to (b4) $\kappa\tau$ takes the values 6.6967, 6.6023, 6.5023 and 6.4098; and from (c1) to (c4) $\kappa\tau$ takes the values 5.0243, 4.6283, 4.3615 and 4.1800.

orbit along N_2^3. It is clearly seen to 'fold' over on itself, resulting in a period-two orbit in the local vicinity of the period-doubling bifurcation point, shown in panel (c4). This is a period-doubled version of the periodic orbit we find on N_3^2, shown in Fig. 6.5 (c3). This connection is also clearly shown in Fig. 6.1 (a). The dashed box in Fig. 6.2 (c), enlarged in the inset, contains a hysteresis loop. Continuing ECM3 for decreasing $\kappa\tau$ shows that it is destabilised in a saddle-node bifurcation of limit cycles at $\kappa\tau \approx 6.703$. The solution then jumps to the non-symmetric branch N_3^1 which is stable up until a torus bifurcation at $\kappa\tau \approx 6.660$. However, starting from and continuing the stable periodic orbit on N_3^1 for increasing $\kappa\tau$ shows that it is destabilised in another torus bifurcation at $\kappa\tau \approx 6.707$. Simulation has shown that the ensuing torus is short lived and the solution jumps to ECM3 on S_3. Thus, for $\kappa\tau \in [6.703, 6.707]$ one observes a region of bistability between the stable symmetric periodic orbit of S_3 and the stable non-symmetric periodic orbit of N_3^1.

6.4 Homoclinic orbits

We now discuss in detail the homoclinic orbits identified in Fig. 6.1 (b), found at the end of the branches S_1 and N_1^3, and at the end of the branch emanating from the Hopf bifurcation H_5.

A routine allowing computation of connecting orbits using projection boundary conditions has been recently added to DDE-BIFTOOL [55]. A homoclinic orbit can be approximated by a very high period orbit, but by using projection boundary conditions one generally achieves a more accurate orbit, particularly if one then wants to follow it in parameters. This routine also gives stability information of the associated saddle steady states (or homoclinic points). In Section 6.3, we identified two possible homoclinic orbits of branches S_1 and N_1^3, where the period of the orbit started to increase rapidly for small changes in $\kappa\tau$. It was shown in Figs. 6.3 (a1)–(a8) and (d1)–(d8) that both periodic orbits develop in a similar fashion, until finally the symmetric orbit, shown in panel (a8), appears as an image of the non-symmetric orbit, shown in panel (d8), together with its symmetric counterpart. We also identified a homoclinic orbit at the end of the branch emanating from the Hopf bifurcation H_5.

All three homoclinic orbits are shown in Fig. 6.6. The saddle point involved in the homoclinic orbit in each case is the trivial saddle steady state at $(Re(E), Im(E), N) = (0, 0, 813.75)$. This trivial equilibrium does not depend on $\kappa\tau$. This was confirmed with DDE-BIFTOOL, which also gives stability information about the saddle point involved in the bifurcation. For all orbits, this saddle point has a leading real eigenvalue $\lambda_1 \approx -0.333$ and a complex conjugate pair of unstable eigenvalues $\lambda_{2,3} \approx 19.6 \pm i58.9$. In all cases, this corresponds to the approximate one-dimensional attraction of the trajectory towards the homoclinic point, along its stable manifold, and the two-dimensional spiral from the homoclinic point, along its unstable manifold, shown in Fig. 6.6.

The upper row of Fig. 6.6 shows the homoclinic orbits at the end of the symmetric branch S_1 (a), the non-symmetric branch N_1^3 (b) and the branch emanating from the Hopf bifurcation H_5 (c) in projection onto (E,N)-space. The lower row shows the same orbits projected onto the E-plane. All orbits shown were converted from high period to homoclinic orbits using the new DDE-BIFTOOL routine. However, there are still difficulties with convergence of the Newton iteration. It can clearly be seen that the non-symmetric homoclinic orbit in column (c) is exactly 'one half' of the homoclinic orbit in column (a). The remainder of the retracting 'arm' detailed in Section 6.3 can be seen in column (b). Investigations show that this 'arm' is not a numerical artifact. In fact, we

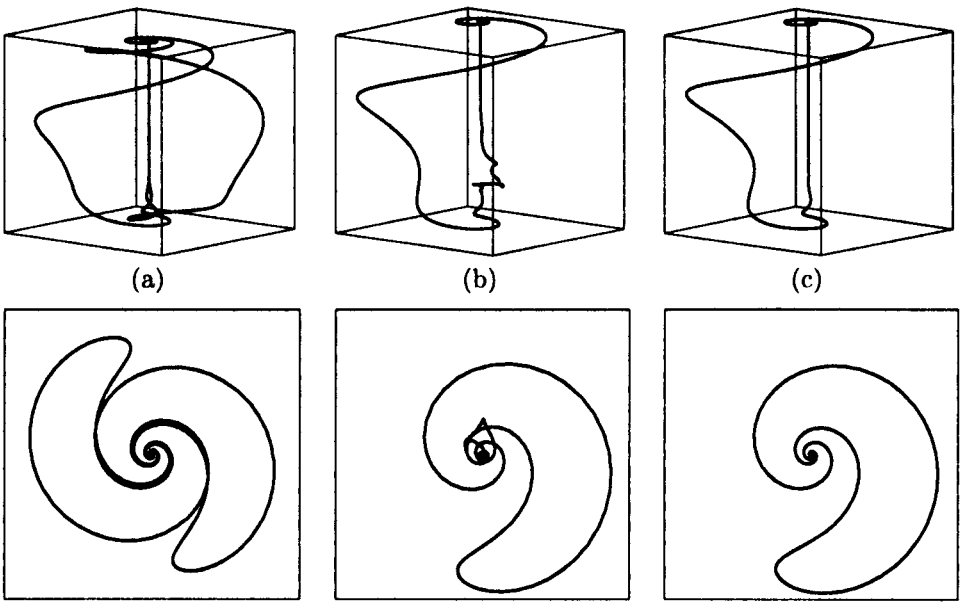

Figure 6.6: Homoclinic orbits at the end of branches S_1 (a), N_1^3 (b) and the branch emanating from H_5 (c), shown in projection onto (E,N)-space and onto the E-plane respectively; the box is $[-800,800]\times[-800,800]\times[7.45\times10^8,8.10\times10^8]$ and the square is $[-1000,1000]\times[-1000,1000]$.

were able to obtain convergence of the Newton iteration to this homoclinic orbit, so that it can be continued in two parameters.

Investigations using a 2-parameter continuation of the non-symmetric steady state, identified in Section 6.1, has revealed a T-point bifurcation [20]. More specifically, this codimension-two bifurcation occurs when a heteroclinic connection between the two non-symmetric equilibria, detailed in Chapter 7, collides with the trivial saddle steady state. The existence of a T-point bifurcation implies the existence of a logarithmic spiral of homoclinic orbits associated with the trivial steady state. It is an organising centre of heteroclinic and homoclinic orbits. In fact, the two-dimensional unstable manifold of the trivial saddle steady state appears to form an upper organising boundary for the dynamics of the PCF laser. A full analysis of the T-point bifurcation is given in Chapter 8.

6.5 Conclusions

We investigated periodic orbits in the PCF laser using recently developed continuation techniques. Stable symmetric periodic orbits corresponding to ECMs of the PCF laser have been shown to exist at different frequency ranges. Moreover, by continuing unstable periodic orbits we have provided a complete picture of how the ECMs of the PCF laser are connected to one another. We showed how bifurcating branches of non-symmetric periodic orbits ended in Hopf bifurcations. In each case, the respective Hopf point was shown to be associated with the same non-symmetric steady state and, therefore, a connection between the different ECMs of the PCF laser was found.

We identified all bifurcations of periodic orbits along the branches and key bifurcations were explained with phase portraits. This included a period-doubling bifurcation between two branches associated with different ECMs. A bistability between a symmetric periodic orbit and non-symmetric periodic orbits leading to a hysteresis loop was identified. Furthermore, some branches were shown to end in homoclinic bifurcations associated with the trivial steady state of the PCF laser.

Chapter 7

Global bifurcations and bistability at the locking boundaries

This chapter is based on the paper [K. Green and B. Krauskopf, "Global bifurcations and bistability at the locking boundaries of a semiconductor laser with phase-conjugate feedback", *Phys. Rev. E*, 66(016220), 2002].

We now concentrate on the mechanism of locking in a semiconductor laser with phase-conjugate feedback. Physically, in its locking range the PCF laser is both frequency locked and phase locked to the frequency of the PCM pump laser. Unlike the case of a COF laser, phase locking in a PCF laser does not depend on the feedback phase. In particular, phase locking results in an ultra-narrow laser line-width which has been shown to be stable even with the addition of noise [23]. By continuing steady states and computing the unstable manifolds of saddle points we find that hysteresis loops and global bifurcations are involved in the mechanism of locking in the PCF laser.

We compute the one-dimensional (1D) unstable manifolds of saddle steady states with one unstable eigenvalue. Each 1D unstable manifold has two branches, which are computed by integrating from two initial conditions along the associated 1D unstable eigendirection close to but on different sides of the steady state. This eigendirection can be found by an iterative approach [36] or with a new routine that was recently added to DDE-BIFTOOL. Knowing at which attractor the branches of 1D unstable manifolds end up is crucial for understanding the global dynamics, as will become clear in Section 7.2.

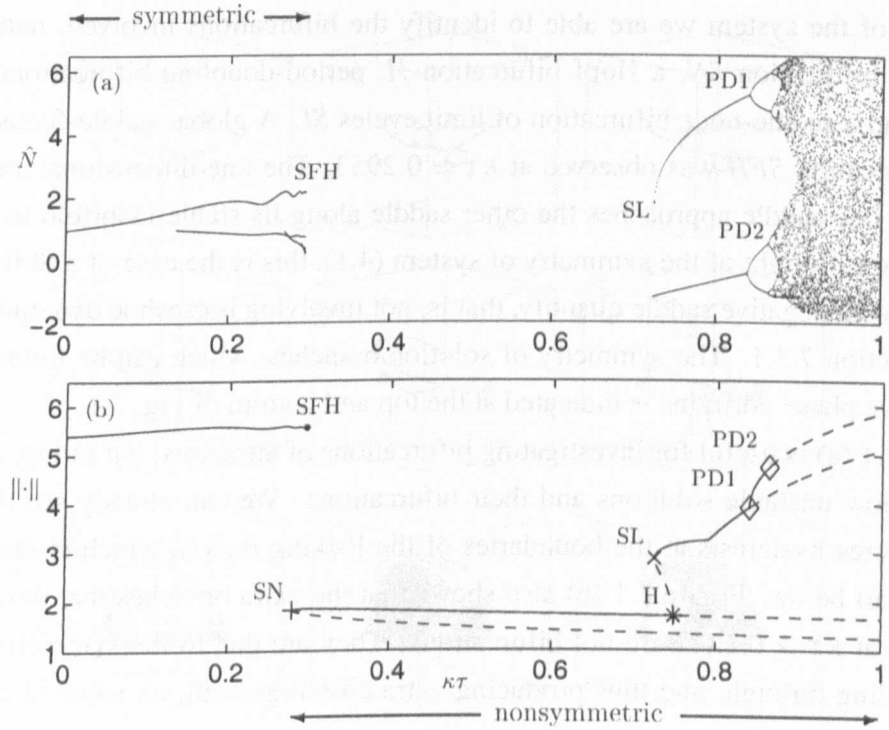

Figure 7.1: Bifurcation diagram obtained by simulation showing normalised inversion $\hat{N}$ versus the feedback strength $\kappa\tau$ (a), and computed with DDE-BIFTOOL showing a normalised amplitude versus $\kappa\tau$ (b); see text for details.

7.1 Bifurcation diagrams

Figure 7.1 contains two bifurcation diagrams. As in Section 4.1, to obtain Fig. 7.1 (a) we integrated system (4.1) and plotted (after transients died away) the normalised value of the inversion $\hat{N} = (N/N_{sol} - 1) \times 10^3$ whenever the intensity $P(t) = |E(t)|^2$ crossed its average value in the positive direction [35]. The region with no points corresponds to a locked solution. A small number of points correspond to a periodic solution. A large number of points correspond to chaotic dynamics. Due to the presence of hysteresis discussed below, the periodic solution for $\kappa\tau \in [0.0000, 0.2953]$ was computed for increasing $\kappa\tau$, while the periodic solution for $\kappa\tau \in [0.7487, 0.9004]$ was computed for decreasing $\kappa\tau$.

Figure 7.1 (b) was obtained by continuation with DDE-BIFTOOL. For steady states we plot $Re(E)$ and for periodic solutions we plot $|\max(Re(E)) - \min(Re(E))|$, offset by the $Re(E)$-value of the steady states at the Hopf point. Attracting solutions are drawn as solid curves, while unstable solutions are drawn as dashed curves. By studying the

eigenvalues of the system we are able to identify the bifurcations involved, namely a saddle-node bifurcation *SN*, a Hopf bifurcation *H*, period-doubling bifurcations *PD1* and *PD2*, and a saddle-node bifurcation of limit cycles *SL*. A global saddle-focus heteroclinic bifurcation *SFH* was observed at $\kappa\tau \approx 0.2953$. The one-dimensional unstable manifold of one saddle approaches the other saddle along its stable manifold in a spiralling fashion. In light of the symmetry of system (4.1), this is the case of a Shil'nikov bifurcation with negative saddle quantity, that is, not involving horseshoe dynamics; see [43] and Section 7.3.1. The symmetry of solution branches, which can be found from the respective phase portraits, is indicated at the top and bottom of Fig. 7.1.

Figure 7.1 (a) is useful for investigating bifurcations of attractors, but in Fig. 7.1 (b) we also follow unstable solutions and their bifurcations. We can already see that the system features hysteresis at the boundaries of the locking region, which is discussed in more detail below. Figure 7.1 (b) also shows that the extra branches that develop in Fig. 7.1 (a) at $\kappa\tau \geq 0.1347$ are not bifurcations. They are due to the symmetric limit cycle spiralling through, and thus producing extra crossings with, its value of average intensity.

7.2 Unstable manifolds

Figures 7.2 and 7.3 show the phase portraits corresponding to Fig. 7.1 in projection onto (E,N)-space [Fig. 7.2] and the E-plane [Fig. 7.3]. Except for panels (a) and (b), which were obtained by simulation, these phase portraits were obtained by plotting both branches of the 1D unstable manifold of one of the two symmetric saddle points, marked by $\times$; the corresponding attracting steady states are marked by $+$. The bifurcation diagrams in Fig. 7.1, along with Figs. 7.2 and 7.3, present a complete picture of the route into and out of locking for the PCF laser specified in Section 4.1.

For very low values of $\kappa\tau$, system (4.1) has an almost planar periodic solution surrounding the origin of the E-plane [Figs. 7.2 (a), 7.3 (a)], which is the continuation of the free-running laser ($\kappa\tau = 0$) that has constant power and inversion. With increasing feedback the laser is destabilised. First, the periodic solution starts to curl up near two distinct points [Figs. 7.2 (b), 7.3 (b)]. It develops a typical shape and does end in a saddle-focus heteroclinic bifurcation *SFH* when it hits two saddle-focus steady states at $\kappa\tau \approx 0.2953$, [Fig. 7.1 (b)]. The exact nature of this global bifurcation is detailed in Section 7.3.1. The two saddle-focus steady states are each others symmetric counterparts and are born together with two attractors in the saddle-node bifurcation *SN* at

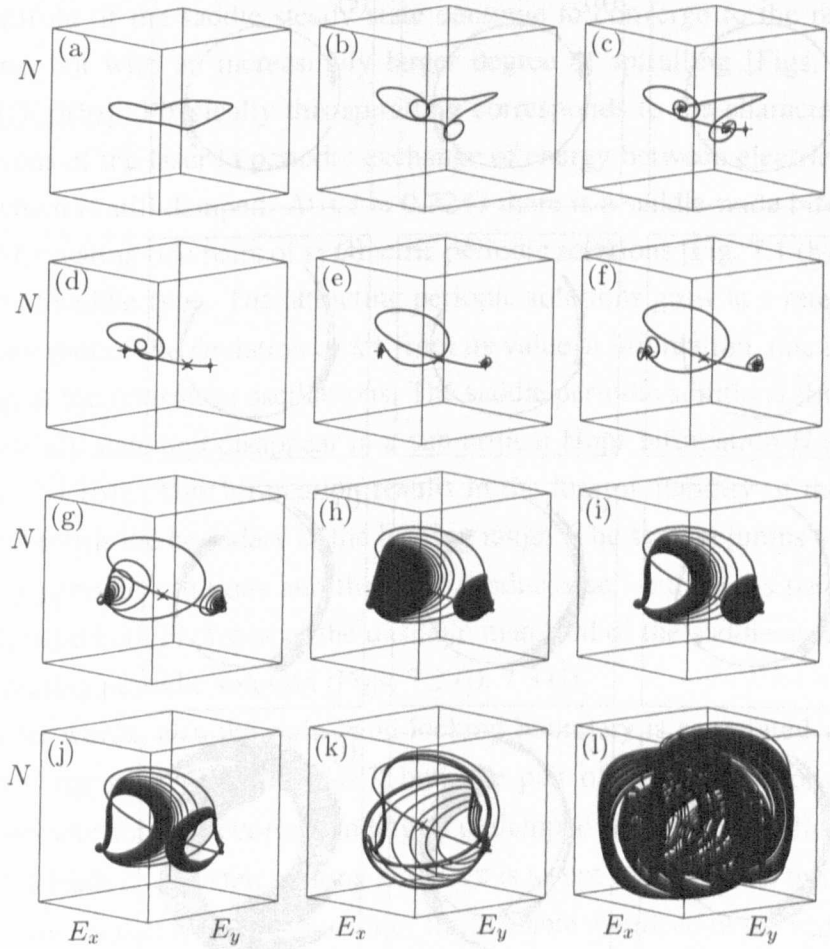

Figure 7.2: Phase portraits shown in projection onto (E,N)-space. Except for (a) and (b), plotted are both branches of the 1D unstable manifold of one of the two symmetric saddle points ($\times$). The box is $[-200, 200] \times [-200, 200] \times [7.61 \times 10^8, 7.68 \times 10^8]$; from (a) to (l), $\kappa\tau$ takes the values 0.1000, 0.2700, 0.2952, 0.3065, 0.4410, 0.5180, 0.6182, 0.7183, 0.7252, 0.7253, 0.7904, and 0.9004.

$\kappa\tau \approx 0.2794$, that is, before the saddle-focus heteroclinic bifurcation [Fig. 7.1 (b)]. This produces a region of bistability between the pair of attracting steady states and the periodic solution. Indeed, for $\kappa\tau \in [0.2794, 0.2953]$ one branch of the 1D unstable manifold converges to the periodic solution, while the other branch converges to a locked steady state [Figs. 7.2 (c), 7.3 (c)]. Physically this bistability means that the laser is capable of producing locked or periodic output for the same experimental value of $\kappa\tau$, depending on the initial condition. After the saddle-focus heteroclinic bifurcation, bistability is lost and both branches of the saddle-focus steady state converge to one of the

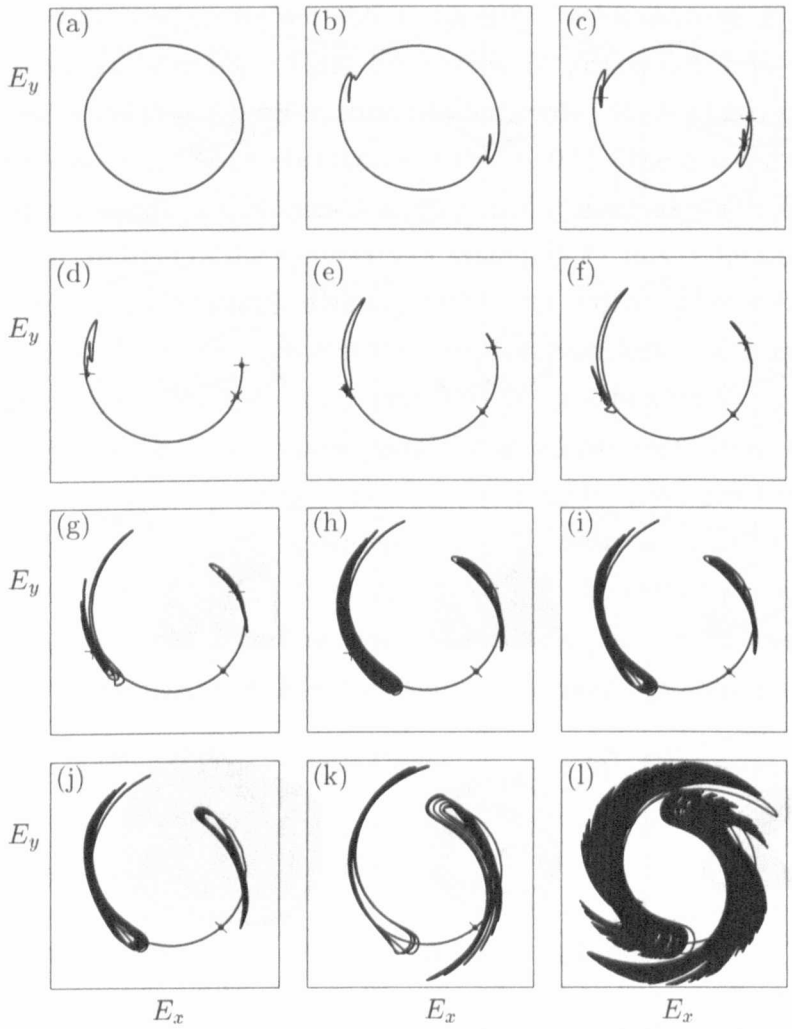

Figure 7.3: Projection of plots in Fig. 7.2 onto the E-plane; the square is $[-270, 270] \times [-270, 270]$.

two locked solutions, which are the only attractors and symmetric images of each other [Figs. 7.2 (d), 7.3 (d)].

This bistability leads to a hysteresis loop: for increasing $\kappa\tau$ the symmetric periodic solution is destroyed in the saddle-focus heteroclinic bifurcation *SFH* and the system jumps to one of the steady states, whereas for decreasing $\kappa\tau$ the two steady states are destroyed in the saddle-node bifurcation *SN* and the system jumps to the symmetric periodic solution. So not only do we see a qualitative change in the attracting solutions, but we also see a change in the symmetry of the attractor, as is indicated in Fig. 7.1.

As $\kappa\tau$ is increased further through the locking region, the two branches of the

1D manifold of the saddle steady state continue to converge to the respective locked solutions, but with an increasingly larger degree of spiralling [Figs. 7.2 (e)(f)(g)(h), 7.3 (e)(f)(g)(h)]. Physically this spiralling corresponds to the characteristic relaxation oscillations of the laser (a periodic exchange of energy between electric field and inversion), which is still damped. At $\kappa\tau \approx 0.7247$ there is a saddle-node bifurcation of limit cycles *SL* creating two pairs of symmetric periodic solutions [Fig. 7.1 (b)], one attracting and one of saddle-type. The attracting periodic solutions grow at a rate proportional to the square root of the deviation of $\kappa\tau$ from its value at bifurcation, one speaks of an undamping of the relaxation oscillations. The saddle periodic solutions shrink down to the locked steady state and disappear in a sub-critical Hopf bifurcation *H* at $\kappa\tau \approx 0.7487$; see [Fig. 7.1 (b)]. This bifurcation results in the loss of stability of the locked steady states and forms the boundary of the locking range. The system jumps to one of the two attracting periodic solutions and the laser produces self-pulsations (relaxation oscillations). Indeed both branches of the unstable manifold of the saddle steady state end up at an attracting periodic solution [Figs. 7.2 (j), 7.3 (j)].

In other words, also the right-hand locking boundary is associated with a region of bistability: for $\kappa\tau \in [0.7247, 0.7487]$ both the pair of locked solutions as well as the pair of periodic solutions corresponding to undamped relaxation oscillations are stable. Again, this leads to a hysteresis loop when $\kappa\tau$ is swept up and down through *SL* and *H*.

Note already that the two branches of the unstable manifold of the saddle steady state behave differently just after *SL* [Figs. 7.2 (i), 7.3 (i)] and just before *H* [Figs. 7.2 (j), 7.3 (j)]. As will be discussed in detail in Section 7.3.2, this implies the existence of a heteroclinic bifurcation between *SL* and *H*.

When $\kappa\tau$ is increased further, the pair of stable periodic solutions undergoes a period-doubling cascade starting at $\kappa\tau \approx 0.8393$ [Fig. 7.1 (b)]. This eventually leads to both branches of the 1D unstable manifold of the saddle steady state accumulating on a chaotic attractor [Figs. 7.2 (l), 7.3 (l)]. For even larger values of $\kappa\tau$ the two attractors collide in an attractor crisis caused by a collision of their basins of attraction, culminating in symmetry restoring inside the chaotic region [35].

7.3 Global bifurcations

We already mentioned in the last section that at both boundaries of the locking range we find global bifurcations, namely a saddle-focus heteroclinic bifurcation between two saddle steady states at the left-hand boundary, and a heteroclinic bifurcation between a

saddle steady state and a saddle periodic solution at the right-hand boundary. We now discuss these two global bifurcations in detail.

7.3.1 Heteroclinic connection between two steady states

In Fig. 7.4 (a) we show the symmetric limit cycle just before the saddle-focus heteroclinic bifurcation *SFH* in which it hits the pair of saddle-focus steady states x_1 and x_2. A time-trace of E_y over its period $\mathrm{T} \approx 41.0\tau$ is shown in Fig. 7.4 (c), where the mesh points used in the DDE-BIFTOOL continuation are highlighted. When approaching *SFH* the period T goes to infinity. At *SFH* the periodic solution disappears and instead we have a symmetric pair of heteroclinic connections between x_1 and x_2, one of which is shown in Fig. 7.4 (b). This connecting orbit was computed with the new extension of DDE-BIFTOOL introduced in Ref. [55]. Its time-trace with highlighted mesh points is shown in Fig. 7.4 (d). An analysis of the eigenvalues of the saddle-foci shows a negative saddle quantity, $\sigma = \lambda_1 + Re(\lambda_{2,3})$, where $\lambda_1 > 0$, while $\lambda_{2,3}$ are the complex pair of eigenvalues with negative real part that are closest to the imaginary axis. This implies that there is a unique bifurcating stable limit cycle [43].

The fact that this global bifurcation appears as two simultaneous heteroclinic connections is due to the symmetry of Eqs. (4.1). When one divides out the symmetry and identifies x_1 and x_2 then one gets just a regular saddle-focus homoclinic connection.

We remark that after but near the saddle-focus heteroclinic bifurcation *SFH* the system is excitable – an example of excitability due to a heteroclinic bifurcation [10]. When the locked solution is perturbed to the other-side of the saddle steady state it will produce a large excursion by following roughly the old heteroclinic connection and ending up at the other locked solution [Fig. 7.2 (d), 7.3 (d)]. Physically, this corresponds to a phase jump by π and a relaxing pulse in the power of the laser. We remark that the amplitude of this pulse is quite small. This can also be inferred from Fig. 7.3 (d): the distance from the origin in the E-plane does not change much and the power is the square of this distance.

7.3.2 Heteroclinic connection between a steady state and a periodic orbit

Between the saddle-node bifurcation *SL* and the Hopf bifurcation *H* we have another region of bistability where again the laser can produce qualitatively different stable output

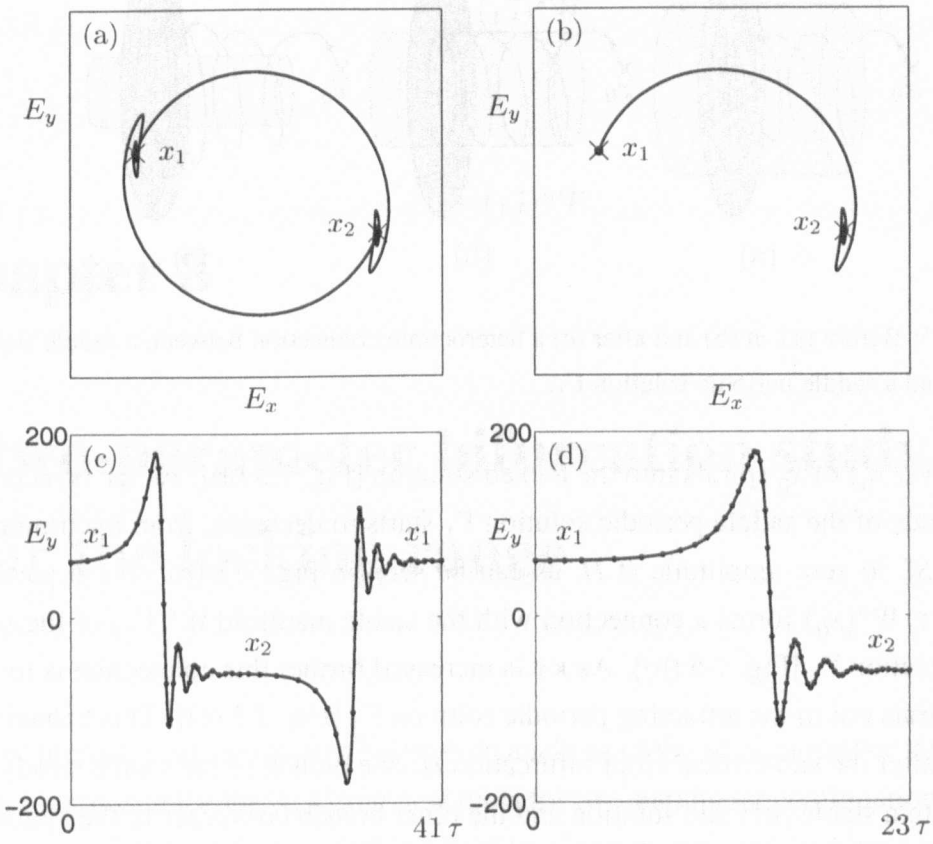

Figure 7.4: The periodic solution just before the saddle-focus heteroclinic bifurcation (a) and the heteroclinic connection between the saddle steady states x_1 and x_2 at the bifurcation (b). Panels (c) and (d) show the corresponding time-traces of E_y with the mesh points highlighted.

depending on the initial condition. The infinite-dimensional stable manifold of the unstable periodic solution forms the boundary between solutions converging to the locked steady state or the stable periodic solution.

As the unstable periodic solution decreases in size there must be a heteroclinic connection between the saddle periodic solution and a saddle steady state, we now explain this in detail. Figures 7.2 (i), 7.3 (i) show the 1D unstable manifolds for $\kappa\tau = 0.7252$, which is typical of the region $\kappa\tau \in [0.7247, 0.7252]$ where we see one branch spiralling into a periodic solution, while the other branch spirals to a locked solution. However, at $\kappa\tau = 0.7253$ [Figs. 7.2 (j), 7.3 (j)], one branch spirals into a periodic solution as before, but the other branch now spirals out to the symmetric counterpart of this periodic solution. This implies that between the values of $\kappa\tau = 0.7252$ and $\kappa\tau = 0.7253$ a heteroclinic bifurcation must take place, as is sketched in Fig. 7.5. Initially, the 1D unstable

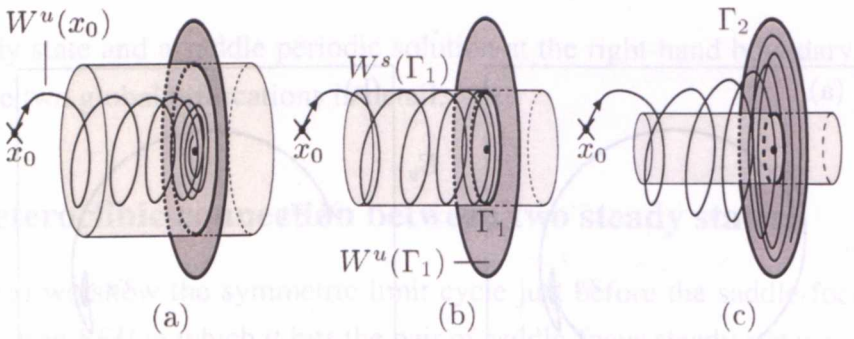

Figure 7.5: Before (a), at (b) and after (c) a heteroclinic connection between a saddle steady state x_0 and a saddle periodic solution Γ_1.

manifold $W^u(x_0)$ of x_0 spirals into the locked solution [Fig. 7.5 (a)]. As $\kappa\tau$ is increased, the amplitude of the saddle periodic solution Γ_1 starts to decrease, from maximum amplitude at *SL* to zero amplitude at *H*, as can be seen in Fig. 7.1 (b). For a particular value of $\kappa\tau$, $W^u(x_0)$ forms a connection with the stable manifold $W^s(\Gamma_1)$ of the saddle periodic solution Γ_1 [Fig. 7.5 (b)]. As $\kappa\tau$ is increased further this connection is lost and $W^u(x_0)$ spirals out to the attracting periodic solution Γ_2 [Fig. 7.5 (c)]. This behaviour is preserved after the sub-critical Hopf bifurcation *H*: one branch of the saddle steady state converges to a stable periodic solution and the other branch converges to the symmetric counterpart of this periodic solution [Figs. 7.2 (k), 7.3 (k)].

7.4 Conclusions

We studied in detail the transitions into and out of locking of a semiconductor laser with phase-conjugate feedback. Both feature bistabilities leading to hysteresis loops. Furthermore, both transitions to locking are associated with global bifurcations, namely a saddle-focus heteroclinic bifurcation and heteroclinic bifurcation between a steady state and a periodic solution, respectively. New tools for DDEs allowed us to study these global bifurcations in unprecedented detail.

The bifurcation scenario we described is structurally stable. Initial investigations of some bifurcation curves in the plane of $\kappa\tau$ versus injection current indicate that this scenario appears to be typical for a PCF laser pumped near its threshold current (up to about 7.7% above threshold), which is the region of injection current most commonly investigated in feedback experiments.

The construction of a full two-dimensional bifurcation diagram is the next logical step and is the topic of Chapter 8.

Chapter 8

A two-parameter bifurcation study near the locking range

We now present a two-parameter bifurcation analysis of the semiconductor laser subject to phase-conjugate feedback. Using new tools for two-parameter continuation in DDEs, we present a full two-dimensional bifurcation diagram near the locking range of the PCF laser in the plane of feedback strength versus pump current. We are able to follow bifurcations of equilibria and connecting orbits in two-parameters. On the other hand, bifurcations of periodic orbits can be detected, but two-parameter continuation of such bifurcations is not yet available. We identify codimension-two bifurcations, including a double-Hopf point, a Belyakov point and a bifurcation of heteroclinic orbits known as a T-point, and show how the dynamics of the PCF laser near the locking region are organised around these points.

What is presented here is a first example of a two-parameter continuation study of a system of DDEs. In fact, DDE-BIFTOOL was extended to cope with specific issues raised by this study, for example, the computation of a neutral-saddle curve and questions raised during the continuation of connecting orbits.

We also make a first attempt at mapping out bifurcations of periodic orbits in the system by detecting individual bifurcation points at appropriate values of the parameters. This reveals a number of interesting bifurcation scenarios, including a cusp bifurcation, and possible Bogdanov-Takens and 1:2 resonance points which we hope, with the development of new tools, will be studied in the future.

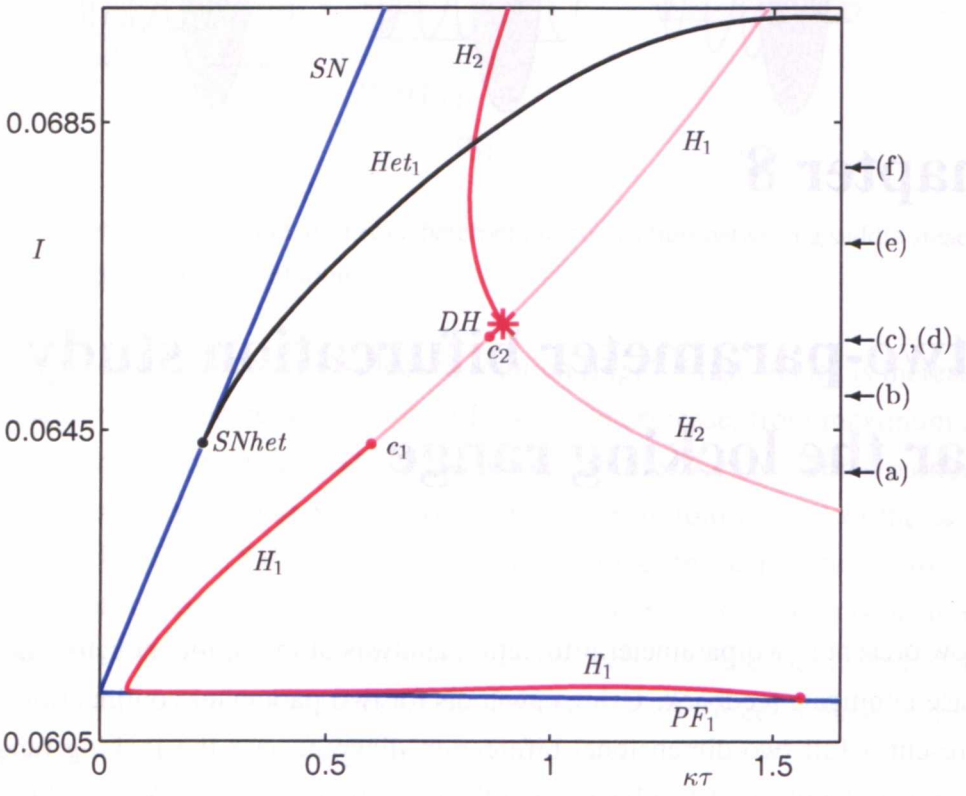

Figure 8.1: Bifurcations bounding the locking range of the PCF laser in $(\kappa\tau, I)$-space. The arrows correspond to the one-parameter continuations shown in Figure 8.2.

8.1 The locking range

In this section we use the continuation package DDE-BIFTOOL to detect and follow the bifurcations involved in the locking mechanism of the PCF laser. The resulting bifurcation diagram shown in Fig. 8.1 was obtained by starting a two-parameter continuation from bifurcation points identified in one-parameter studies, including the study described in Chapter 7. Plotted in red are curves of Hopf bifurcations $H_{1,2}$ where each point on the curve represents a steady state with a pair of pure imaginary eigenvalues. The Hopf curves $H_{1,2}$ are drawn dark when they are supercritical (the bifurcating periodic orbit is stable), and are drawn in a lighter tone when they are subcritical (the bifurcating periodic orbit is unstable). In blue are plotted curves of saddle-node bifurcations *SN* and pitch-fork bifurcations PF_1, in both cases each point represents a steady state with a real

eigenvalue equal to zero. Furthermore, we plot a curve of heteroclinic connections Het_1 between two saddle steady states that are each others symmetric counterparts.

The general picture of the locking range of the PCF laser is that it is bounded by the curve of saddle-node bifurcations *SN* to the left, the (supercritical parts of the) curves of Hopf bifurcations $H_{1,2}$ to the right and a curve of pitchfork bifurcations PF_1 below. Passing through the locking range is a curve of heteroclinic orbits Het_1. The area above the curve Het_1, and between the curves *SN* and H_2 is a region of bistability, that is, the periodic orbit involved in the heteroclinic bifurcation Het_1 and the non-symmetric steady states born in the saddle-node bifurcation *SN* coexist; see already Figs. 8.2 (b) to (f). Note that, when the heteroclinic curve crosses the curve of Hopf bifurcations H_2 there is a second region of bistability, where two stable periodic solutions coexist.

The non-symmetric saddle steady states are born in the saddle-node bifurcation *SN* together with a pair of non-symmetric stable steady states which correspond to the locked solutions of the PCF laser. These locked solutions are destabilised along the curves of Hopf bifurcations $H_{1,2}$ when they bifurcate with a periodic orbit. Between c_1 and c_2, on H_1, the Hopf bifurcation is subcritical, that is, the bifurcating periodic orbit is unstable. As was shown in Chapter 7, for fixed I, this subcritical Hopf bifurcation leads to a bistability between an attracting steady state and an attracting periodic orbit, and a heteroclinic connection between their respective saddles [27]. This bistability is due to a saddle-node bifurcation of limit cycles *SL* curve connecting c_1 and c_2, and running parallel to the subcritical part of H_1; see already Fig. 8.8 (b).

The pitchfork curve PF_1 is a bifurcation of the trivial steady state. Below PF_1, the trivial steady state is stable. It is destabilised at PF_1 when it bifurcates with a pair of non-symmetric stable steady states (the locked solutions). Physically, the PCF laser is in its off-state below PF_1. In this system with $\mathbb{Z}_2$-symmetry the pitchfork bifurcation constitutes the laser threshold, that is, it marks the onset of lasing.

The Hopf curves $H_{1,2}$ intersect at the point *DH*, at $(\kappa\tau, I) \approx (0.893, 0.06589)$, which is a codimension-two double-Hopf bifurcation point where there are two pairs of complex eigenvalues on the imaginary axis [43]. At this bifurcation point the center manifold is four-dimensional, in other words, this bifurcation is only possible in a phase-space of dimension greater than or equal to four. Around a double-Hopf point the system can bifurcate to a number of invariant objects, including two-dimensional tori which may branch to three-dimensional tori [43]. In fact, we will see below that, near the double-Hopf point, a period-doubling route to chaos [27] becomes a route to chaos via the break-up of a torus.

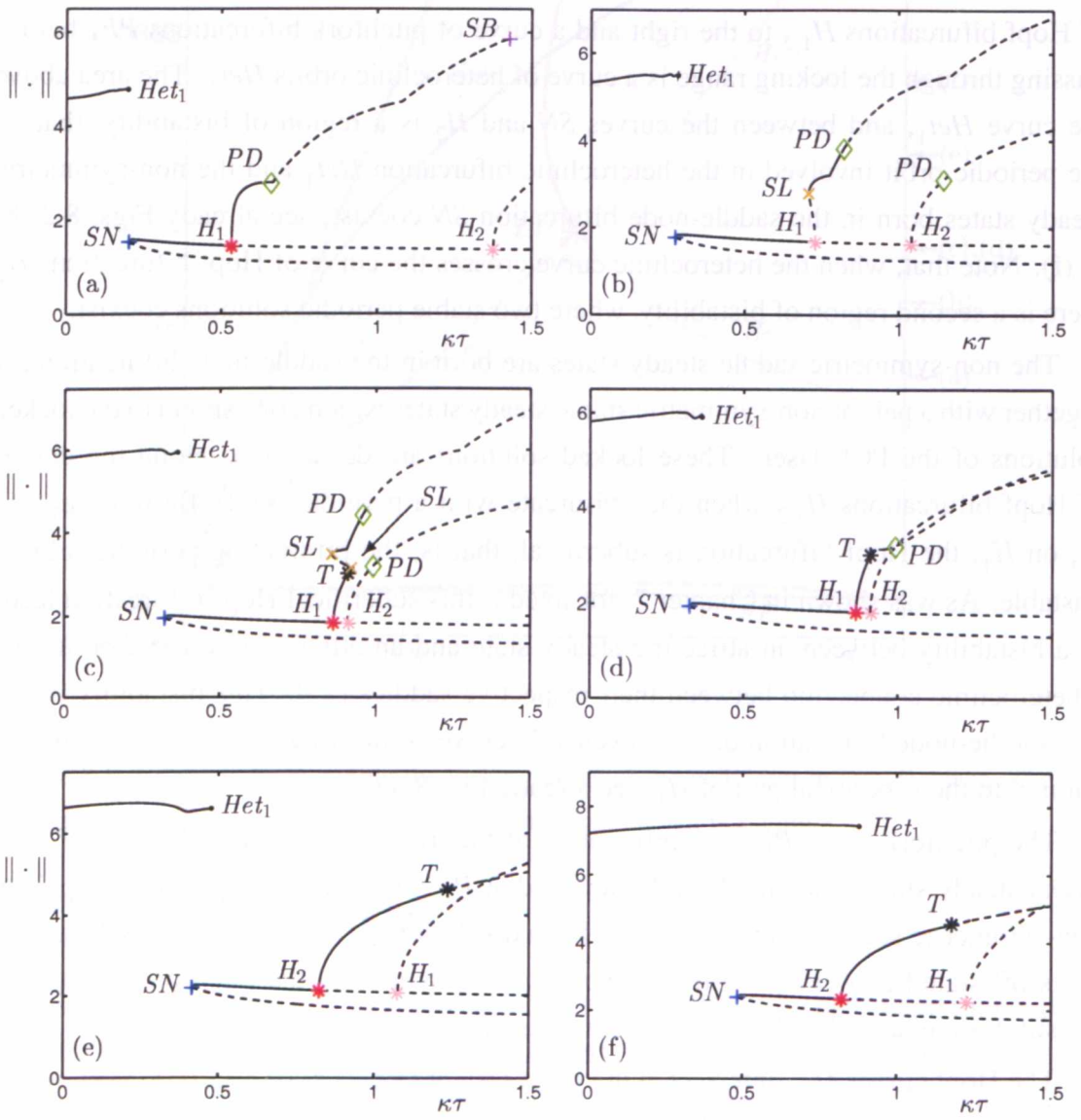

Figure 8.2: One parameter continuation of equilibria and periodic orbits for fixed pump current I; from (a) to (f) I takes the values 0.064, 0.065, 0.0657345, 0.0657347, 0.067, and 0.068.

At $(\kappa\tau, I) \approx (0.225, 0.06433)$ the heteroclinic curve Het_1 ends at the saddle-node curve *SN* at a saddle-node heteroclinic point *SNhet*. Here the saddle-node bifurcation takes place on a codimension-one heteroclinic connection. If we divide out the symmetry of system (4.1), this is a saddle-node homoclinic bifurcation [43]. Below the point *SNhet* the saddle-node bifurcation *SN* takes place on a limit cycle [29].

The lower part of the Hopf curve H_1 is seen to bend off and run roughly parallel to the curve PF_1 before terminating. For low values of fixed pump current I, this means that it is possible for the laser to lock and unlock as the value of $\kappa\tau$ is varied; see already Fig. 8.4. However, this effect occurs for a very small range of I and would be extremely difficult to observe experimentally.

We now discuss transitions through the two-dimensional bifurcation diagram in Fig. 8.1 as we vary the value of $\kappa\tau$ for fixed values of I, this is the approach we took in Chapter 7. The bifurcation diagrams in Fig. 8.2 were obtained with DDE-BIFTOOL and the respective I-values are indicated by the arrows on the right of Fig. 8.1. For steady states we plot $Re(E)$ and for periodic solutions we plot $|\max(Re(E)) - \min(Re(E))|$, offset by the $Re(E)$-value of the steady state at the Hopf point. Attracting solutions are drawn as solid curves, while unstable solutions are drawn as dashed curves. By studying the eigenvalues of the system we are able to identify the bifurcations involved. Apart from saddle-node bifurcation *SN*, Hopf bifurcations $H_{1,2}$ and saddle-focus heteroclinic bifurcations Het_1 already shown in Fig. 8.1, we also find saddle-node bifurcations of limit cycles *SL*, period-doubling bifurcations *PD*, symmetry-breaking (or restoring) bifurcations *SB* and torus (or Neimark-Sacker) bifurcations *T*. The different bifurcations are colour coded throughout; compare Fig. 8.1, and see already Figs. 8.3, 8.4 and 8.8.

For low values of I [Fig. 8.2 (a)], the saddle-node bifurcation *SN* occurs very close to the saddle-focus heteroclinic bifurcation Het_1. For $I < 0.06433$, the steady state is destabilised in the supercritical Hopf bifurcation H_1. The ensuing periodic solution then undergoes a period-doubling bifurcation *PD*, the first along a route to chaos; compare Fig. 7.1. At $I \approx 0.06433$ the Hopf bifurcation H_1 becomes subcritical, for larger values of I [Fig. 8.2 (b)] we observe the emergence of a saddle-node bifurcation of limit cycles *SL*. This is the scenario considered in Chapter 7 and Ref. [27]; again see Fig. 7.1. At $I \approx 0.0657345$, the period-doubling route to chaos is preceded by a torus bifurcation *T* and two saddle-node bifurcations of limit cycles *SL*. Consequently, we find a bistability between two stable periodic solutions [Fig. 8.2 (c)]. One of the periodic solutions is born in the Hopf bifurcation H_1 at $\kappa\tau \approx 0.8653$ and is destabilised in the torus bifurcation *T* at

$\kappa\tau \approx 0.9118$. The other periodic solution is born in the saddle-node bifurcation of limit cycles SL at $\kappa\tau \approx 0.8598$, first identified in Fig. 8.2 (b), and is destabilised in the period-doubling bifurcation PD at $\kappa\tau \approx 0.9593$. For $I > 0.0657346$ the route to chaos via the break-up of a torus persists [Fig. 8.2 (d)]. This change, from a period-doubling route to chaos to a route to chaos via the break-up of a torus, appears to be due to the presence of the double-Hopf point. At the double-Hopf point the Hopf curves H_1 and H_2 pass through one another. Figure 8.2 (e) shows the situation for $I = 0.067$. The first Hopf bifurcation that destabilises the non-symmetric saddle steady state is now H_2, which leads to a stable periodic orbit that is destabilised in a torus bifurcation T at $\kappa\tau \approx 1.236$. As I is increased further there is an increasingly larger region of bistability between a stable periodic solution and the non-symmetric stable steady state at the left boundary of the region of stability. This is a result of the heteroclinic curve Het_1 moving away from the saddle-node bifurcation curve SN, and crossing into the locking range. Finally, for $I > 0.068222$ the periodic orbit involved in the heteroclinic bifurcation exists past the first Hopf bifurcation. This is shown in Fig. 8.2 (f) where for $I = 0.068$ we observe a bistability between the periodic orbit involved in the heteroclinic bifurcation and the periodic orbit born in the Hopf bifurcation H_2.

8.2 Bifurcations of steady states

In Fig. 8.3 we increase the area of $(\kappa\tau, I)$-space under consideration to take a somewhat more global point of view. We follow the curves of saddle-node bifurcations SN, pitchfork bifurcations PF_1, Hopf bifurcations $H_{1,2}$ and heteroclinic bifurcations Het_1 shown in Fig. 8.1 further. We also follow the additional curves of pitchfork bifurcations PF_2, Hopf bifurcations H_3 and heteroclinic bifurcations Het_2, and show a neutral saddle curve ns. This provides a consistent picture of the bifurcations that can be continued, namely, bifurcations of steady states and heteroclinic orbits.

Figure 8.4 shows an enlargement of Fig. 8.3 near the laser threshold, illustrating the interaction of the pitchfork curves $PF_{1,2}$ with the Hopf curves $H_{1,3}$. The steady states in three different regions are sketched, where stable steady states are drawn as blue points and saddle (unstable) steady states are drawn as red points. As was mentioned earlier, below the pitchfork curve PF_1 the trivial steady state is stable [region 1]. Physically, the curve PF_1 marks the onset of lasing of the PCF laser (below this curve the laser is off). At the curve PF_1, the trivial steady state is destabilised and a pair of non-symmetric stable steady states emerge [region 2], these are destabilised at the Hopf curve H_1. The curve

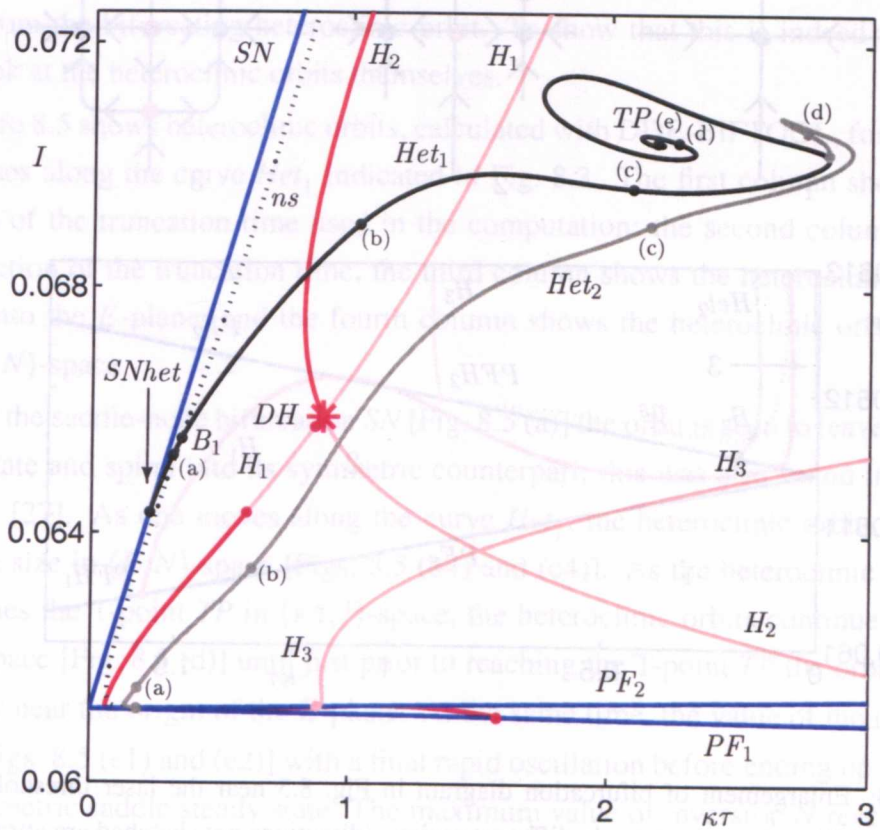

Figure 8.3: Bifurcations of steady states in $(\kappa\tau, I)$-space. The labels along the curves $Het_{1,2}$ correspond to phase portraits shown in Figs. 8.5 and 8.7.

of pitchfork bifurcations PF_2 represents another bifurcation of the trivial steady state. At this curve the trivial steady state has a zero eigenvalue, which means that a pair of non-symmetric saddle steady states is born [region 3]. These saddles are those involved in the saddle-node bifurcation SN and they appear as the lower branch of saddle steady states identified in Fig. 8.2. At the Hopf curve H_3 this non-symmetric saddle steady state undergoes a Hopf bifurcation, where it bifurcates with a saddle periodic orbit. The codimension-two pitchfork-Hopf bifurcation points $PFH_{1,2}$ represent the ends of the Hopf curves $H_{1,3}$, respectively. At a pitchfork-Hopf point the center manifold is three-dimensional, and one finds a real eigenvalue and two pure imaginary eigenvalues on the imaginary axis [43].

The shape of the Hopf curve H_1 means that the laser can lock and unlock for a fixed value of the pump current I as the feedback strength $\kappa\tau$ is varied. For example, for

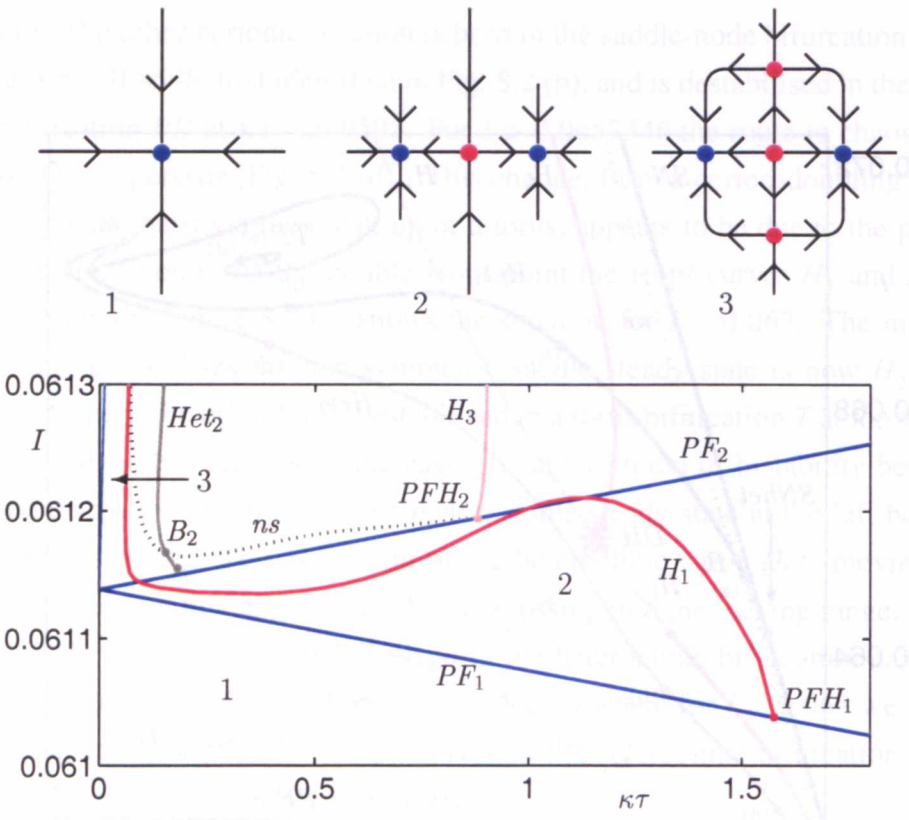

Figure 8.4: Enlargement of bifurcation diagram in Fig. 8.3 near the laser threshold, and sketch of stability of steady states in different regions (directions not sketched are attracting).

$I = 0.0612$ a locked solution is born in a saddle-node bifurcation SN at $\kappa\tau \approx 0.00428$. This solution is unlocked (becomes unstable) at the Hopf curve H_1 at $\kappa\tau \approx 0.0606$ and the ensuing solution is once again locked at the Hopf curve H_1 at $\kappa\tau \approx 0.977$. A final intersection with the Hopf curve H_1 at $\kappa\tau \approx 1.227$ results in an unlocked solution. However, we note that this would be extremely difficult to observe experimentally due to the small ranges in the parameters involved.

The curves of heteroclinic bifurcations $Het_{1,2}$ are explained in the next section. We already note that, as is to be expected, they end at the curves SN and PF_2 where the non-symmetric saddle steady states involved in the heteroclinic orbits are born.

8.3 Global bifurcations

Figure 8.3 shows that the curve of heteroclinic bifurcations Het_1 curls up near the point marked TP. This indicates that the centre point of the spiral is a codimension-two point

known as a *T-point* [20]. At *TP* the heteroclinic connection between the two non-symmetric steady states is destroyed. This results in the creation of two heteroclinic orbits from the bifurcating heteroclinic orbit. To show that this is indeed the case we must look at the heteroclinic orbits themselves.

Figure 8.5 shows heteroclinic orbits, calculated with DDE-BIFTOOL, for the parameter values along the curve Het_1 indicated in Fig. 8.3. The first column shows E_x as a function of the truncation time used in the computation; the second column shows N as a function of the truncation time; the third column shows the heteroclinic orbit projected onto the E-plane; and the fourth column shows the heteroclinic orbit projected onto (E,N)-space.

Near the saddle-node bifurcation *SN* [Fig. 8.5 (a)] the orbit is seen to leave one saddle steady state and spiral into its symmetric counterpart; this was also found in Chapter 7 and Ref. [27]. As one moves along the curve Het_1, the heteroclinic orbits start to increase in size in (E,N)-space [Figs. 8.5 (b4) and (c4)]. As the heteroclinic curve Het_1 approaches the T-point *TP* in $(\kappa\tau,I)$-space, the heteroclinic orbits continue to grow in (E,N)-space [Fig. 8.5 (d)] until just prior to reaching the T-point *TP* the orbit is seen to pass very near the origin of the E-plane. At the same time, the value of the inversion N grows [Figs. 8.5 (e1) and (e2)] with a final rapid oscillation before ending up at the other non-symmetric saddle steady state. The maximum value of inversion N reached is very close to the value of N of the trivial steady state [Fig. 8.5 (e4)]. This is a clear indication that we are very near the forthcoming T-point bifurcation.

One can find the new heteroclinic orbits constituting the heteroclinic orbits at the T-point *TP*, that is, connecting the trivial steady state to the non-symmetric steady states, by providing the boundary value solver DDE-BIFTOOL with the position and stability information of the trivial steady state. As is to be expected at a T-point there is a codimension-two connection from the non-symmetric steady state to the trivial steady state and a codimension-zero connection from the trivial steady state to the symmetric counterpart of the non-symmetric steady state.

Figure 8.6 (a) shows the heteroclinic orbit between the two non-symmetric steady states. The codimension of a heteroclinic orbit is given by the sum of the dimension of the unstable manifold of the end steady state minus the dimension of the unstable manifold of the initial steady state plus one [55]. The non-symmetric steady states have one-dimensional unstable manifolds. Consequently, the heteroclinic orbit (and its symmetric counterpart) shown Fig. 8.6 (a) is of codimension-one. This orbit is seen to start at one of the non-symmetric steady states and then spend much time at the trivial steady

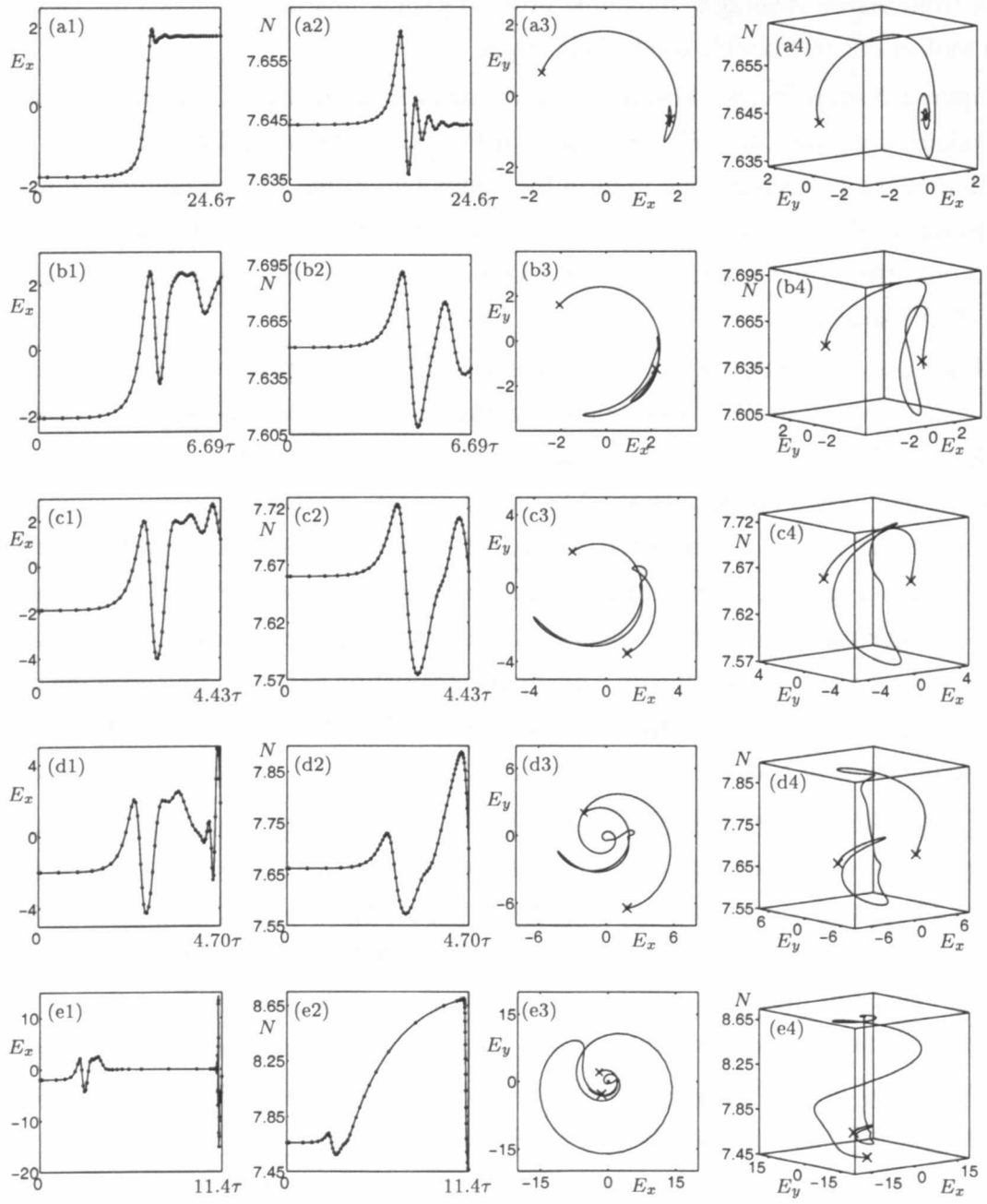

Figure 8.5: Heteroclinic orbits along the curve Het_1; from (a) to (e) $(\kappa\tau, I)$ takes the values $(0.314, 0.065264)$, $(1.303, 0.069026)$, $(2.085, 0.069635)$, $(2.201, 0.070357)$, and $(2.177, 0.070394)$.

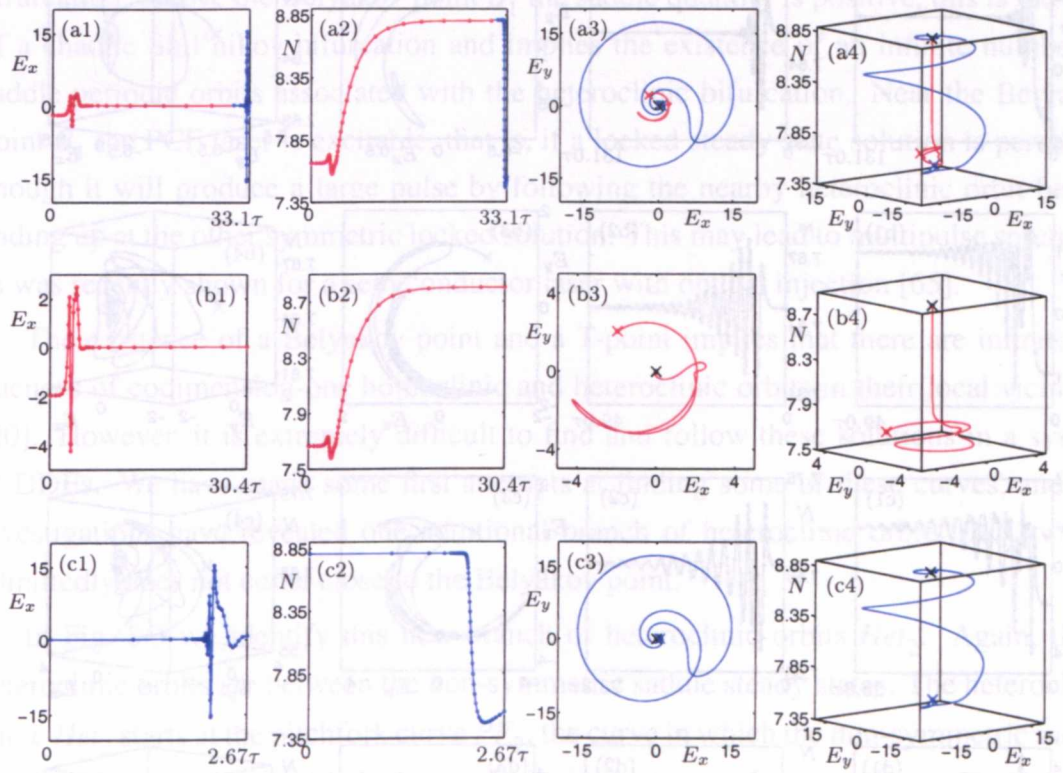

Figure 8.6: Codimension-one heteroclinic orbit very close to the T-point *TP* (a), and the corresponding codimension-two (b) and codimension-zero (c) heteroclinic orbits at the T-point *TP*.

state (red part of the orbit) before a sudden oscillation back to the end non-symmetric steady state (blue part of the orbit). These two parts correspond to the two heteroclinic orbits that we find at the T-point. The first of these is shown in Fig. 8.6 (b). The non-symmetric steady states have one-dimensional unstable manifolds and the trivial steady state has a two-dimensional unstable manifold, therefore, the heteroclinic orbit shown in Fig. 8.6 (b) is of codimension-two. This heteroclinic connection only exists at the point *TP*, and its continuation would require freeing a third parameter, which is beyond the scope of this study. The second heteroclinic orbit found at the T-point *TP* is shown in Fig. 8.6 (c). Because the trivial steady state has a two-dimensional unstable manifold and the non-symmetric steady states have one-dimensional unstable manifolds, this heteroclinic orbit is of codimension-zero. In other words, this heteroclinic orbit exists for all values of $(\kappa\tau, I)$ in a local neighbourhood of the T-point *TP*.

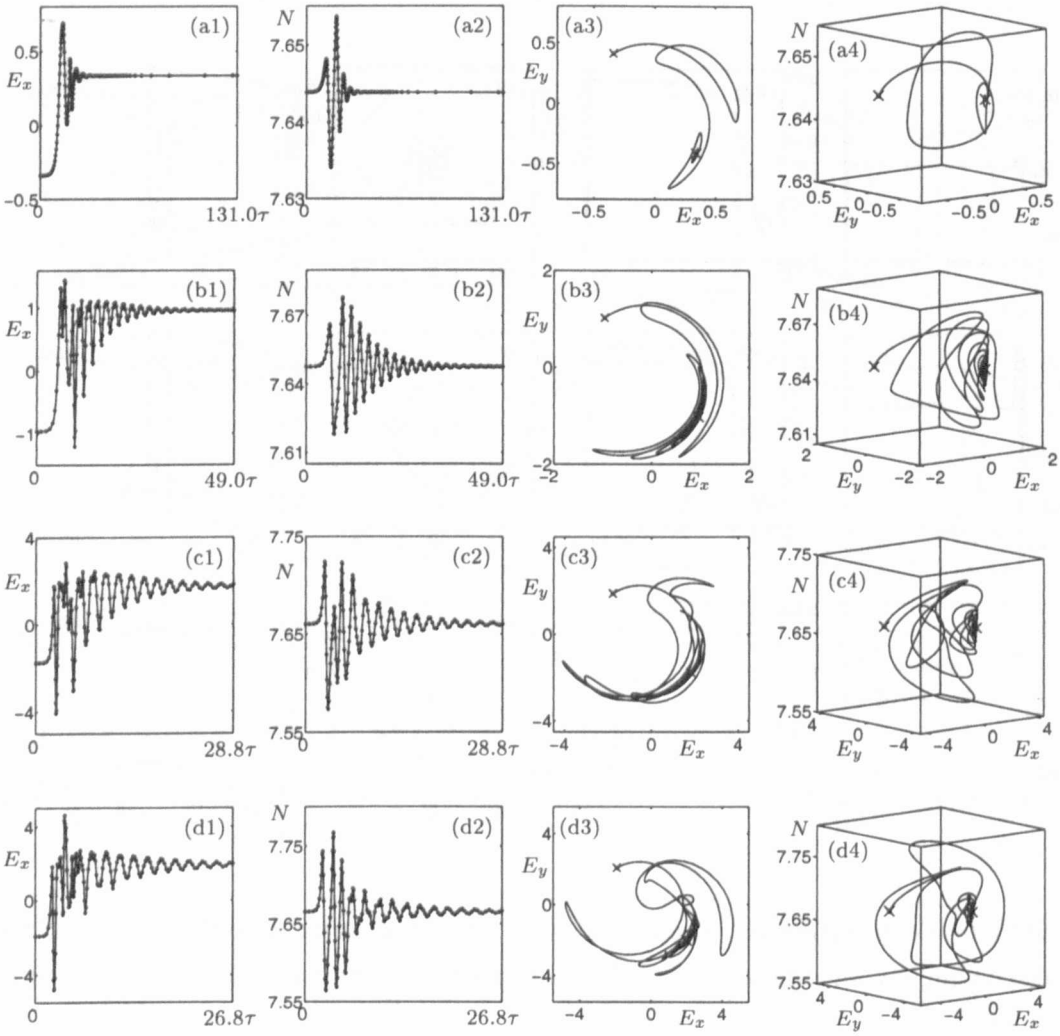

Figure 8.7: Heteroclinic orbits along the curve Het_2; from (a) to (d) $(\kappa\tau, I)$ takes the values $(0.182, 0.061478)$, $(0.620, 0.063430)$, $(2.153, 0.069019)$, and $(2.751, 0.070576)$.

In Figs. 8.3 and 8.4, the dotted curve *ns* represents a neutral saddle curve, along which the saddle steady states born in the saddle-node bifurcation *SN* have zero saddle quantity, that is, $\sigma = \lambda_1 + Re(\lambda_{2,3}) \equiv 0$, $\lambda_1 < 0$, $Re(\lambda_{2,3}) > 0$. We note that the curve *ns* starts at the pitchfork curve PF_2, the curve in which the non-symmetric saddle steady states associated with the neutral saddle are born; see Fig. 8.4. The curve is seen to intersect the curve of heteroclinic orbits Het_1 at the point B_1, a codimension-two Belyakov point [65]. Along the curve Het_1, the heteroclinic orbits between the saddle-node heteroclinic bifurcation *SNhet* and the Belyakov bifurcation B_1 have a negative saddle quantity

corresponding to a bifurcating attracting periodic orbit associated with the heteroclinic bifurcation. Above the Belyakov point B_1 the saddle quantity is positive, this is the case of a chaotic Shil'nikov bifurcation and implies the existence of an infinite number of saddle periodic orbits associated with the heteroclinic bifurcation. Near the Belyakov point B_1 the PCF laser is excitable, that is, if a locked steady state solution is perturbed enough it will produce a large pulse by following the nearby heteroclinic orbit before ending up at the other symmetric locked solution. This may lead to multipulse solutions, as was recently shown for a semiconductor laser with optical injection [65].

The existence of a Belyakov point and a T-point implies that there are infinite sequences of codimension-one homoclinic and heteroclinic orbits in their local vicinities [20]. However, it is extremely difficult to find and follow these solutions in a system of DDEs. We have made some first attempts at finding some of these curves, and our investigations have revealed one additional branch of heteroclinic orbits Het_2, which admittedly does not come close to the Belyakov point.

In Fig. 8.3 we identify this new branch of heteroclinic orbits Het_2. Again, these heteroclinic orbits are between the non-symmetric saddle steady states. The heteroclinic curve Het_2 starts at the pitchfork curve PF_2, the curve in which the non-symmetric saddle steady states associated with the heteroclinic connection are born; again see Fig. 8.4. We were unable to ascertain why the curve ended at the top end at $(\kappa\tau, I) \approx (2.833, 0.0702)$. A possible explanation may be an interaction with a curve of bifurcations of periodic orbits. However, at present it is not possible to continue bifurcations of periodic orbits in DDEs, therefore, we leave this as an open question. What is clear is that the heteroclinic curves Het_1 and Het_2 cannot cross, as they involve the same branch of the one-dimensional unstable manifold of the non-symmetric saddle steady states. A word of warning is in order: DDE-BIFTOOL continues the boundary value problem beyond the end point of Het_2. However, the above argument and analysis of the data shows that the boundary value does no longer correspond to a heteroclinic connection of the PCF laser.

Figure 8.7 shows orbits along the heteroclinic curve Het_2. The heteroclinic orbit shown in Fig. 8.7 (a) is very close to the pitchfork curve PF_2; note that the non-symmetric steady states, which have just been created, are very close together; see Fig. 8.7 (a3). As one moves along Het_2, the orbits oscillate more as they spiral into the end steady state [Fig. 8.7 (b)]. Finally, near the end of the curve Het_2, the damped oscillations become more irregular with the size of the orbit only increasing slightly in (E,N)-space [Fig. 8.7 (c) and (d)]. One sees the emergence of an extra 'arm' of the orbit

in Fig. 8.7 (d3). This may be an indication of a bifurcating periodic orbit responsible for the destruction of the curve Het_2. We note that, unlike in the case of the curve Het_1, there is no interaction of the curve Het_2 with the trivial saddle steady state. As is seen in Fig. 8.4, the curve Het_2 crosses the curve *ns* at the point B_2, another codimension-two Belyakov point. Below the Belyakov point B_2 the heteroclinic orbits along the curve Het_2 have a negative saddle quantity corresponding to a bifurcating attracting periodic orbit, above B_2 the saddle quantity is positive corresponding to an infinite number of bifurcating saddle periodic orbits.

8.4 Bifurcations of periodic orbits

In this section we make a first attempt at providing a dynamically consistent two-parameter scenario, including bifurcations of periodic orbits, of the locking range of the PCF laser. As has been mentioned, one cannot yet continue bifurcations of periodic orbits in systems of DDEs in two parameters. However, we performed a number of one-parameter studies, detected bifurcations by studying the Floquet multipliers, and plotted the results in $(\kappa\tau, I)$-space.

Figure 8.8 shows coloured points indicating bifurcations of periodic orbits. For different values of I a one-parameter continuation of a periodic orbit was performed. By studying the Floquet multipliers of the system the following bifurcations were detected: saddle-node bifurcations of limit cycles *SL* (yellow points) when a real Floquet multiplier passes through the unit circle at $+1$, period-doubling bifurcations *PD* (green points) when a real Floquet multiplier passes through the unit circle at -1, symmetry-breaking (or restoring) bifurcations *SB* (purple points) when a real Floquet multiplier passes through the unit circle at $+1$, and torus (or Neimark-Sacker) bifurcations *T* (black points) when a complex pair of Floquet multipliers pass through the unit circle. Figure 8.8 (a) shows bifurcations of the periodic orbit originating from the Hopf curve H_1, while Fig. 8.8 (b) shows bifurcations of the periodic orbit originating from the Hopf curve H_2.

Below the double-Hopf point *DH*, Fig. 8.8 (a) clearly identifies that a saddle-node bifurcation of limit cycles *SL* runs close to the curve of subcritical Hopf bifurcations H_1. The stable periodic orbit emerging from the curve *SL* is destabilised at the curve of period-doubling bifurcations *PD* (the first in a route to chaos); see Fig. 7.1 and Figs. 8.2 (b) and (c). The ensuing unstable periodic orbit is destroyed in a symmetry-restoring bifurcation at the curve *SB*. Above the double-Hopf point *DH* the bifurcation

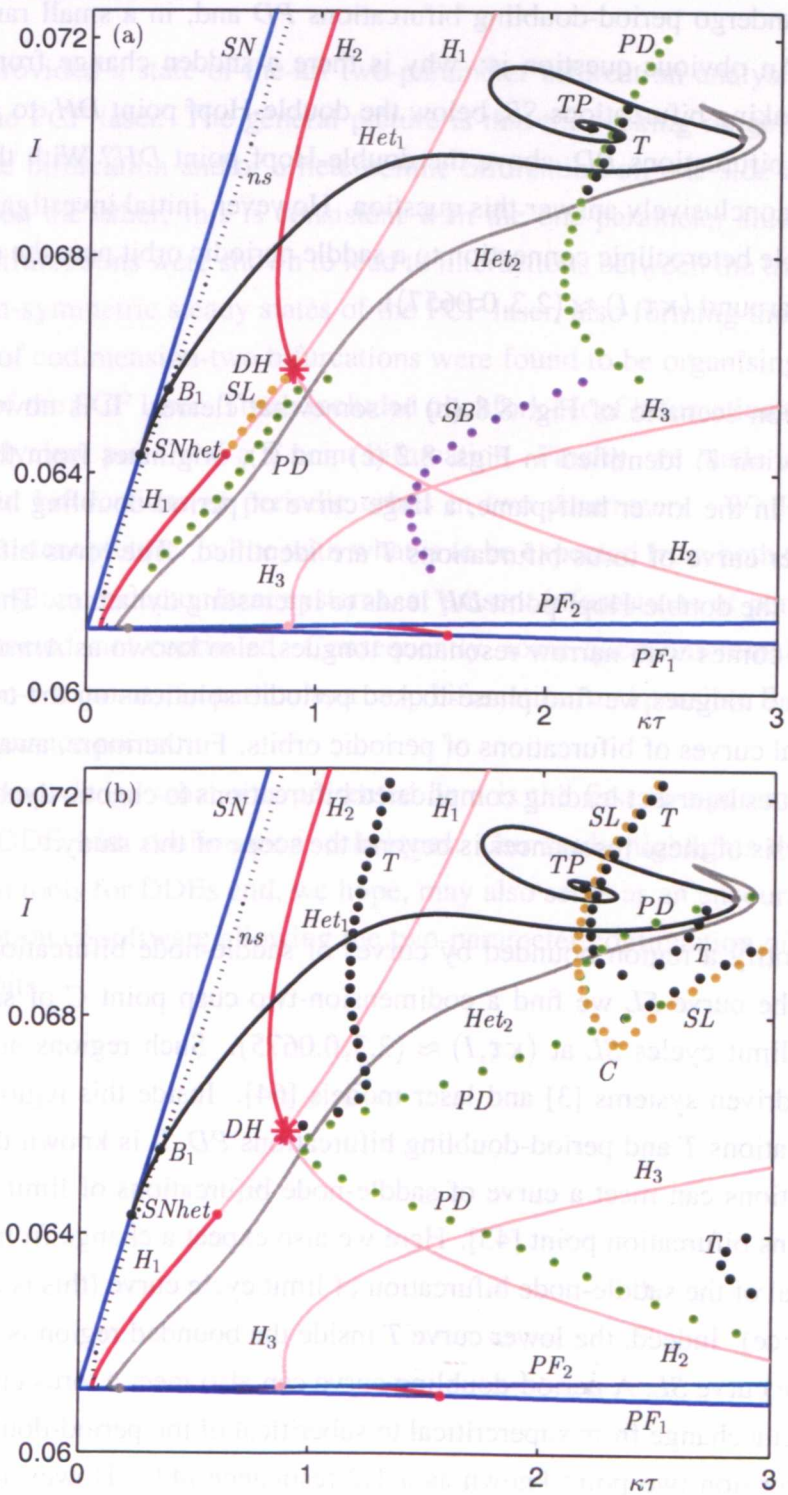

Figure 8.8: Bifurcation diagrams in $(\kappa\tau, I)$-space; panel (a) shows bifurcations of periodic orbits originating from the Hopf curve H_1, and panel (a) shows bifurcations of periodic orbits originating from the Hopf curve H_2.

scenario is very different. The saddle periodic orbits originating from the Hopf curve H_1 are seen to undergo period-doubling bifurcations *PD* and, in a small range, torus bifurcations *T*. An obvious question is: why is there a sudden change from a curve of symmetry-breaking bifurcations *SB*, below the double-Hopf point *DH*, to a curve of period-doubling bifurcations *PD*, above the double-Hopf point *DH*? With the present tools we cannot conclusively answer this question. However, initial investigations have revealed a possible heteroclinic connection to a saddle periodic orbit near the end points of these curves (around $(\kappa\tau, I) \approx (2.3, 0.0657)$).

The bifurcation scenario of Fig. 8.8 (b) is somewhat clearer. It is now clear that the torus bifurcation *T*, identified in Figs. 8.2 (e) and (f), originates from the double-Hopf point *DH*. In the lower half-plane, a large curve of period-doubling bifurcations *PD* and a smaller curve of torus bifurcations *T* are identified. The torus bifurcation *T* originating from the double-Hopf point *DH* leads to interesting dynamics. Theory states that the curve *T* comes with narrow resonance tongues, also known as *Arnold tongues* [43]. Inside these tongues we find phase-locked periodic solutions on the torus which lead to additional curves of bifurcations of periodic orbits. Furthermore, away from the curve *T* the tongues intersect leading complicated bifurcations to chaotic dynamics [43]. A detailed analysis of these resonances is beyond the scope of this study.

We also identify a region bounded by curves of saddle-node bifurcations of limit cycles *SL*. On the curve *SL* we find a codimension-two cusp point *C* of saddle-node bifurcations of limit cycles *SL* at $(\kappa\tau, I) \approx (2.3, 0.0675)$. Such regions are common in periodically driven systems [3] and laser models [64]. Inside this region we identify torus bifurcations *T* and period-doubling bifurcations *PD*. It is known that a curve of torus bifurcations can meet a curve of saddle-node bifurcations of limit cycles at a Bogdanov-Takens bifurcation point [43]. Here we also expect a change from supercritical to subcritical of the saddle-node bifurcation of limit cycle curve (this is also known as a 1:1 resonance). Indeed, the lower curve *T* inside the bounded region is seen to run very close to the curve *SL*. A period-doubling curve can also meet a torus curve. Again we would expect a change from supercritical to subcritical of the period-doubling bifurcation, a codimension-two point known as a 1:2 resonance [43]. However, at present we cannot accurately identify such points and leave a detailed study of bifurcations of periodic orbits as an open problem, to be addressed when a continuation of bifurcations of periodic orbits becomes available.

8.5 Conclusions

We have provided a state-of-the-art two-parameter bifurcation analysis of the locking range of the PCF laser. The general picture is that the locking range is bounded by a saddle-node bifurcation and/or a heteroclinic bifurcation on one side and by Hopf bifurcations on the other; this is consistent with the one-parameter study of Chapter 7. Pitchfork bifurcations were shown to lead to interactions between the trivial steady state and the non-symmetric steady states of the PCF laser, also forming the laser threshold. A number of codimension-two bifurcations were found to be organising centres for the dynamics of the PCF laser. These included pitchfork-Hopf bifurcations, a double-Hopf point, a Belyakov point and a T-point bifurcation. Finally, we made a first attempt at mapping out bifurcations of periodic orbits in two parameters. While this led to an overall consistent picture, in line with what is to be expected from both theory and studies of other semiconductor laser systems, at present bifurcations of periodic orbits can only be detected, not continued. Consequently, some questions remain about further codimension-two points, in particular a cusp bifurcation, and possible Bogdanov-Takens and 1:2 resonance points.

To our knowledge what was presented here is the first two-parameter bifurcation study of a DDE with continuation techniques. Our study highlights the usefulness of continuation tools for DDEs and, we hope, may also serve as an encouragement for the implementation of software allowing the two-parameter continuation of bifurcations of periodic orbits.

Chapter 9

Bistability and torus break-up

This chapter is based on the paper [K. Green B. Krauskopf, and K. Engelborghs, "Bistability and torus break-up in a semiconductor laser with phase-conjugate feedback", *Phys. D*, 173:114–129, 2002].

We now apply the new and advanced numerical tools for DDEs (see Section 3.4.2 and Chapter 5) to investigate the PCF laser. We concentrate on a transition involving the break-up of a torus and show in Section 9.3 that a *crisis bifurcation* is responsible for a sudden transition to chaos: a regular small attractor (a hose-like torus) increases dramatically in size and becomes a large chaotic attractor. Our study is made possible by, firstly, the package DDE-BIFTOOL [12, 13, 14], which allows one to perform continuation and bifurcation analysis of DDEs, much like AUTO [8] does for ordinary differential equations (ODEs); see Section 3.4.2. Our second main tool is to compute one-dimensional (1D) unstable manifolds of saddle periodic orbits in systems of DDEs; see Chapter 5. These unstable manifolds are important for understanding the global dynamics of dynamical systems.

The chapter is organised as follows. In Section 9.1 we show bifurcation diagrams obtained by simulation and by continuation to provide an outline of the dynamics involved in a route to chaos in system (4.1). This leads to the discovery of regions of bistability which we detail in Section 9.2. In Section 9.3 we compute unstable manifolds of locked periodic orbits and show that the mechanism behind the transition to chaos is due to the break-up of a torus culminating in a crisis bifurcation. Finally, we draw conclusions in Section 9.4.

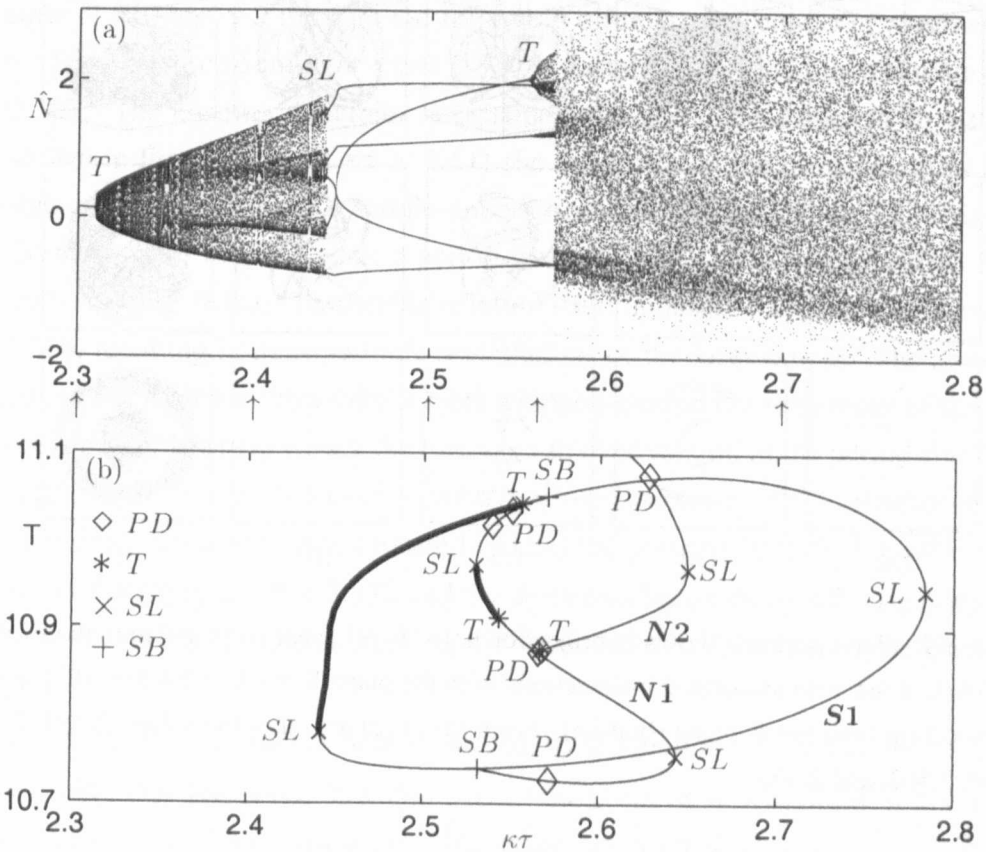

Figure 9.1: Bifurcation diagram obtained by simulation (a), and by continuation with DDE-BIFTOOL (b). The consecutive arrows correspond to the phase portraits shown in Fig. 9.2(a)–(e).

9.1 The bifurcation diagram

As was shown in Fig. 4.2, the general picture of the dynamics of the PCF laser is that, as $\kappa\tau$ is changed, the laser produces stable periodic output interspersed with 'bubbles' of more complicated dynamics, which for the most part are chaotic [23, 35]. We consider in detail a transition to chaos at the beginning of the 'second bubble', in the range of $\kappa\tau \in [2.300, 2.800]$. This transition is outlined in Fig. 9.1, which shows two bifurcation diagrams, one obtained by simulation [Fig. 9.1(a)] and one by continuation [Fig. 9.1(b)].

9.1.1 Simulation

As described in Section 4.1, to obtain Fig. 9.1(a), for each value of $\kappa\tau$ we integrated system (4.1) starting with an initial condition from the attractor for the previous value

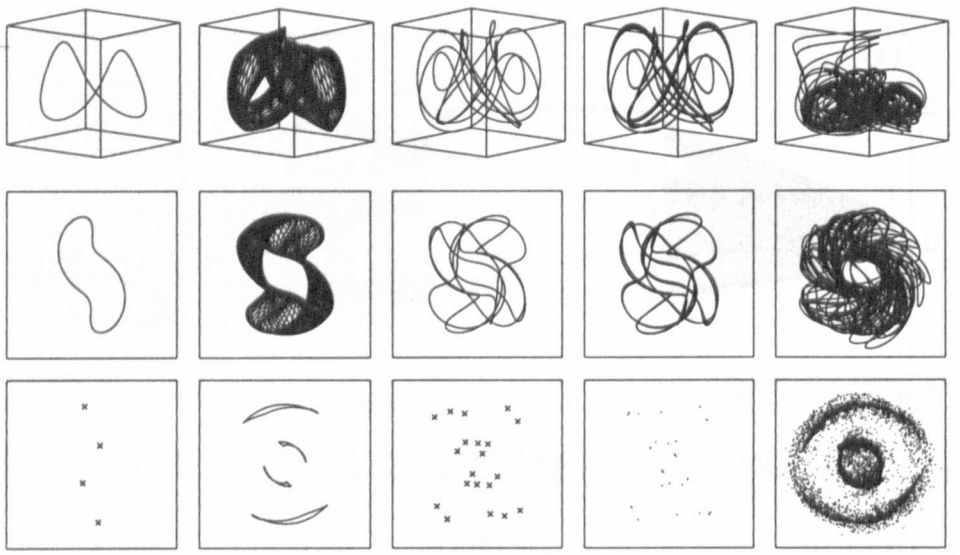

Figure 9.2: Phase portraits shown in projection onto (E,N)-space (top) and onto the E-plane (middle); along with associated intersections with the plane $\Sigma \equiv \{N = 7.620 \times 10^8\}$ shown in projection onto the E-plane (bottom). From (a) to (e) $\kappa\tau$ takes the values 2.300, 2.400, 2.500, 2.562, and 2.700.

of $\kappa\tau$ and let transients die away. Then we plotted the normalised value of the inversion $\hat{N} = (N/N_{sol} - 1) \times 10^3$ whenever the intensity $P(t) = |E(t)|^2$ crossed its average value in the increasing direction. This section was chosen to ensure intersections of the orbit for distinct values of the inversion N [35]. In Fig. 9.1(a), a small number of points correspond to a periodic solution. A large number of points correspond to quasiperiodic or chaotic dynamics.

Figure 9.2 shows the associated representative phase portraits, obtained by simulation, of the dynamics corresponding to Fig. 9.1(a), shown in projection onto (E,N)-space (top) and the E-plane (middle). We also show associated intersections of the orbits with a plane Σ (bottom). Throughout this chapter, we fix the plane

$$\Sigma \equiv \{\,(E,N) \mid N = 7.620 \times 10^8\,\}.$$

The value $N = 7.620 \times 10^8$ was chosen because it is a good approximation to the average value of N for all $\kappa\tau$ in our region of interest, ensuring that all attractors intersect Σ over the entire range of $\kappa\tau$ considered. We remark that the exact choice of Σ is not important, as long as orbits intersect transversally at least locally near the relevant periodic orbits.

Figures 9.1(a) and 9.2 indicate the following bifurcation scenario of symmetric attractors. The periodic solution at $\kappa\tau = 2.300$ is destabilised in a torus bifurcation T at $\kappa\tau \approx 2.307$. The ensuing dynamics is quasiperiodic and takes place on an attracting torus, shown in Fig. 9.2(b). At $\kappa\tau \approx 2.441$ the dynamics on the torus becomes locked to a stable periodic solution in a saddle-node bifurcation of limit cycles *SL*. This stable orbit can be seen in Fig. 9.2(c) as a period-five solution, and it is responsible for the five branches in Fig. 9.1(a). This stable solution itself undergoes a torus bifurcation T at $\kappa\tau \approx 2.556$, resulting in quasiperiodic modulations of the laser output. The associated new torus is essentially a 'hose-like' object wrapped around the remainder of the initial torus; see Fig. 9.2(d) where we see the torus as a thicker version of the period-five locked solution [Fig. 9.2(c)]. It is further confirmed by close inspection of the attractor in Σ that there are indeed invariant circles located around the previously locked solution. This new torus is destroyed at $\kappa\tau \approx 2.570$ and the dynamics becomes chaotic. By comparing simulations for increasing and decreasing $\kappa\tau$, we found that there is no hysteresis in this transition.

A similar route to chaos has been observed, by simulation, in a semiconductor laser with COF [48, 49]. However, no explanation was given as to why there was a sudden transition to a large chaotic attractor. Therefore, an immediate question is: What is the mechanism involved in the sudden transition from the attracting torus to a much larger chaotic attractor? We answer this question in Section 9.3, where we identify this transition to chaos as a crisis bifurcation. This requires the new technique of computing 1D unstable manifolds of system (4.1).

9.1.2 Continuation

Figure 9.1(b) was obtained with DDE-BIFTOOL by starting a continuation from the stable locked periodic solution on the torus. Plotted is the period T, or T/2 for period-doubled solutions, against $\kappa\tau$. We choose to plot T as is often done in continuation studies to ensure a smooth solution branch as $\kappa\tau$ is varied. Attracting solutions are drawn as thick curves, while unstable solutions are thin. By studying the Floquet multipliers of the system we are able to identify the bifurcations involved, namely, saddle-node bifurcations of limit cycles *SL*, period-doubling bifurcations *PD* and torus bifurcations T. Due to the underlying symmetry of system (4.1) we also find symmetry-breaking bifurcations *SB* of a symmetric periodic orbit. Here a real Floquet multiplier passes through the unit circle at $+1$. As opposed to a saddle-node bifurcation of limit cycles, this leads to

the creation of two non-symmetric periodic orbits. Symmetry-breaking bifurcations can be distinguished from saddle-node bifurcations of limit cycles by looking at where they appear on branches. Using the new functionality of DDE-BIFTOOL described in Section 3.4.2, we switched onto and computed the emanating branches of non-symmetric periodic solutions. Figure 9.1(b) shows an oval branch **S1** of symmetric periodic solutions and two branches **N1** and **N2** of non-symmetric periodic solutions. We will refer to **S1** as having a lower and an upper part, bounded by the saddle-node bifurcations of limit cycles *SL* at the maximum and minimum values of $\kappa\tau$.

The main stable solution, indicated by a thick line, lies on the upper part of **S1**. Analysis of the Floquet multipliers shows that this stable solution is born at *SL* at $\kappa\tau \approx 2.441$, marking the onset of locking. It destabilises at $\kappa\tau \approx 2.556$ in the torus bifurcation *T*. This agrees with the simulation in Fig. 9.1(a). The ensuing unstable solution exists until $\kappa\tau \approx 2.784$, where it 'collides' with the lower part of **S1** and both solutions are lost at *SL*. Two additional bifurcations of unstable solutions also exist on **S1**. They are symmetry-breaking bifurcations at the points denoted by *SB*, which are in fact connected by a branch of non-symmetric solutions **N1**.

By continuing the branch **N1** emanating from the point *SB* on the lower part of **S1** at $\kappa\tau \approx 2.532$, we detect a period-doubling bifurcation *PD*. This leads to a period-doubled bifurcating branch **N3** (not shown in Fig. 9.1(b); see Fig. 9.9). We then detect a saddle-node bifurcation of limit cycles *SL*, before a second period-doubling bifurcation *PD* leading to the branch **N2**. At $\kappa\tau \approx 2.543$ a torus bifurcation *T* leads to a stable solution on branch **N1**, indicated by the thick curve. This stable solution is destabilised at a saddle-node bifurcation of limit cycles *SL* at $\kappa\tau \approx 2.530$. The unstable branch then passes two period-doubling bifurcations *PD*. These are in fact connected via a branch of period-doubled unstable solutions (not shown). Finally, symmetry is restored in the symmetry-breaking bifurcation *SB* on the upper part of **S1**.

Continuing the period-doubled branch **N2**, we follow an unstable solution and rapidly detect a torus bifurcation *T* at $\kappa\tau \approx 2.5661$, this leads to another stable solution. This stable solution is almost immediately destabilised in a period-doubling bifurcation *PD* at $\kappa\tau \approx 2.5675$. This small region of stability is invisible on the scale of Fig. 9.1(b), but it is enlarged in Section 9.2 below. Through further continuation of branch **N2**, we detected a saddle-node bifurcation and a period-doubling bifurcation before the branch leaves the window of Fig. 9.1(b).

By following bifurcating branches of unstable solutions, we have found values of $\kappa\tau$ for which there exist regions of bistability and multiple unstable solutions. Figure 9.3

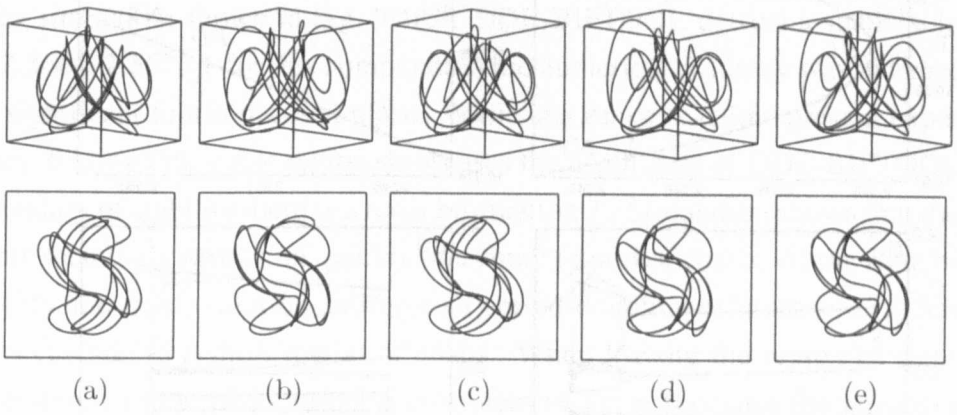

Figure 9.3: Periodic orbits shown in projection onto (E,N)-space (top) and onto the E-plane (bottom) for $\kappa\tau = 2.542$. Showing, the symmetric unstable orbit on the lower part of **S**1 (a), the symmetric stable orbit on the upper part of **S**1 (b), the non-symmetric unstable orbit on the lower part of **N**1 (c), the non-symmetric stable orbit on the middle part of **N**1 (d), and the non-symmetric unstable orbit on the upper part of **N**1 (e).

shows an example of such solutions obtained by taking a vertical slice of Fig. 9.1(b), through the central non-symmetric branch **N**1, where we observe different stable and unstable solutions for $\kappa\tau = 2.542$; see also Fig. 9.4(a) below. Plotted are two symmetric orbits on branch **S**1, one stable and one unstable, as well as three non-symmetric orbits on branch **N**1, one stable and two unstable. If symmetric counterparts of the non-symmetric orbits are included, there are eight coexisting periodic solutions, three of which are attractors and five of which are of saddle-type.

9.2 Windows of bistability

We now investigate in detail the two regions of bistability that we identified in Fig. 9.1(b). This bistability is between a symmetric pair of periodic solutions on **N**1 and the main periodic solution on **S**1, and between a symmetric pair of periodic solutions on **N**2 and the 'hose-like' torus shown in Fig. 9.2(d). Both of the symmetric pairs of periodic solutions have small basins of attraction and, therefore, would be extremely difficult to observe in simulations without using initial conditions obtained by continuation. We remark that there is no hysteresis associated with these stable solutions when one follows the main attractor as in Fig. 9.1(a). This is because the windows of stability are connected to **S**1 via unstable branches, so that, scanning back and forth, in the bifurcation diagram,

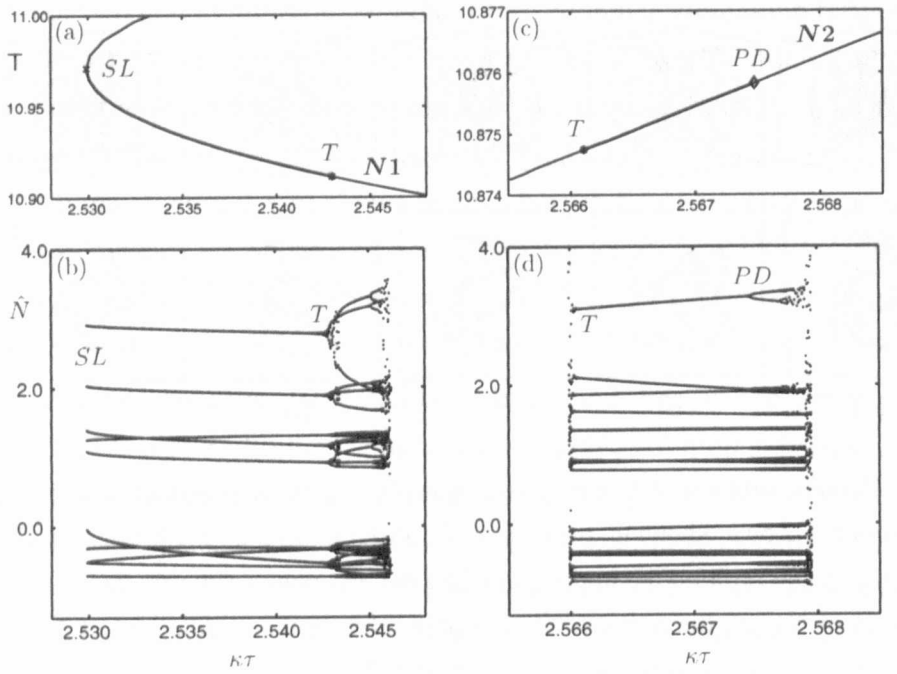

Figure 9.4: Bifurcation diagrams near the stable region of branch **N**1, obtained by continuation (a) and by simulation (b), and near the stable region of branch **N**2, again obtained by continuation (c) and by simulation (d).

the dynamics is always attracted to the main attractor.

The first region of stability on **N**1 is illustrated in Figs. 9.4(a) and (b). Continuation shows that a stable periodic orbit is born at $\kappa\tau \approx 2.530$ in a saddle-node bifurcation of limit cycles *SL*. It exists for $\kappa\tau \in [2.530, 2.543]$. By starting from the attracting periodic solution found with DDE-BIFTOOL [Fig. 9.4(a)], we can compute a bifurcation diagram by simulation to see what happens to this solution as we increase and decrease $\kappa\tau$ in small steps. This results in the bifurcation diagram of Fig. 9.4(b). As found by continuation, at $\kappa\tau \approx 2.543$, the periodic orbit undergoes a torus bifurcation *T*. The dynamics then locks to a periodic solution. This locked solution seemingly undergoes a period-doubling cascade to a small region of chaos. After this, the solution jumps to the main attractor of system (4.1), in this case the stable periodic solution on **S**1. Notice that Fig. 9.4(a) contains ten branches due to the non-symmetric nature of the solution, the periodic orbit is still of period five.

The region of stability on **N**2 is illustrated in Figs. 9.4(c) and (d). Again, by starting from the attracting periodic solution found with continuation [Fig. 9.4(c)] and integrating as we increase and decrease $\kappa\tau$ in small steps, we obtain the bifurcation dia-

gram by simulation shown in Fig. 9.4(d). DDE-BIFTOOL detects a stable solution for $\kappa\tau \in [2.5661, 2.5675]$; for this computation the numerical accuracy was increased to ensure a significant fourth decimal place. While this range is below present experimental accuracy, finding this stable region showcases the usefulness of DDE-BIFTOOL. At the left boundary of stability there is a torus bifurcation T. Simulation shows that the emerging torus seemingly breaks up quickly to a small region of chaos. At the right boundary of stability, the stable solution undergoes a period-doubling bifurcation *PD*. Simulation shows a cascade to a short region of chaos. When leaving the region of stability, the solution jumps to the main attractor of system (4.1), in this case the attracting 'hose-like' torus. Notice that Fig. 9.4(c) contains twenty branches due to the period-doubled non-symmetric nature of the solution, the periodic orbit is of period ten.

The new attracting periodic solutions, that were found in these simulations, could be continued with DDE-BIFTOOL, but due to the small parameter ranges in which these solutions exist, we stop here. However, the overall picture is again that of the break-up of a torus but on a smaller scale.

9.3 Break-up of a torus

The bifurcation diagrams of Fig. 9.1, along with the phase portraits in Fig. 9.2, present a good picture of the main attractors involved in the break-up of a torus in a semiconductor laser with PCF. However, in order to understand this transition fully, in particular, to understand why we have a sudden change from an attracting torus to a much larger chaotic attractor, we need to investigate what happens to the underlying torus after locking. For this it is not sufficient to use mere simulation, because for $2.440 < \kappa\tau < 2.555$ one will only get an image of the stable periodic orbit [Fig. 9.2(c)], and not of the torus (or its remainder) on which it lies. This is where our method for the computation of the 1D unstable manifolds of the saddle periodic orbits is crucial.

The saddle periodic orbits we used are along the lower part of **S1** and are shown in the bottom row of Fig. 9.5. The top row shows the corresponding stable orbits. Both are shown in projection onto the E-plane and the values of parameters are $\kappa\tau = 2.445$, $\kappa\tau = 2.450$, $\kappa\tau = 2.480$, $\kappa\tau = 2.500$ and $\kappa\tau = 2.531$. At these values of $\kappa\tau$, between *SL* and *SB* on the lower part of **S1** [Fig.9.1(b)], the saddle periodic orbits have exactly one unstable Floquet multiplier and therefore, their unstable manifolds are one dimensional. This allows us to compute them with the methods outlined in Chapter 5.

In Fig. 9.6 we show the trace of these unstable manifolds in the plane Σ. The crosses

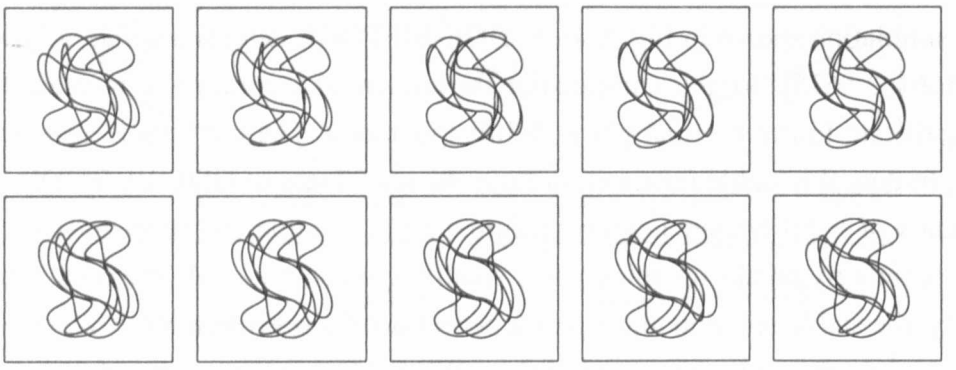

Figure 9.5: Symmetric stable orbits (top) and corresponding symmetric unstable orbits (bottom) shown in projection onto the E-plane. From (a) to (e) $\kappa\tau$ takes the values 2.445, 2.450, 2.480, 2.500 and 2.531; the square is $E \in [-400, 400] \times [-400, 400]$.

(+) mark the five intersection points with Σ of the saddle periodic orbit in Fig. 9.5. From each saddle point there emanate two branches of the unstable manifold, which converge to neighbouring attracting points ($\times$) corresponding to the stable periodic orbit in Fig. 9.5. In this way and much like for ODEs, the torus, or what remains of it is the closure of these branches of the 1D unstable manifold, and it shows up as a closed curve. Note that there are twenty intersections associated with locking on the full torus [Fig. 9.2(c)]. They correspond to the torus intersecting four times resulting in four groups of five intersections. We show only the top five intersections. Recall that the different branches of the unstable manifold are allowed to intersect each other because we are looking at a two-dimensional projection of an infinite-dimensional system.

Our computations reveal the following bifurcation scenario as $\kappa\tau$ is increased through the locking region. The locking of the quasiperiodic solution [Fig. 9.6(a)] produces a stable periodic solution that exists on a smooth torus [Fig. 9.6(b)], as one expects immediately after locking. However, smoothness is lost as the manifold starts to 'curl up' along the stable periodic orbit. DDE-BIFTOOL detects this transition at $\kappa\tau \approx 2.4492$, where we found that the two Floquet multipliers close to and inside the unit circle become a complex pair. Figure 9.6(c) shows the manifold just after this transition at $\kappa\tau = 2.450$. Notice that the branches of the manifold are no longer smoothly connected at the attractors ($\times$) but now spiral into them. Physically, this corresponds to damped oscillations of the laser output as it settles down to its periodic solution. The unstable manifold becomes increasingly folded and stretched as $\kappa\tau$ is increased and the

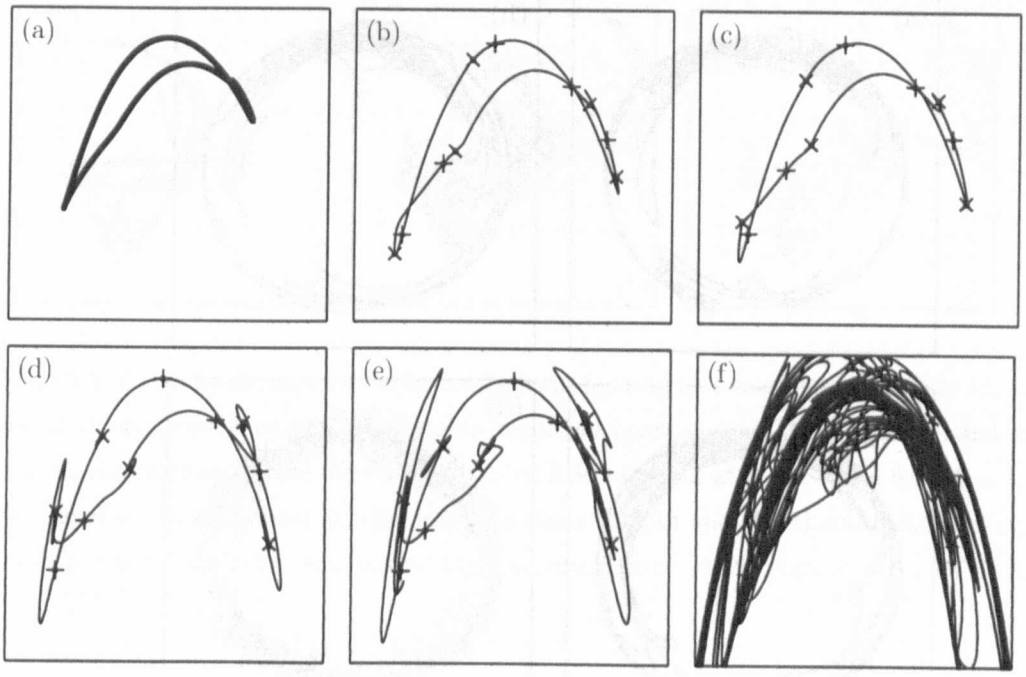

Figure 9.6: Break-up of the torus in the plane $\Sigma \equiv \{N = 7.620 \times 10^8\}$. Except for (a), which was obtained by simulation, plotted are all branches of the 1D unstable manifolds of the saddle points (+), which converge to the attractors (×). From (a) to (f) $\kappa\tau$ takes the values 2.400, 2.445, 2.450, 2.480, 2.500 and 2.531; the square is $E \in [-300, 300] \times [140, 300]$.

chaotic region is approached. Nevertheless, the torus is still a continuous (but not a smooth) object [Figs. 9.6(d) and (e)]. The transients are becoming increasingly complicated as $\kappa\tau$ is increased. At $\kappa\tau = 2.531$ we see the unstable manifold covering a large part of the upper part of the E-plane [Fig. 9.6(f)] and also making excursions into the lower part; see already Fig. 9.7(a) which shows the 1D unstable manifold of Fig. 9.6(f) over a larger area of the E-plane. Note that Fig. 9.7 still shows the 1D unstable manifold associated with only the top group of five of the twenty intersections of the saddle periodic orbit with Σ.

At $\kappa\tau \approx 2.5348$ the saddle periodic orbit undergoes a symmetry-breaking bifurcation *SB*, resulting in an additional unstable direction of the unstable manifold. However, it is still possible to compute the *strong unstable manifold*, corresponding to the largest, real Floquet multiplier of the associated periodic; see also Fig. 5.6. This strong unstable manifold is shown in Fig. 9.7 inside the chaotic region for the saddle periodic orbit on the lower part of **S**1 at $\kappa\tau = 2.700$ [Fig. 9.7(b)]. It is indeed a continuation of the unstable manifold for $\kappa\tau = 2.531$ [Fig. 9.7(a)].

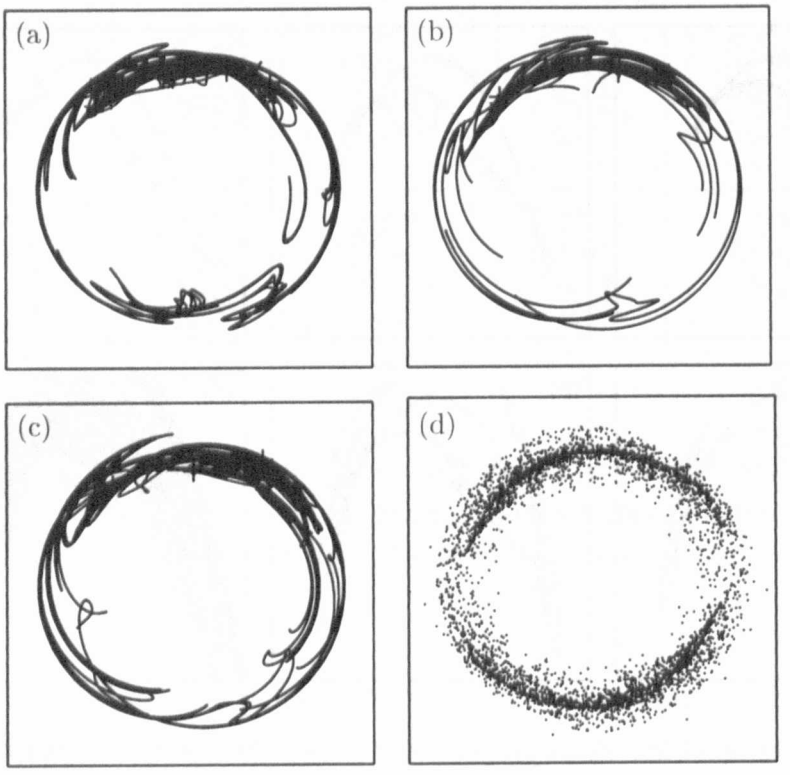

Figure 9.7: Break-up of the torus in the plane $\Sigma \equiv \{N = 7.620 \times 10^8\}$. Plotted are all branches of the 1D unstable manifolds for $\kappa\tau = 2.531$ (a) and $\kappa\tau = 2.700$ (b) on the lower part of **S**1, for $\kappa\tau = 2.700$ on the upper part of **S**1 (c) and the associated intersection of the main attractor for $\kappa\tau = 2.700$ (d); the square is $E \in [-400, 400] \times [-400, 400]$.

We also computed 1D unstable manifolds for the saddle periodic orbits along the upper part of **S**1 between *SB* and *SL*. Here the saddle orbits have exactly one unstable Floquet multiplier and, therefore, also have one unstable direction. An associated unstable manifold, for $\kappa\tau = 2.700$, is shown in Fig. 9.7(c). We observe that it is very similar to the unstable manifold in Fig. 9.7(b). As is generally the case, the unstable manifold accumulates on the chaotic attractor. To illustrate this, the associated intersection with Σ of the upper and lower parts of the main chaotic attractor for $\kappa\tau = 2.700$ is shown in Fig. 9.7(d).

The sudden transition to chaos at $\kappa\tau \approx 2.570$ is indicative of a crisis bifurcation, in which we see a discontinuous change in the size or shape of an attractor [24, 25, 54]. In our case this attractor is the hose-like torus. At the crisis bifurcation there is a rearrangement of stable and unstable manifolds of suitable saddle points. It is not possible to compute the infinite-dimensional stable manifold of a saddle point in a DDE. However,

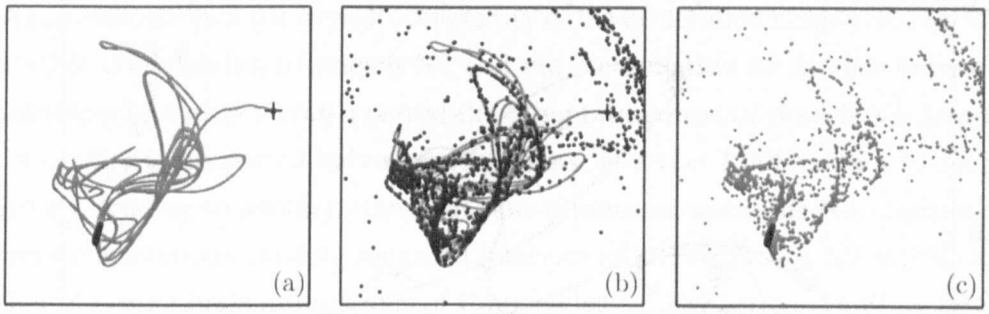

Figure 9.8: Crisis bifurcation of the hose-like torus leading to a much larger chaotic attractor. Plotted is one branch of the 1D unstable manifold (grey curve) and the associated main attractor (black dots) before the crisis for $\kappa\tau = 2.569$ (a) and after the crisis for $\kappa\tau = 2.571$ (b). Panel (c) is an overlay of the hose-like torus (black) and the chaotic attractor (grey) that exist before and after the crisis bifurcation, respectively; the square is $E \in [-95, 105] \times [235, 275]$.

we can cast more light on this bifurcation by computing the branch of the 1D unstable manifold that ends up at the attractor. This is shown in Fig. 9.8 (a) and (b) for one (of the five) saddle points corresponding to the saddle periodic orbit; compare Fig. 9.1 (b). Just before the crisis bifurcation at $\kappa\tau = 2.569$ [Fig. 9.8 (a)] the unstable manifold is contained in the basin of attraction of the hose-like torus and, hence, eventually ends up at the corresponding attracting invariant circle. Notice however, that this branch makes large excursions before settling down. After the crisis bifurcation at $\kappa\tau = 2.571$ [Fig. 9.8 (b)] the hose-like torus has seemingly been replaced by a much larger chaotic attractor. The unstable manifold accumulates on this new attractor, which has a shape resembling the manifold just prior to the bifurcation. However, the chaotic attractor is no longer confined by the stable manifold of the saddle. Overlaying the attractor before and after the crisis bifurcation [Fig. 9.8 (c)] shows that the hose-like torus is 'part of' the large chaotic attractor. In other words, in the crisis bifurcation a small 'regular' attractor (an invariant torus) suddenly and discontinuously changes in size to become a chaotic attractor.

The crisis bifurcation we found in the PCF laser is much like an interior crisis in that there is a sudden growth in the size of the attractor. However, the smaller attractor is not chaotic itself (as is generally assumed in the definition of an interior crisis [24, 25, 54]). We remark that the sudden appearance of the much larger chaotic attractor is preceded by more and more complex transients due to the increasingly complicated geometry of

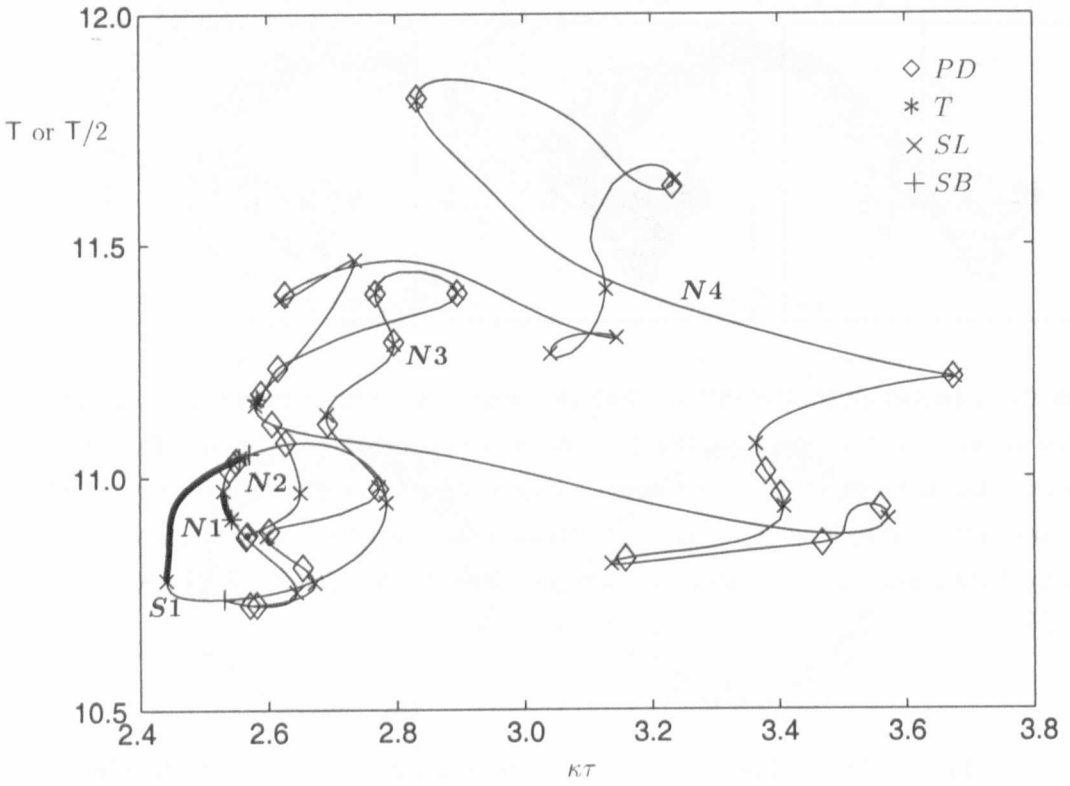

Figure 9.9: Bifurcation diagram obtained by continuation showing the branches **N**2 and **N**3, which are connected to a further bifurcating branch **N**4.

unstable manifolds; see Figs. 9.6–9.8.

9.4 Conclusions

In summary, we have presented a detailed numerical investigation of a route to chaos via the break-up of a torus in a PCF laser. A similar transition has also been observed in a COF laser [49] but the actual sudden transition to the chaotic attractor has not been explained. Our results clearly indicate that the chaotic attractor associated with this transition was created at a crisis bifurcation. We believe this to be the first time that a sudden transition to chaos has been studied in detail in a system of DDEs. This was only made possible by advanced numerical tools for DDEs, namely the package DDE-BIFTOOL to compute saddle periodic orbits, combined with our new technique for computing unstable manifolds of saddle periodic orbits. This highlights the use of these techniques for DDEs in general.

As an indication of the overall complexity of the bifurcation diagrams, Fig. 9.9 shows the further continuation of branch N2 and the continuation of another branch of non-symmetric solutions N3 from a period-doubling bifurcation of branch N1. Branches N2 and N3 both end in period-halving bifurcations, at $\kappa\tau \approx 2.6063$ and $\kappa\tau \approx 2.5893$ respectively, leading to another branch of non-symmetric solutions N4. Here we clearly see multiple solutions existing for small intervals of $\kappa\tau$. Branches N2 and N3 contain a number of saddle-node bifurcations of limit cycles *SL* and period-doubling bifurcations *PD*, the latter lead to other branches which could be continued. Moreover, at the end of branch N3 we find a small region of stability which undergoes a period-halving bifurcation leading to a small region of stability on branch N4 for $\kappa\tau \in [2.5832, 2.5893]$. We found that these stable solutions have such small basins of attraction that it is numerically very difficult to find the stable solution even when starting from the numerical approximation provided by DDE-BIFTOOL. We believe that the period-doubling of this stable solution on branch N4 is the start of a period-doubling cascade to chaos. If this is the case, it implies the coexistence of two chaotic attractors.

We note here that the symmetry-breaking bifurcation *SB* on the upper part of S1 [Fig. 9.1(b)] appears to coincide with the value of $\kappa\tau$ at which we identified the crisis bifurcation. A possible explanation connecting these two events is as follows. As *SB* is approached along branch N1, the non-symmetric orbit tends to the symmetric orbit of branch S1. The fact that these two periodic orbits come together implies that a much larger phase space can be visited by the unstable manifold. Eventually at *SB* the periodic orbits coincide and we see the sudden emergence of the chaotic attractor.

Chapter 10

Discussion

Using continuation techniques and manifold computations we presented a detailed dynamical picture of the single-mode PCF laser, as described by system (4.1). We hope this knowledge will lead to experiments using phase-conjugate feedback and that our bifurcation analysis will allow experimentalists to manipulate the PCF laser output to their requirements.

There is a lot of current interest in the dimensionality of attractors in lasers with delay, particularly for use in communication schemes [63]. We remark that the transition outlined in Chapter 9, up to and including the chaotic region, can occur in a phase-space of minimal dimension three. This leads to the open question: What are the mechanisms involved in the routes to chaos for higher values of $\kappa\tau$? In particular, what happens during the transition from the third bubble of chaos to the fourth ECM [see Fig. 4.2]? Are these transitions to 'high-dimensional chaos'?

Using chaotic signals for communication close to a sudden chaotic transition may, in the presence of noise, result in loss of the chaotic attractor to a periodic solution. This would be vastly undesirable, especially in encryption schemes. Therefore, other sudden transitions to chaos should be investigated. A principal tool in these investigations would be computing unstable manifolds of saddle periodic orbits, as was detailed in Chapter 5. One such sudden transition is the saddle-node bifurcation of limit cycles between ECM2 and the second bubble of chaos. It appears to involve chaotic transients, and our aim for the future is to find the chaotic saddle associated with this transition by computing the one-dimensional unstable manifold of the bifurcating saddle periodic orbit.

The effect on the dynamics of varying other parameters within the PCF laser system should also be looked at. In this thesis, we predominantly investigated the effect variations in the feedback strength had on the dynamics because this parameter is easiest to

vary experimentally. One may also look at other parameters, for example, the parameter α. Although α may not be changed during an experiment (it is a material property of the laser), different lasers have different α values and, therefore, an investigation of how a variation in α affects the dynamics of the laser would be a worthwhile study.

In Chapter 8, we took first steps in investigating what variations in the value of the pump current (an experimentally accessible parameter) has on the dynamics of the PCF laser. Our study was restricted to two-parameter continuation of steady states and connecting orbits. The development of routines allowing two-parameter continuation of bifurcations of periodic orbits would be the next logical step in furthering this work and to the study of DDEs in general.

Any method for growing unstable manifolds in ODEs or maps may be generalised in the same way to DDEs (or their Poincaré maps). We have taken here the first step by computing 1D unstable manifolds of saddle points. It is an interesting challenge for future work to compute 2D unstable manifolds of equilibria by generalising the method in [40], and 2D unstable manifolds of saddle fixed points (corresponding to periodic orbits of the DDE) by generalising that in [38].

We further plan to integrate our method for computing unstable manifolds of saddle-periodic orbits in DDEs with DDE-BIFTOOL. Our method requires as starting data a saddle periodic orbit and an associated linear eigenfunction, specifying the direction of the local unstable manifold, of the saddle periodic orbit. The saddle periodic orbit is presently found with DDE-BIFTOOL, but the eigenfunction is computed with an iterative approach. Just as with steady state solutions, DDE-BIFTOOL will be extended to also compute the eigenfunction and, therefore, automatically provide all necessary starting data needed for a manifold computation. This is not only more accurate, but also allows for a direct integration of both methods in a single environment, for example, in a Matlab interface of DDE-BIFTOOL.

In conclusion, we believe that the results presented in this thesis showcase the usefulness of continuation and manifold computations for the study of DDEs and that the techniques described here will contribute to the development of the theory of global bifurcations in DDEs.

Bibliography

[1] G. P. Agrawal and G. R. Gray. Effect of phase-conjugate feedback on the noise characteristics of semiconductor lasers. *Phys. Rev. A*, 46:5890, 1992.

[2] A. Back, J. Guckenheimer, M. Myers, F. Wicklin, and P. Worfolk. Dstool: Computer assisted exploration of dynamical systems. *Notices AMS*, 39(4):303, 1992.

[3] H. W. Broer and B. Krauskopf. Chaos in periodically driven systems. In Krauskopf and Lenstra [37], pages 31–53.

[4] T. W. Carr, D. Pieroux, and P. Mandel. Theory of a multimode semiconductor laser with optical feedback. *Phys. Rev. A*, 63(033817), 2001.

[5] N. Cyr, C. N. Breton, M. Tetu, and S. Theriault. Laser-diode frequency control by resonant phase-conjugate reflection from an atomic vapor. *Opt. Lett.*, 16:1298, 1991.

[6] D. H. DeTienne, G. R. Gray, G. P. Agrawal, and D. Lenstra. Semiconductor laser dynamics for feedback from a finite-penetration-depth phase-conjugate mirror. *IEEE J. Quantum Electron.*, 33:838, 1997.

[7] O. Diekmann, S. A. Van Gils, S. M. Verduyn Lunel, and H. O. Walther. *Delay Equations: Functional-, Complex-, and Nonlinear Analysis*, volume 110. Springer-Verlag, 1995.

[8] E. Doedel, T. Fairgrieve, B. Sandstede, A. Champneys, Yu. Kuznetsov, and X. Wang. AUTO 97: Continuation and bifurcation software for ordinary differential equations, 1997. `http://indy.cs.concordia.ca/auto/main.html`.

[9] R. D. Driver. *Ordinary and Delay Differential Equations*. Springer-Verlag, Berlin, 1977.

[10] J. L. A. Dubbeldam, B. Krauskopf, and D. Lenstra. Excitability and coherence resonance in lasers with saturable absorber. *Phys. Rev. E*, 60:6580, 1999.

[11] K. J. Engel and R. Nagel. *One-parameter semigroups for linear evolution equations*, volume 194 of *Graduate texts in mathematics*. Springer-Verlag, New York, 2000.

[12] K. Engelborghs, T. Luzyanina, K. in't Hout, and D. Roose. Collocation methods for the computation of periodic solutions of delay differential equations. *SIAM J. Sci. Comput.*, 22:1593, 2000.

[13] K. Engelborghs, T. Luzyanina, and D. Roose. Numerical bifurcation analysis of delay differential equations. *J. Comput. Appl. Math.*, 125:265, 2000.

[14] K. Engelborghs, T. Luzyanina, and G. Samaey. DDE-BIFTOOL v2.00: a Matlab package for bifurcation analysis of delay differential equations. Technical Report TW-330, Department of Computer Science, K. U. Leuven, Belgium, 2000. `http://www.cs.kuleuven.ac.be/~koen/delay/ddebiftool.shtml`.

[15] I. R. Epstein and J. A. Pojman. *An Introduction to Non-linear Chemical Oscillations*. Oxford University Press, New York, 1998.

[16] I. Fischer, Y. Liu, and P. Davis. Synchronization of chaotic semiconductor laser dynamics on subnanosecond time scales and its potential for chaos communication. *Phys. Rev. A*, 62(011801), 2000.

[17] A. Gavrielides. Nonlinear dynamics of semiconductor lasers: Theory and experiments. In Krauskopf and Lenstra [37], pages 191–217.

[18] D. Gay and N. McCarthy. Effects of phase-conjugate feedback on the modal content and noise characteristics of a cw argon ion laser: experimental results. *Opt. Commun.*, 193:197–205, 2001.

[19] C. R. Giuliano. Applications of optical phase conjugation. *Physics Today*, 34(4):27–35, April 1981.

[20] P. Glendinning and C. Sparrow. T-points: A codimension two heteroclinic bifurcation. *Journal of Statist. Phys.*, 43:479, 1986.

[21] H. Glüsing-Lüerssen. A behavioural approach to delay-differential systems. *SIAM J. Control Optim.*, 35:480, 1997.

[22] G. R. Gray, D. H. DeTienne, and G. P. Agrawal. Mode locking in semiconductor lasers by phase-conjugate optical feedback. *Opt. Lett.*, 20:1295, 1995.

[23] G. R. Gray, D. Huang, and G. P. Agrawal. Chaotic dynamics of semiconductor lasers with phase-conjugate feedback. *Phys. Rev. A*, 49:2096, 1994.

[24] C. Grebogi, E. Ott, F. Romeiras, and J. A. Yorke. Critical exponents for crisis-induced intermittency. *Phys. Rev. A*, 36:11, 1987.

[25] C. Grebogi, E. Ott, and J. A. Yorke. Critical exponent of chaotic transients in nonlinear dynamical systems. *Phys. Rev. Lett.*, 57:11, 1986.

[26] K. Green and B. Krauskopf. Bifurcation analysis of frequency locking in a semiconductor laser with phase-conjugate feedback. *Int. J. Bif. Chaos, to appear.*

[27] K. Green and B. Krauskopf. Global bifurcations and bistability at the locking boundaries of a semiconductor laser with phase-conjugate feedback. *Phys. Rev. E*, 66(016220), 2002.

[28] K. Green, B. Krauskopf, and K. Engelborghs. Bistability and torus break-up in a semiconductor laser with phase-conjugate feedback. *Phys. D*, 173:114–129, 2002.

[29] J. Guckenheimer and P. Holmes. *Nonlinear Oscillations, Dynamical Systems, and Bifurcations of Vector Fields.* Springer-Verlag, 1993.

[30] B. Haegeman, K. Engelborghs, D. Roose, D. Pieroux, and T. Erneux. Stability and rupture of bifurcation bridges in semiconductor lasers subject to optical feedback. *Phys. Rev. E*, 66(046216), 2002.

[31] J. K. Hale and S. M. Verduyn Lunel. *Introduction to Functional Differential Equations.* Springer-Verlag, 1993.

[32] T. Heil, I. Fischer, W. Elsäßer, and A. Gavrielides. Dynamics of semiconductor lasers subject to delayed optical feedback: The short cavity regime. *Phys. Rev. Lett.*, 87(243901), 2001.

[33] T. Heil, I. Fischer, W. Elsäßer, J.Mulet, and C. R. Mirasso. Chaos synchronization and spontaneous symmetry-breaking in symmetrically delay-coupled semiconductor lasers. *Phys. Rev. Lett.*, 86(5):795–798, 2001.

[34] D. Hobson. An efficient method for computing invariant manifolds of planar maps. *J. Comput. Phys.*, 104:14–22, 1993.

[35] B. Krauskopf, G. R. Gray, and D. Lenstra. Semiconductor laser with phase-conjugate feedback: Dynamics and bifurcations. *Phys. Rev. E*, 58:7190–7196, 1998.

[36] B. Krauskopf and K. Green. Computing unstable manifolds of periodic orbits in delay differential equations. *J. Comput. Phys., to appear.*

[37] B. Krauskopf and D. Lenstra, editors. *Fundamental Issues of Nonlinear Laser Dynamics*, volume 548. AIP Conf. Proc., 2000.

[38] B. Krauskopf and H. M. Osinga. Globalizing two-dimensional unstable manifolds of maps. *Int. J. Bif. Chaos*, 8(3):483–503, 1998.

[39] B. Krauskopf and H. M. Osinga. Growing 1d and quasi-2d unstable manifolds of maps. *J. Comput. Phys.*, 146:404, 1998.

[40] B. Krauskopf and H. M. Osinga. Two-dimensional global manifolds of vector fields. *CHAOS*, 9(3):768–774, 1999.

[41] B. Krauskopf and H. M. Osinga. Investigating torus bifurcations in the forced van der pol oscillator. In E. J. Doedel and L. S. Tuckerman, editors, *Numerical Methods for Bifurcation Problems and Large-Scale Dynamical Systems*, volume 119 of *IMA Vol. Math. Appl.*, pages 199–208. Springer-Verlag, 2000.

[42] B. Krauskopf, G. H. M. Van Tartwijk, and G. R. Gray. Symmetry properties of lasers subject to optical feedback. *Opt. Commun.*, 177:347, 2000.

[43] Y. Kuznetsov. *Elements of Applied Bifurcation Theory*. Springer, Berlin, 1995.

[44] R. Lang and K. Kobayashi. External optical feedback effects on semiconductor injection laser properties. *IEEE J. Quantum Electron.*, 16(3):347, 1980.

[45] D. Lenstra, B. H. Verbeek, and A. J. den Boef. Coherence collapse in single-mode semiconductor lasers due to optical feedback. *IEEE J. Quantum Electron*, 21:674, 1985.

[46] D. Lenstra and M. Yousefi. Theory of delayed optical feedback in lasers. In Krauskopf and Lenstra [37], pages 87–111.

[47] C. M. Marcus and R. M. Westervelt. Stability of analog networks with delay. *Phys. Rev. A*, 39:347, 1989.

[48] J. Mørk, J. Mark, and B. Tromborg. Route to chaos and competition between relaxation oscillations for a semiconductor laser with optical feedback. *Phys. Rev. Lett.*, 65(16):1999–2002, 1990.

[49] J. Mørk, B. Tromborg, and J. Mark. Chaos in semiconductor lasers with optical feedback: Theory and experiment. *IEEE J. Quantum Elec.*, 28:93, 1992.

[50] J. D. Murray. *Mathematical Biology*, volume 19. Springer-Verlag, Berlin, 1980.

[51] T. S. Parker and L. O. Chua. *Practical Numerical Algorithms for Chaotic Systems*. Springer-Verlag, New York/Berlin, 1989.

[52] D. Pieroux, T. Erneux, B. Haegeman, K. Engelborghs, and D. Roose. Bridges of periodic solutions and tori in semiconductor lasers subject to delay. *Phys. Rev. Lett.*, 87(193901), 2001.

[53] D. Pieroux, T. Erneux, T. Luzyanina, and K. Engelborghs. Interacting pairs of periodic solutions lead to tori in lasers subject to delayed feedback. *Phys. Rev. E*, 63(036211), 2001.

[54] C. Robert, K. T. Alligood, E. Ott, and J. A. Yorke. Explosions of chaotic sets. *Phys. D*, 144:44, 2000.

[55] G. Samaey, K. Engelborghs, and D. Roose. Numerical computation of connecting orbits in delay differential equations. Technical Report TW-329, Department of Computer Science, K. U. Leuven, Belgium, 2001.

[56] M. Sciamanna, T. Erneux, F. Rogister, O. Deparis, P. Megret, and M. Blondel. Bifurcation bridges between external-cavity modes lead to polarization self-modulation in vertical-cavity surface-emitting lasers. *Phys. Rev. A*, 65(041801(R)), 2002.

[57] R. Seydel. *Practical Bifurcation and Stability Analysis*. Springer-Verlag, 1994.

[58] T. Shimura, M. Tamura, and K. Kuroda. Injection locking and mode switching of a diode laser with a double phase-conjugate mirror. *Opt. Lett.*, 18:1645, 1993.

[59] G. H. M. Van Tartwijk and G. P. Agrawal. Laser instabilities: a modern perspective. *Prog. Quantum Electron.*, 22:43, 1998.

[60] G. H. M. Van Tartwijk and D. Lenstra. Semiconductor lasers with optical injection and feedback. *Quantum Semiclass. Opt.*, 7:87–143, 1995.

[61] G. H. M. Van Tartwijk, H. J. C. Van der Linden, and D. Lenstra. Theory of a diode laser with phase-conjugate feedback. *Opt. Lett.*, 17:1590, 1995.

[62] S. M. Verduyn Lunel and B. Krauskopf. The mathematics of delay equations with an application to the Lang-Kobayashi equations. In Krauskopf and Lenstra [37], pages 66–86.

[63] J. K. White and J. V. Moloney. Multichannel communication using an infinite dimensional spatiotemporal chaotic signal. *Phys. Rev. A*, 59:2422, 1999.

[64] S. Wieczorek, B. Krauskopf, and D. Lenstra. Unnested islands of period-doubling in an injected semiconductor laser. *Phys. Rev. E*, 84(056204), 2001.

[65] S. Wieczorek, B. Krauskopf, and D. Lenstra. Multipulse excitability in a semiconductor laser with optical injection. *Phys. Rev. Lett.*, 88(6), 2002.

[66] G. D. Van Wiggeren and R. Roy. Communication with chaotic lasers. *Science*, 279:1198, 1998.

[67] X. S. Yao and L. Makeli. Dual microwave and optical oscillator. *Opt. Lett.*, 22:1867, 1997.

[68] Z. You, E. J. Kostelich, and J. A. Yorke. Calculating stable and unstable manifolds. *Int. J. Bif. Chaos*, 1:605, 1991.